ORNL/TM-2021/2207

Mercury Remediation Technology Development

for Lower East Fork Poplar Creek—FY 2021 Update

DOCUMENT AVAILABILITY

Reports produced after January 1, 1996, are generally available free via US Department of Energy (DOE) SciTech Connect.

Website www.osti.gov

Reports produced before January 1, 1996, may be purchased by members of the public from the following source:

National Technical Information Service
5285 Port Royal Road
Springfield, VA 22161
Telephone 703-605-6000 (1-800-553-6847)
TDD 703-487-4639
Fax 703-605-6900
E-mail info@ntis.gov
Website http://classic.ntis.gov/

Reports are available to DOE employees, DOE contractors, Energy Technology Data Exchange representatives, and International Nuclear Information System representatives from the following source:

Office of Scientific and Technical Information
PO Box 62
Oak Ridge, TN 37831
Telephone 865-576-8401
Fax 865-576-5728
E-mail reports@osti.gov
Website https://www.osti.gov/

This report was prepared as an account of work sponsored by an agency of the United States Government. Neither the United States Government nor any agency thereof, nor any of their employees, makes any warranty, express or implied, or assumes any legal liability or responsibility for the accuracy, completeness, or usefulness of any information, apparatus, product, or process disclosed, or represents that its use would not infringe privately owned rights. Reference herein to any specific commercial product, process, or service by trade name, trademark, manufacturer, or otherwise, does not necessarily constitute or imply its endorsement, recommendation, or favoring by the United States Government or any agency thereof. The views and opinions of authors expressed herein do not necessarily state or reflect those of the United States Government or any agency thereof.

ORNL/TM-2021/2207

Environmental Sciences Division

MERCURY REMEDIATION TECHNOLOGY DEVELOPMENT FOR LOWER EAST FORK POPLAR CREEK—FY 2021 UPDATE

Teresa J. Mathews
Melanie A. Mayes
Scott C. Brooks
Chris DeRolph
Alexander Johs
Sujith Nair
Peijia Ku
Leroy Goñez-Rodríguez
Louise Stevenson
Paul Matson
José L. Martínez Collado
Kenneth Lowe
Matt Larson
Andrew Duncan
Tom Geeza
Olawale Alo
Nikki Jones

September 2021

Prepared by
OAK RIDGE NATIONAL LABORATORY
Oak Ridge, TN 37831-6283
managed by
UT-BATTELLE LLC
for the
US DEPARTMENT OF ENERGY
under contract DE-AC05-00OR22725

ACKNOWLEDGMENTS

The authors would like to thank Janice Hensley and Jimmy Massey of URS | CH2M Oak Ridge LLC and Elizabeth Phillips, Laura Hedrick, and Brian Henry of the US Department of Energy's Oak Ridge Office of Environmental Management for their support of mercury technology development in Oak Ridge and their project oversight and support for this document. Additional contributors to various research and technology development activities that provided a basis for the report's evaluations and recommendations include Michael Jones (Oak Ridge National Laboratory). Olivia Shafer (Oak Ridge National Laboratory) was responsible for editing, and her contributions are sincerely appreciated.

CONTENTS

LIST OF FIGURES

LIST OF TABLES

ABBREVIATIONS

AC	activated carbon
AEL	Aquatic Ecology Laboratory
BC	biochar
BCK	Bear Creek kilometer
BCW	Bear Creek watershed
BS	bank soil
DEM	digital elevation model
DMW	diluted mineral water
DOC	dissolved organic carbon
DOE	US Department of Energy
DOM	dissolved organic matter
EFK	East Fork Poplar Creek kilometer
EFPC	East Fork Poplar Creek
FC	First Creek
FR	filtration rate
Hg_D	dissolved mercury
Hg_i	inorganic mercury
Hg_T	total mercury
HRD	historical release deposit
IC_{25}	inhibitory concentration at which there is a 25% reduction compared with the control
LEFPC	lower East Fork Poplar Creek
$MeHg_D$	dissolved methylmercury
$MeHg_T$	total methylmercury
MTF	Mercury Treatment Facility
NDCI	normalized difference chlorophyll index
OF	Outfall
ORNL	Oak Ridge National Laboratory
SM	SediMite
SWAT	Soil and Water Assessment Tool
TSS	total suspended solids
TWRA	Tennessee Wildlife Resource Agency
UAS	unoccupied aerial system
UEFPC	upper East Fork Poplar Creek
Y-12	Y-12 National Security Complex

1. INTRODUCTION

Mercury remediation is a high priority for the US Department of Energy (DOE) Oak Ridge Office of Environmental Management. Mercury contamination in the environment can be found at all three DOE facilities in Oak Ridge, Tennessee, but the greatest environmental risk concern relative to Hg on the Oak Ridge Reservation is likely associated with historical Hg losses at and near the Y-12 National Security Complex (Y-12). Mercury in water and fish from East Fork Poplar Creek (EFPC) downstream of Y-12 exceeds regulatory thresholds. Because of the complexities of Hg transport and fate in the aquatic environment, conventional remedial options for EFPC are highly uncertain.

DOE is using a phased adaptive management approach to Hg remediation at Y-12, with a focus in the next few years on construction of the Mercury Treatment Facility (MTF) to treat the most contaminated Y-12 outfall entering EFPC (DOE 2017a; DOE 2017b). Once operational, the MTF will provide additional protection against inadvertent releases of Hg into the stream from decontamination and decommissioning of Y-12 Hg-use buildings. Although the MTF is anticipated to substantially decrease Hg water concentrations and flux in upper EFPC (UEFPC), research and technology development are needed to develop appropriate and longer-term remedial solutions for the downstream environment. Since late 2014, the Oak Ridge Office of Environmental Management and URS | CH2M Oak Ridge LLC/Restoration Services Inc. have supported DOE's Oak Ridge National Laboratory (ORNL) Environmental Sciences Division staff in conducting field and laboratory studies to develop Hg remedial technology solutions for lower EFPC (LEFPC).

A technology development strategy for LEFPC was developed in 2014 that was consistent with the adaptive management paradigm and DOE's Technology Readiness Level guidelines (Peterson et al. 2015). Initially, a thorough review of the literature was conducted, and site-specific information was collected to develop a broad number of potential technologies that might be applied in LEFPC. An adaptive management approach was then used to focus on technologies that might have the most promise and potential remediation benefit. Field and laboratory studies conducted from 2014 to 2020 have identified the major drivers of Hg flux and bioaccumulation in EFPC and narrowed the list of high-merit technologies that might be of use in remediating the downstream environment.

Whereas previous annual reporting updates for Hg remediation technology development for LEFPC have focused on presenting detailed results from the previous fiscal year, this FY 2021 update takes a comprehensive, higher-level approach to the research and technology development activities conducted since 2014. The report is organized to be consistent with the three tasks defined in the LEFPC strategic plan (Peterson et al. 2015).

- Task 1, Soil and Groundwater Source Control, focuses on addressing downstream Hg sources to the creek (especially floodplain and bank soils [BSs]) and groundwater.

- Task 2, Surface Water and Sediment Manipulation, centers on potential manipulation of instream processes, including the many water and sediment chemistry factors that affect Hg methylation.

- Task 3, Ecological Manipulation, investigates methods to manipulate the food chain at both lower and higher levels of organization to decrease Hg concentrations in fish.

- Task 4, Periphyton Dynamics and Distribution (added in 2021), investigates methods for measuring in situ and remotely sensing periphyton abundance and distribution.

Together, the four study tasks focus on manipulating the key factors that affect Hg concentrations in fish: the amount of inorganic Hg (Hg_i) available to the ecosystem, conversion of Hg_i to MeHg, and bioaccumulation of MeHg through the food web (Figure 1). A major focus of the project has been understanding Hg transport and fate processes in the EFPC system so that targeted, site-specific technologies can be developed.

- Task 5, Watershed Modeling (added in 2019), integrates data collected from field and laboratory studies from Tasks 1–4 to define conceptual and quantitative models for EFPC to inform future remedial decision-making.

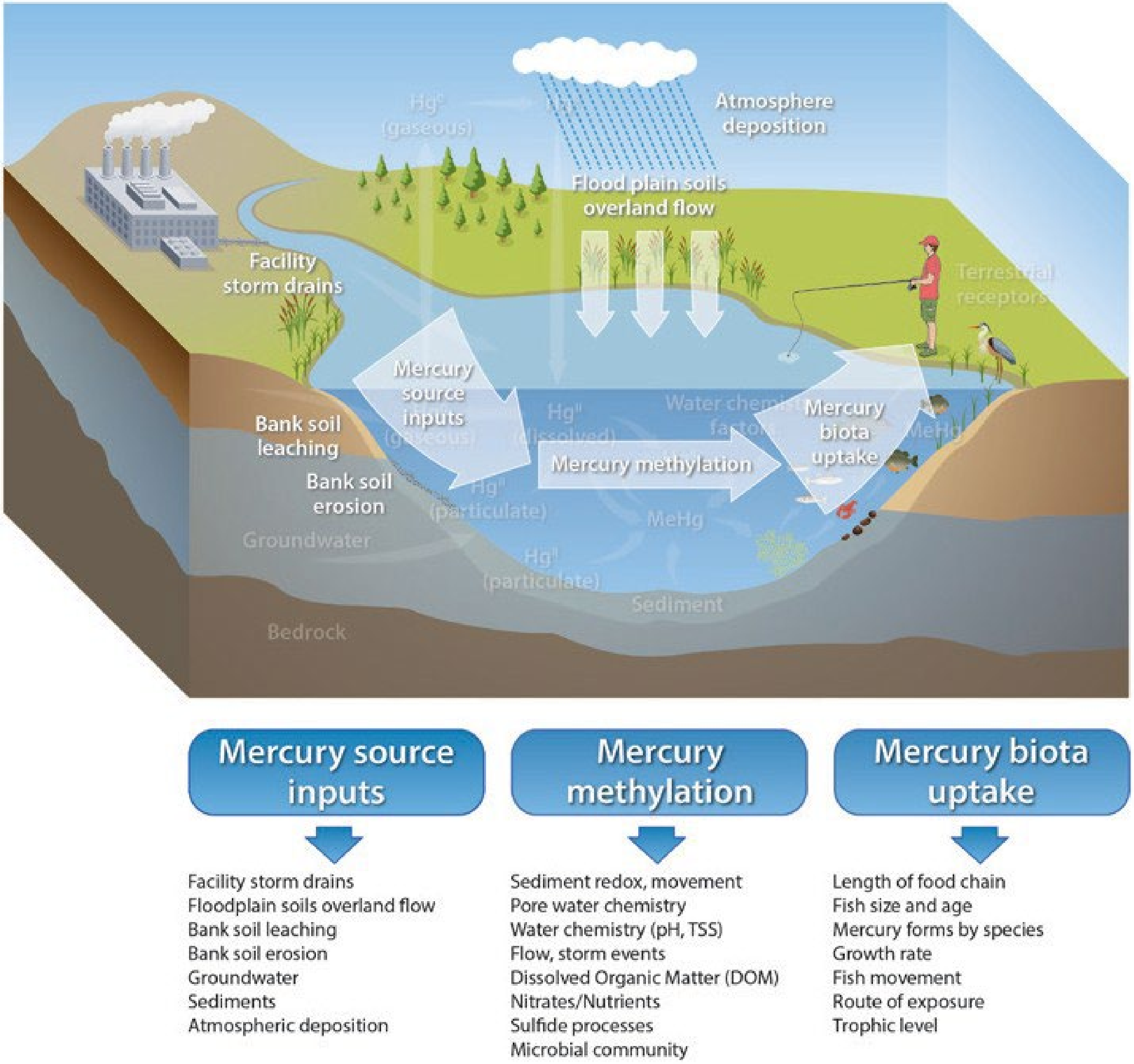

Figure 1. The three major factors affecting Hg concentrations in fish: Hg source inputs to the ecosystem, Hg methylation, and bioaccumulation of MeHg. TSS = total suspended solids. (Source: Peterson et al. 2015)

2. RESEARCH AND TECHNOLOGY DEVELOPMENT RESULTS

Results from the LEFPC Mercury Remediation Technology Development Project in FY 2021, as well as the key findings from previous years, are provided in this section.

2.1 SOIL SOURCE CONTROL AND ENGINEERED SORBENTS

2.1.1 Soil

Field measurements of BS fluxes

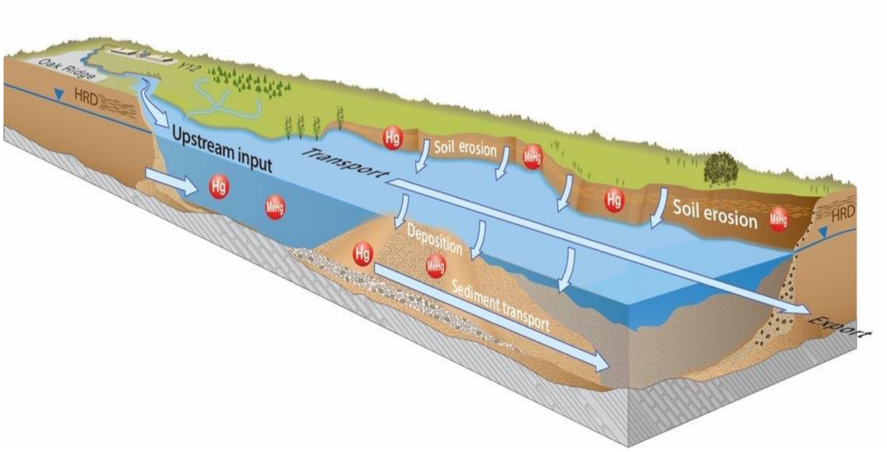

Figure 2. Concept diagram of Hg and MeHg release from stream BSs and incorporation into stream water and streambed sediments. The historical release deposit (HRD) is shown as a distinct layer above the water table. (Source: Peterson et al. 2018.)

Past remedial activities removed more than 34,000 m^3 of floodplain soils with Hg concentrations exceeding 400 mg/kg. However, downstream bioaccumulation and biomagnification of Hg in fish has continued even though releases of Hg from Y-12 have decreased. For several years now, soils and sediments downstream of Y-12 have accounted for most of the annual export of Hg to the watershed (Watson et al. 2016, 2017). As Hg is eroded from bank and floodplain soils, it contributes to the concentration of total Hg (Hg_T) in the water column and sediments where it is transformed into MeHg by microbes or periphyton (Figure 2). Providing technologies to reduce the flux of Hg into the creek is the primary goal of this task. For example, in previous years, the locations of the highest Hg concentrations in stream banks—the historical release deposits (HRDs)—have been identified (Mathews et al. 2019, Dickson et al. 2018).

CONTINUING KEY CONCEPTS

- Improved understanding of Hg dissolution and desorption from creek BSs
- Eroding floodplain soil banks delivering fluxes of Hg into EFPC
- Reducing Hg fluxes into EFPC expected to decrease Hg available for methylation
- Pilot testing of engineered sorbent performance in the field
- New methods to quantitatively measure erosion from creek BSs

This year, the focus involves measuring erosion, which is a key need for modeling Hg release during storm events. Understanding the spatial and temporal patterns of erosion will provide substantial data with which to test and calibrate the watershed model (Task 5). Quantitative measurements of erosion will enable continued prioritization of stream bank locations for future studies and potential remedial investigations (Figure 3).

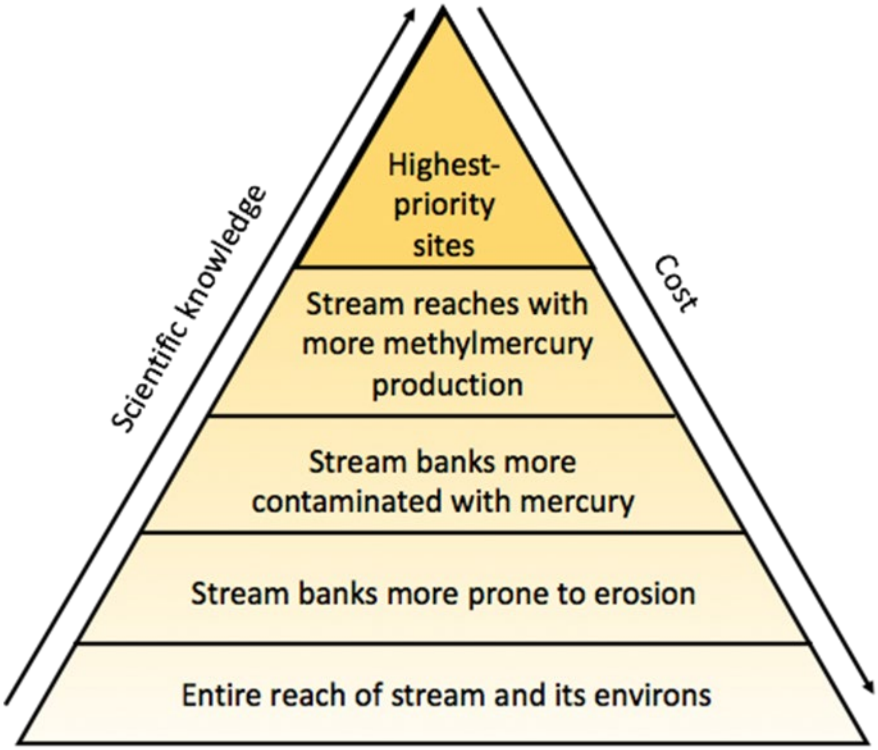

Figure 3. Phased approach for choosing stream bank remedial investigation sites and for determining target areas for remediation. (Source: Peterson et al. 2015.)

2.1.2 Using Lidar to Determine Soil Erosion and Deposition in Creek Banks

A field-portable terrestrial laser scanning device (Leica BLK360) was tested to provide state-of-the-art erosion measurements of EFPC stream banks. The device, based on lidar (light detection and ranging) technology, takes hundreds of thousands of measurements in minutes. The instrument aims a laser beam at an interior fully rotating mirror that reflects the beam outward and then measures the return signals to generate 360° 3D images composed of millions of spatially oriented points (known as a *point cloud*). The instrument's ability to obtain an accurate estimate of the change in volume of the EFPC creek bank (i.e., erosion and deposition) was tested at a set of 9 locations at which erosion pin measurements have occurred for at least 5 years (as detailed by Mathews et al. (2019)).

To test the lidar technology, an exercise was developed to determine that the information from the instrument is reliable. Erosion was simulated by making small excavations along an old roadcut on the Oak Ridge Reservation, and lidar was used to calculate the volume losses (Martínez Collado 2021). Three columns of soil were excavated in three steps each (top, middle, and bottom), and a lidar scan of the entire area was performed after each of the excavations (Figure 4). The workflow for the scanning and volume calculation is shown in Figure 5. The initial and final scans after the removal of the upper third of each of the soil columns are shown in Figure 6, where the material removed is colored in green.

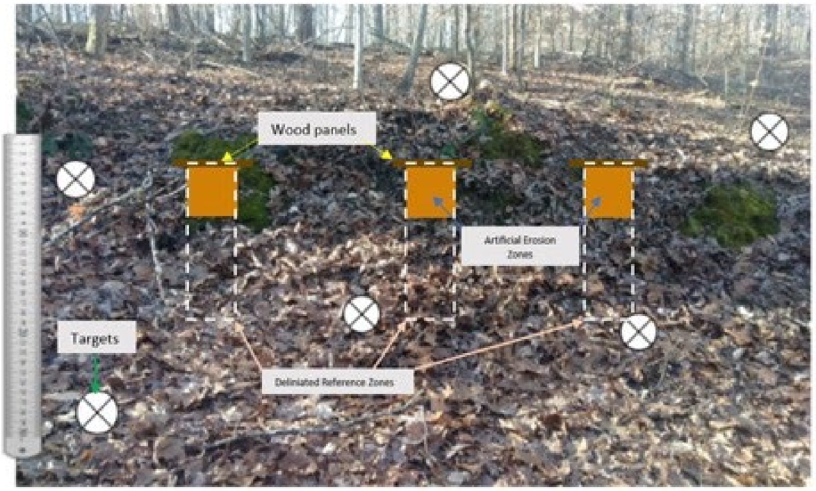

Figure 4. Testing the lidar instrument on the Oak Ridge Reservation. The three columns denoted by the dotted white lines represent three locations of excavation. The orange squares represent three steps of excavation (A shown; B and C not shown) within each column. The targets are to facilitate alignment of the lidar scans in the software.

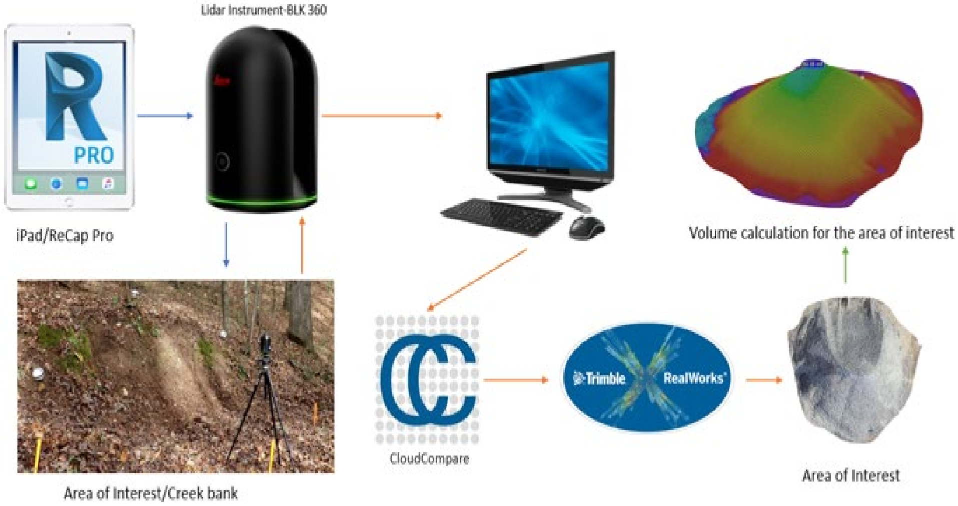

Figure 5. Workflow for using the lidar instrument. The area of interest is scanned with the Leica BLK360, which is operated through the ReCap Pro program on an iPad. The scans are imported into a PC using the ReCap Pro program and trimmed to the area of interest using a freeware called CloudCompare. Then, the trimmed scans are imported into the Trimble RealWorks for registration and are overlayed on one another using the targets to calculate the difference in volume between the initial scan and the final scan.

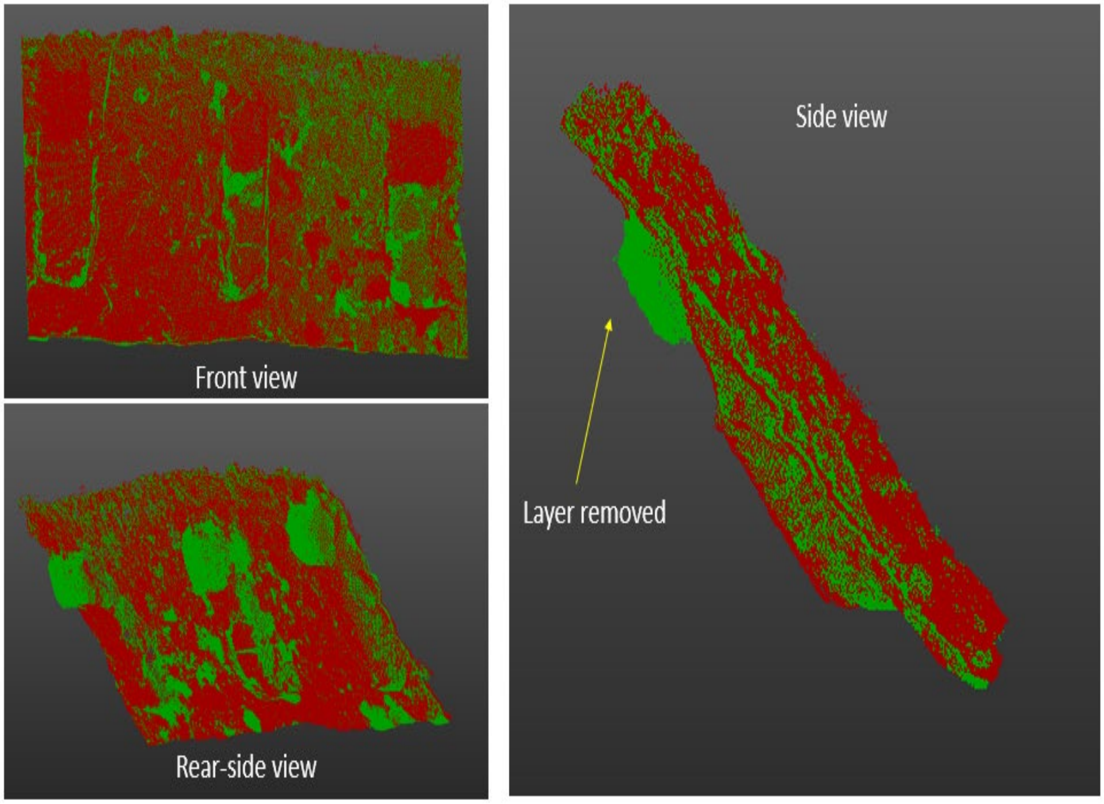

Figure 6. Final processed images from the lidar testing site on the Oak Ridge Reservation shown in Figure 4. The green color indicates the volume differences between the scans taken before and after the excavation.

To determine the accuracy of the technique, the results of the lidar instrument were compared against volumetric measurements of the excavated area (Table 1). The errors of the volume estimates ranged from 3% to 37%. For an additional check, bulk density samples (mass/volume) were also collected from the area before the soil was excavated in each step, and the soil removed was weighed in the field (mass). The errors of the mass estimates ranged from 12% to 38% (results not shown) (Martínez Collado 2021). On the basis of these initial tests and others, the lidar scans provide estimates of erosion with an acceptable amount of error.

Table 1. Comparison between physical volumetric measurements of soil removed and volume calculated from software using the lidar scans for the Oak Ridge Reservation test site.

Section	Measured volume (cm³)	Calculated volume (cm³)	% error
1A	7,079	7,794	10.1
1B	7,079	5,418	23.5
1C	7,079	5,854	17.3
2A	14,160	13,680	3.39
2B	14,160	8,963	36.7
2C	14,160	11,030	22.1
3A	21,238	16,220	23.6
3B	21,238	13,330	37.2
3C	21,238	14,420	32.1

Lidar-based estimates of erosion and deposition in EFPC

The lidar instrument was used to monitor creek bank erosion in EFPC at nine sites that were already associated with erosion pin measurements (Figure 7). Based on knowledge from the previous erosion pin measurements, sites were chosen with both high and low erosion to minimize bias. Lidar scans and new erosion pin measurements were taken simultaneously to compare the two techniques. For each creek bank location, three lidar scans were taken from three locations, covering an area about 10 m wide (Figure 8). The creek banks were scanned, and erosion pin measurements were taken in August and November 2020, and in January 2021. Bulk density measurements were used to translate the volumetric erosion measurements into estimates of soil and Hg mass eroded. Ten evenly spaced samples were collected as a function of depth from each side of each scanned bank and were dried at 85°C for 24 h. Bulk density ranged from 1.28 to 1.74 g/cm³ with an average standard deviation of 0.18 and a total 20 samples per site (Martínez Collado 2021).

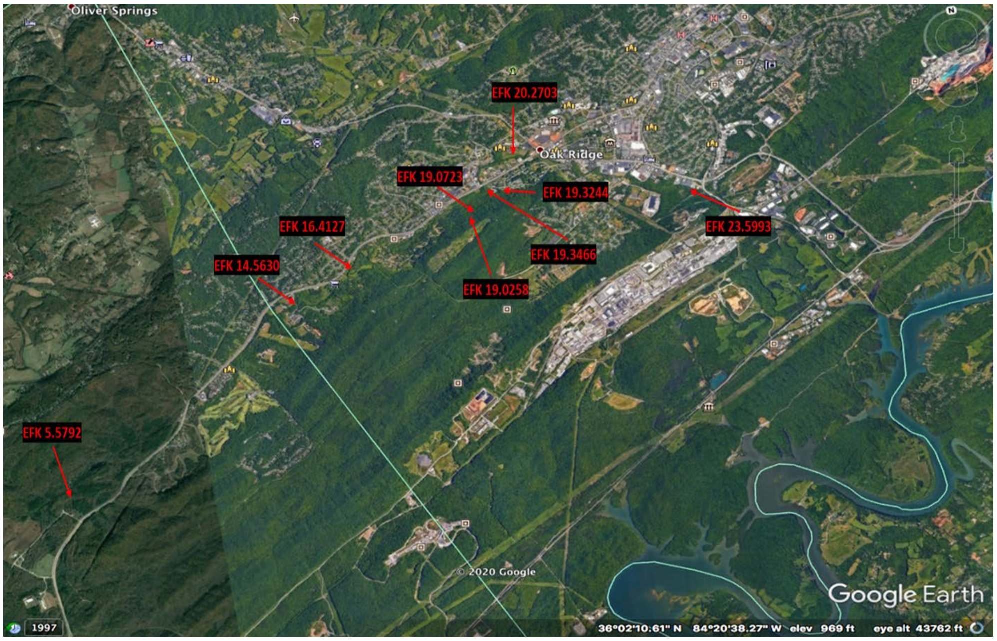

Figure 7. Nine locations of erosion pin measurements chosen for lidar scanning in EFPC in EFPC kilometers (EFKs) above the mouth of the creek.

Figure 8. Configuration of the Leica BLK360 lidar instrument for acquiring scans of EFPC banks. The BLK360 is moved to the three locations for three scans of each stream bank. The white spheres are targets used to align the three scans in the registration software.

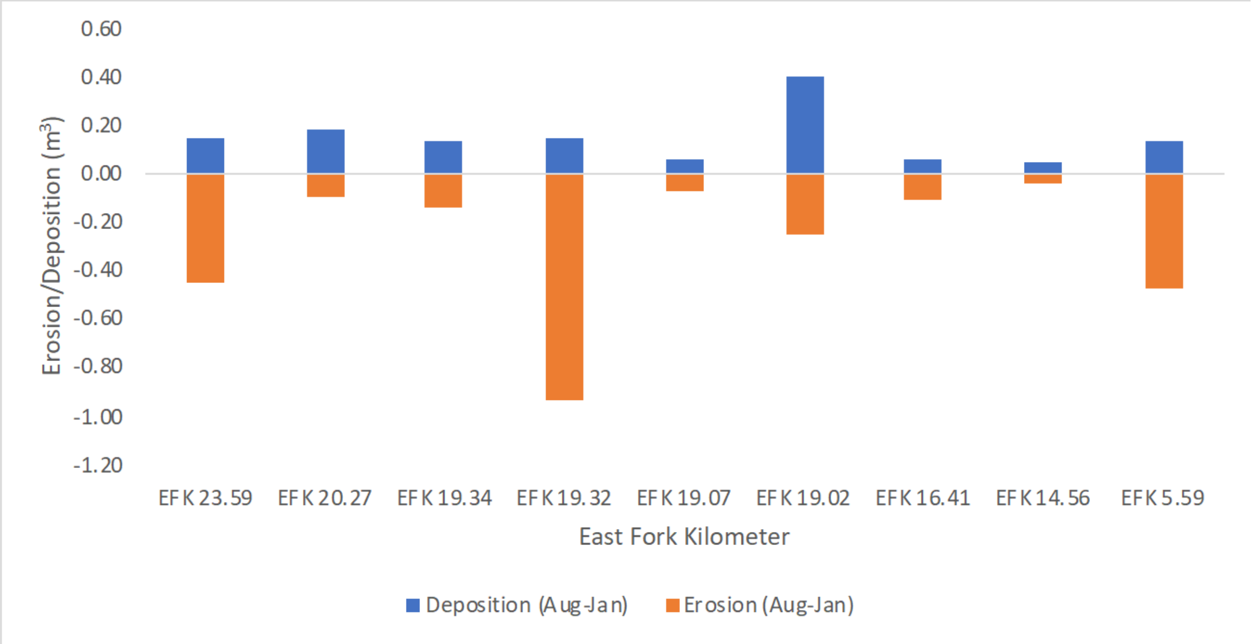

Figure 9. Volume of soil associated with deposition and erosion from the EFPC monitoring sites as measured by lidar in EFPC kilometers (EFKs) above the mouth (August 2020–January 2021).

An outcome of this experiment was an estimate of Hg introduced into the EFPC waters due to erosion and deposition from these sites (Figure 9). Based on estimates of the volume of soil eroded (Table 2) and the bulk density measurements at each site (Martínez Collado 2021), the mass of soil eroded into the creek was estimated (Table 3). Using an average of the different analyses of the Hg concentration per site (Dickson et al. 2018), the total mass of Hg present at each site was also estimated (Table 3). Although few sample sites were studied, both high Hg and high erosion appear to be required for substantial fluxes into EFPC, such as in EFPC kilometers (EFK) 23.59 and 19.32. This finding supports the prioritization concepts of the task (Figure 3).

Table 2. Comparison between soil loss calculated from lidar and erosion pins.

Site	Bank surface area (m^2)	Lidar soil loss (m^3)	Erosion pin soil loss (m^3)
EFK 23.59	10.3	0.29	6.92
EFK 20.27	4.62	0.00	0.29
EFK 19.34	6.73	0.01	1.34
EFK 19.32	7.10	0.79	0.12
EFK 19.07	7.92	0.02	0.00
EFK 19.02	7.20	0.00	0.11
EFK 16.41	5.65	0.06	2.86
EFK 14.56	3.93	0.00	0.00
EFK 5.59	14.2	0.33	0.50

Table 3. Mass of eroded soil and eroded Hg estimated from the lidar technique.

Sites	Hg total (mg/kg)	Mass of eroded soil (kg)	Mass of eroded Hg (kg)
EFK 23.59	1,070	464	0.49599
EFK 20.27	35.9	0.00	0.00000
EFK 19.34	763	8.48	0.00648
EFK 19.32	739	1140	0.84279
EFK 19.07	429	25.7	0.01095
EFK 19.02	582	0.00	0.00000
EFK 16.41	9.05	88.9	0.00081
EFK 14.56	10.9	0.00	0.00000
EFK 5.597	8.10	504	0.00408

For most sites where erosion was substantial, the estimates from the erosion pins greatly exceeded those from the lidar (Table 2). According to previous studies reviewed by Martínez Collado (2021), the most important limitation associated with the erosion pin measurements of streambank erosion is the lack of accuracy for extrapolating erosion measurements across the entire bank surface when the diameter of a pin itself is only 1 cm. Lidar, in contrast, can obtain millions of points (or measurements) from the entire creek bank surface, and therefore can detect both small and large changes within the same surface to provide more representative and realistic data. The drastic difference in the capacity of the two techniques to measure streambank retreat has been compared in another study, and on average, the reported difference was 787%, and values ranged from 22% to 30,003% of soil eroded from a streambank surface (Myers et al. 2019). The same pattern was observed here, where the estimates of erosion from the pins were an average of 64 times higher than estimates from the lidar (Table 2). Consequently, the much higher resolution of the lidar technique results in much more credible estimates of streambank erosion.

In future studies, erosion pins will be used because the effort of taking yearly measurements is minimal and because there is tremendous value in maintaining a data set that began in 2013. However, the initial results are clear in demonstrating the value and superiority of the lidar technology, and that it is the only technique suitable for estimating volume changes of entire streambanks. A long-term data set with the nine preliminary sites will be built, and the number of monitoring sites will be extended to the extent possible. This improved information will enable better modeling of erosional and depositional processes in EFPC (Task 5), and will provide improved estimates of Hg input into EFPC (Table 3).

Release of Hg from BSs—laboratory measurements

The potential release of Hg from EFPC creek banks and specifically the HRD soil layer may contribute disproportionately to elevated Hg levels in downstream environments. Factors controlling the release of Hg species from Hg-contaminated soils are not well understood. Rain events, flooding, and drainage can cause soil erosion and can lead to the release of Hg from soils into the stream. Desorption or dissolution of Hg associated with contaminated BSs may also increase bioavailable Hg, potentially increasing MeHg production in the system. Understanding processes that contribute to the release of Hg from contaminated soils is essential for the development of remediation strategies aimed at limiting Hg mobilization, transport, and conversion to highly toxic MeHg.

The mobilization of Hg from EFPC creek BSs was investigated, and the extent of Hg release into aqueous solution in relation to solid:solution ratio, water chemistry, and time was determined to identify conditions that promote the mobilization of Hg. Two types of Hg-contaminated soils were collected from the creek bank of EFPC at multiple locations (Figure 10). BSs and HRD layer soils were collected from randomly selected locations between EFK 22.46 and 8.41. Creek BS samples were separated into five size fractions to study the effect of particle size on Hg release. Fractionation was carried out by dry sieving the soil samples into five size classes: >2.36 mm, 1.00–2.36 mm, 0.125–1.00 mm, 0.053–0.125 mm, and <0.053 mm.

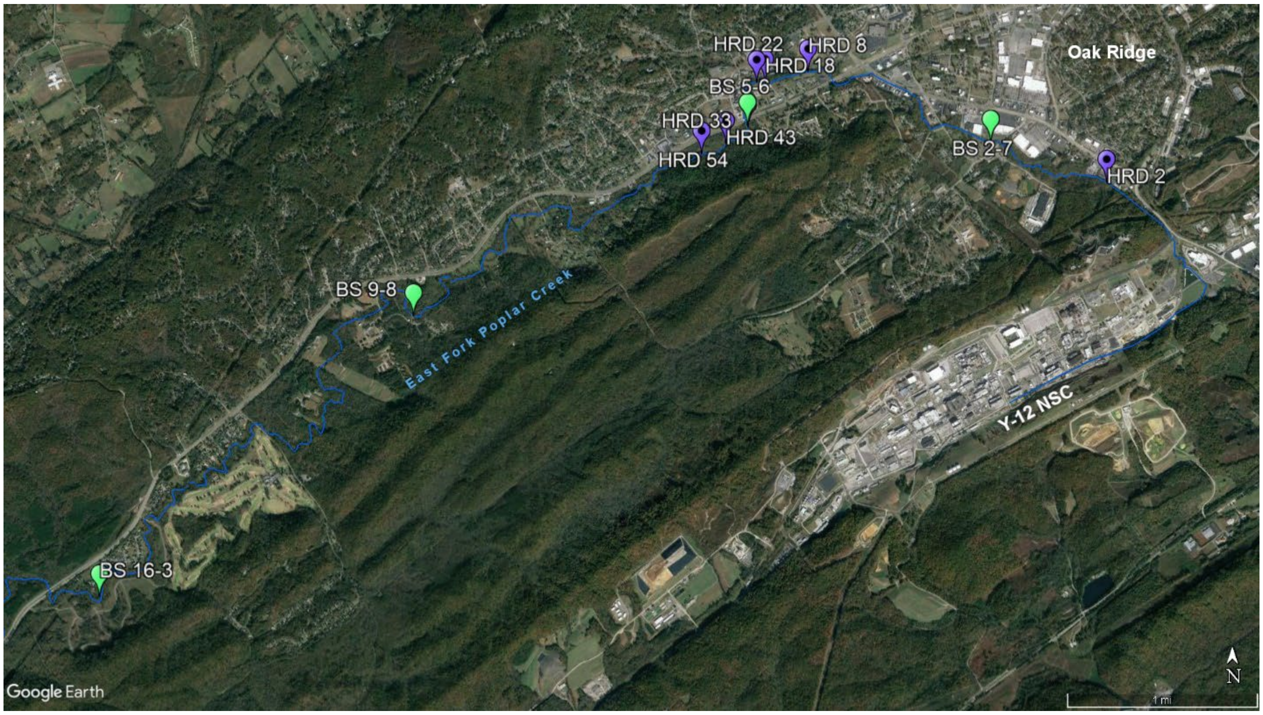

Figure 10. Locations in EFPC for the collection of contaminated creek BSs (green = regular soil, purple = HRD layer soil).

The release of Hg from each individual size fraction was determined in batch experiments with artificial creek water, which mimics the water chemistry of EFPC. Leachable Hg was operationally defined as Hg passing through a 0.2 µm filter. Overall, the fraction of total leachable Hg in all creekbank samples (BSs and HRD) varied by more than an order of magnitude between sampling locations. BSs samples released between 0.011% and 0.040% of Hg (Figure 11A), and HRD soil samples released between 0.017% and 0.17% of Hg (Figure 11B). Individual size fractions contributed between 8% and 41% of the total released Hg, which suggests heterogeneity in the content of leachable Hg among size fractions. To further evaluate the role of individual size fractions on Hg release, the Hg released from each size fraction across all sampled locations was examined. Whereas both the mean and median percentages of Hg released for BS samples were 0.005%–0.008% of Hg (Figure 12A), the mean and median percentages of Hg released from HRD soils were 0.01%–0.03% of Hg (Figure 12B). Overall, the medians for HRD soils tend to lie above their respective means, indicating that the distributions for some size fractions (e.g., >2.36 mm, 1.00–0.125 mm, 0.125–0.053 mm) are skewed toward a higher percentage of Hg released. Among HRD soil samples, the particle size fraction from 1.00 to 0.125 mm generally exhibited the lowest degree of variability with respect to Hg released.

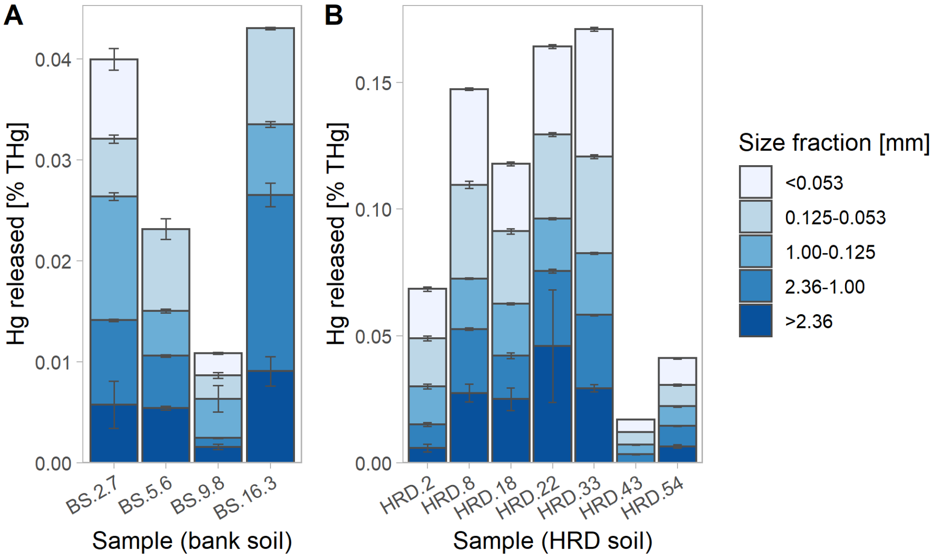

Figure 11. Mercury released from EFPC creek BSs in percentage of Hg in each soil size fraction determined in batch experiments with artificial creek water at a solid:solution ratio of 30 mL/g. (A) Mercury released from BS samples. (B) Mercury released from HRD soil samples.

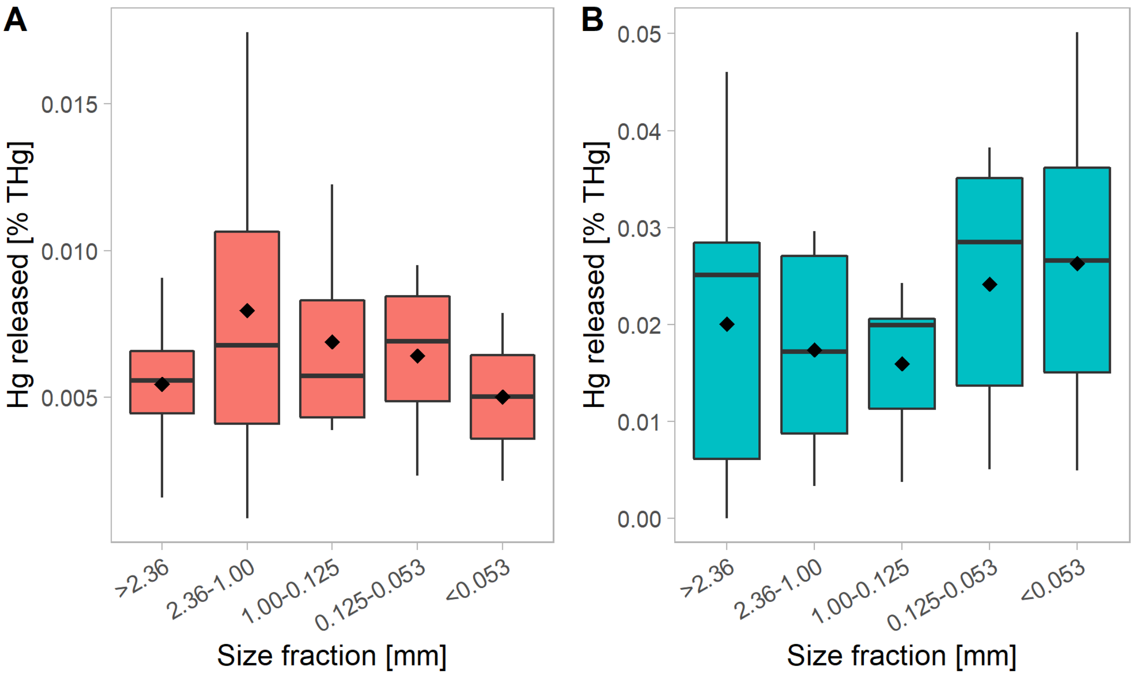

Figure 12. Impact of soil size fraction on Hg release from EFPC soils from batch experiments (solid:solution ratio of 30 mL/g). Mean (black diamonds) and median (horizontal lines) Hg released for each fraction in percentage of soil Hg for fractionated (A) BS samples and (B) HRD soil samples.

The relationship between Hg_T in EFPC stream BSs and quantities released into solution was examined (Figure 13). A linear trend was observed, which is consistent across a wide range of Hg levels for both BS and HRD soil samples. Overall, 0.0175% ± 0.0025% of the Hg in both BS and HRD soils was released into solution under the experimental conditions. Thus, the fraction of Hg released from solution is proportional to the Hg_T concentration in soils.

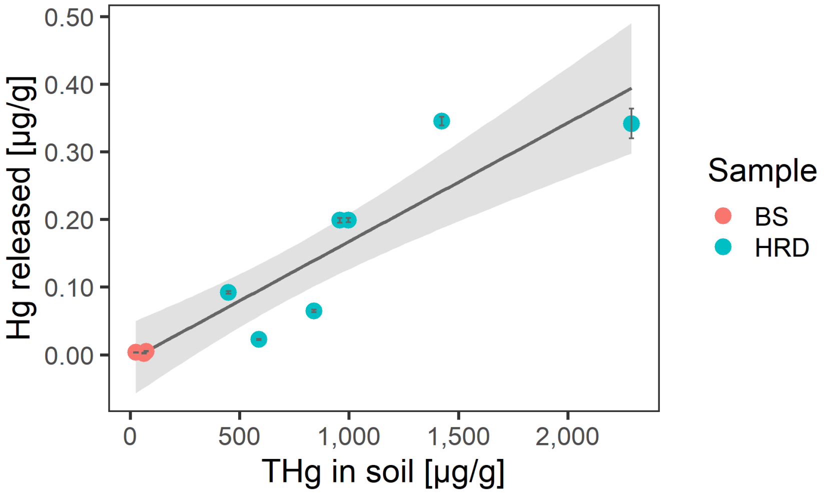

Figure 13. Relationship between the Hg_T concentration in the soil and Hg released into solution (soil size fraction of 1.00–0.125 mm, solid:solution ratio of 30 mL/g) in batch experiments with creek BS samples and artificial creek water over a period of 6 h. The gray shaded area indicates the 95% confidence interval. Error bars indicate standard deviations of analytical replicates. Adjusted $R^2 = 0.83$, slope = $1.75 \cdot 10^{-4} \pm 2.5 \cdot 10^{-5}$, $n = 11$.

Because of the existence of solid HgS minerals in EFPC BSs and HRD soils, dissolution of HgS may contribute to the release of dissolved Hg (Hg_D) species from soils. In the presence of sulfides, the dissolution of HgS minerals can result in the formation of several aqueous species, such as $Hg(SH)_2^0$(aq), HgS_2H^-(aq), and HgS_2^{2-}(aq), which may increase the concentrations of bioavailable Hg species. Although sulfide concentrations can significantly influence Hg release from HgS minerals, the concentration of inorganic sulfide in EFPC surface water is generally very low and ranges from 0 to 0.24 µmol/L. The observed Hg concentrations in the batch experiments cannot be attributed solely to dissolution of HgS minerals. Considering the abundance of organic matter in EFPC soils, the release of Hg(II) into solution may be enhanced by dissolved organic matter (DOM) and organic thiolates found in the soils. In addition, oxidative dissolution of HgS minerals may contribute significantly to the mobilization of Hg_D species in fluvial environments. Although HgS minerals are kinetically resistant to oxidation, reduced sulfide minerals are thermodynamically unstable in the presence of dissolved oxygen. Thus, the rates and extent of Hg release from HgS minerals in the presence of dissolved oxygen can vary widely and will depend on site-specific conditions, such as particle size distribution and concentration, dissolved oxygen concentration, mass transport effects, and water chemistry.

Overall, the results of these studies confirm that BSs are a long-term chronic source of Hg. Generally, Hg concentrations in the soil control Hg flux from contaminated EFPC BSs. Erosion of HRD soils into the creek may result in a fairly rapid release of leachable Hg, increasing the flux of Hg_D into EFPC. Inorganic sulfide concentrations in EFPC water are low, and aqueous Hg concentrations are higher than predicted from aqueous speciation models for HgS and sulfides, suggesting that oxidative dissolution and mobilization by DOM may contribute to the mobilization of Hg in EFPC. HRD soils constitute the largest reservoir of Hg and should be a priority for remediation efforts. Understanding the processes underlying Hg mobilization from soils improves the ability to estimate Hg_D loads to EFPC.

2.1.3 Engineered Sorbents

2.1.4 Determining the Efficacy of Engineered Sorbents in the Field

Soils and sediments can retain Hg contamination for decades, where it is a persistent source that can be mobilized and transformed into MeHg. Sorbent amendments are considered a low-impact alternative to dredging and capping for the remediation of soil and sediments on Hg-contaminated sites (Gilmour et al. 2013); however, the number of field studies involving Hg remediation is still quite small. Engineered sorbents are widely used for the removal of heavy metals from industrial waste streams and for in situ stabilization. Although remediation strategies using in situ amendments have been successfully demonstrated for organic contaminants, the application of sorbent amendments for remediation of Hg remains limited. The objective when using sorbents to stabilize contaminants is to reduce the bioavailability of Hg for methylation and MeHg for bioaccumulation. Studies focused on developing technologies for Hg remediation have thus far involved the use of carbon-based functionalized mesoporous silica, organocation-modified clays, and brass sorbents (Paulson et al. 2014, 2018, Johs et al. 2019). These studies demonstrated that Hg sorption is affected by Hg speciation, particularly in the presence of DOM, which is abundant in EFPC. Here, engineered sorbents were evaluated in the field and the effectiveness in immobilizing Hg in EFPC creek BSs and sediments was determined.

Field sorbent deployment experiment

Experimental details of the deployment were described in the FY 2020 annual report. Sorbent coupons were deployed in creek BSs and sediments at three different locations along EFPC (EFKs 5.0, 18.2, and 22.1). The deployment periods were 6 and 12 months for creek banks and 1, 3, 6 and 12 months for creek sediments. One subset of coupons specifically targeted the HRD. For this set, sorbent coupons were placed in soil layers above, within, and below the HRD.

The results show that Hg sorption is generally proportional to Hg background levels, although significant variability between individual samples was observed. Biochar (BC) and activated carbon (AC) placed within the HRD layer exhibited the highest Hg concentrations (Figure 14).

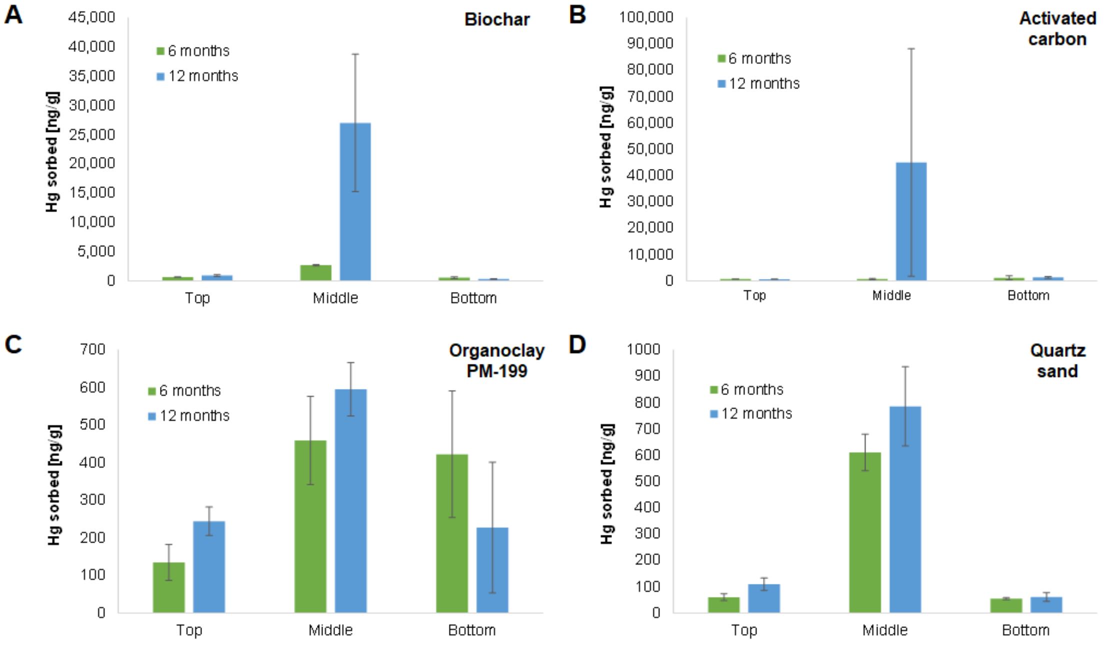

Figure 14. Hg sorption in sorbent coupons deployed in creek banks near EFK 18.2 for 6 and 12 months (ng Hg/g sorbent). (A) BC, (B) AC, (C) Organoclay PM-199, and (D) quartz sand. *n* = 3. Top = above the HRD, Middle = within the HRD, Bottom = below the HRD.

Sorption kinetics

Two essential parameters relevant for assessing sorbent performance in the field are sorption capacity and the rate of sorption. The absorption of a contaminant to a sorbent after deployment progresses until a steady state is reached. At this point, the flux of Hg from the surrounding media (e.g., soil, sediments) to the sorbent is equivalent to the flux of Hg from the sorbent to the surrounding media. The kinetics of Hg adsorption to sorbent materials can be evaluated using empirical models, which are generally applicable to both laboratory and field experiments. If the experimental data are obtained under identical conditions, the parameters obtained from fitting the experimental data to the empirical adsorption model facilitate a direct comparison of sorbent performance. Here, the concentration of Hg in the sorbents coupons was followed over time at each field site and the Hg sorption kinetics were obtained by fitting the experimental data to a pseudo–first-order rate equation (Equation 1).

$$Q = Q_{max}(1 - e^{-k_t \cdot t})\ . \tag{1}$$

The kinetic parameters—adsorption density at equilibrium (Q_{max}) and absorption rate (k_t)—were obtained from a fit to the rate equation (example shown in Figure 15). Across all field sites and conditions, the highest Q_{max} values were observed for BC (1,051–2,549 ng/g) followed by AC (628–2,231 ng/g) (Figure 16), and k_t values ranged from 0.11 to 1.32 mo^{-1} (Figure 17).

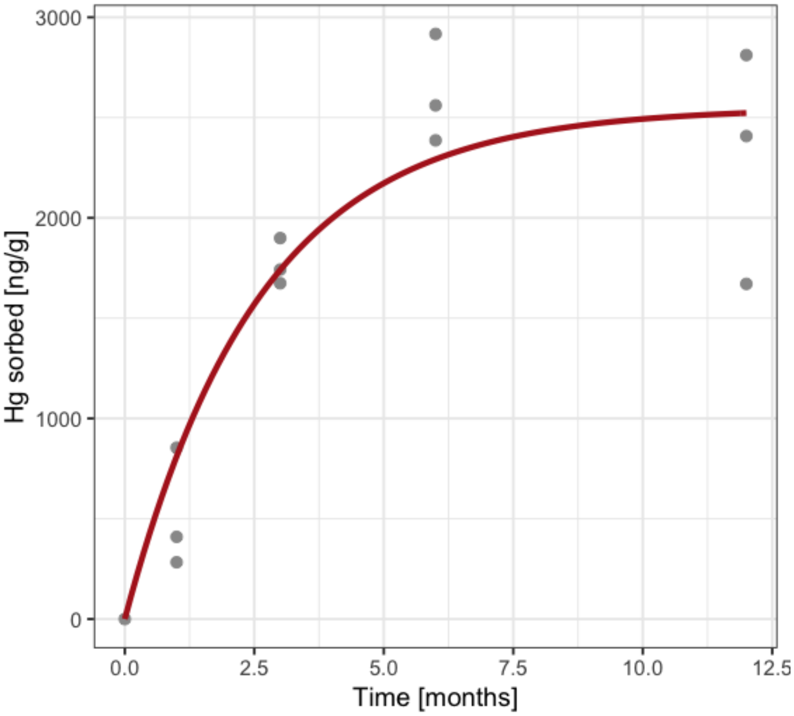

Figure 15. Example of Hg sorption kinetics for BC in creek sediments at EFK 5.0. Red line: fit to pseudo–first-order rate equation. $Q_{max} = 2{,}549 \pm 229$ ng/g, $k_t = 0.38 \pm 0.10$ mo^{-1}.

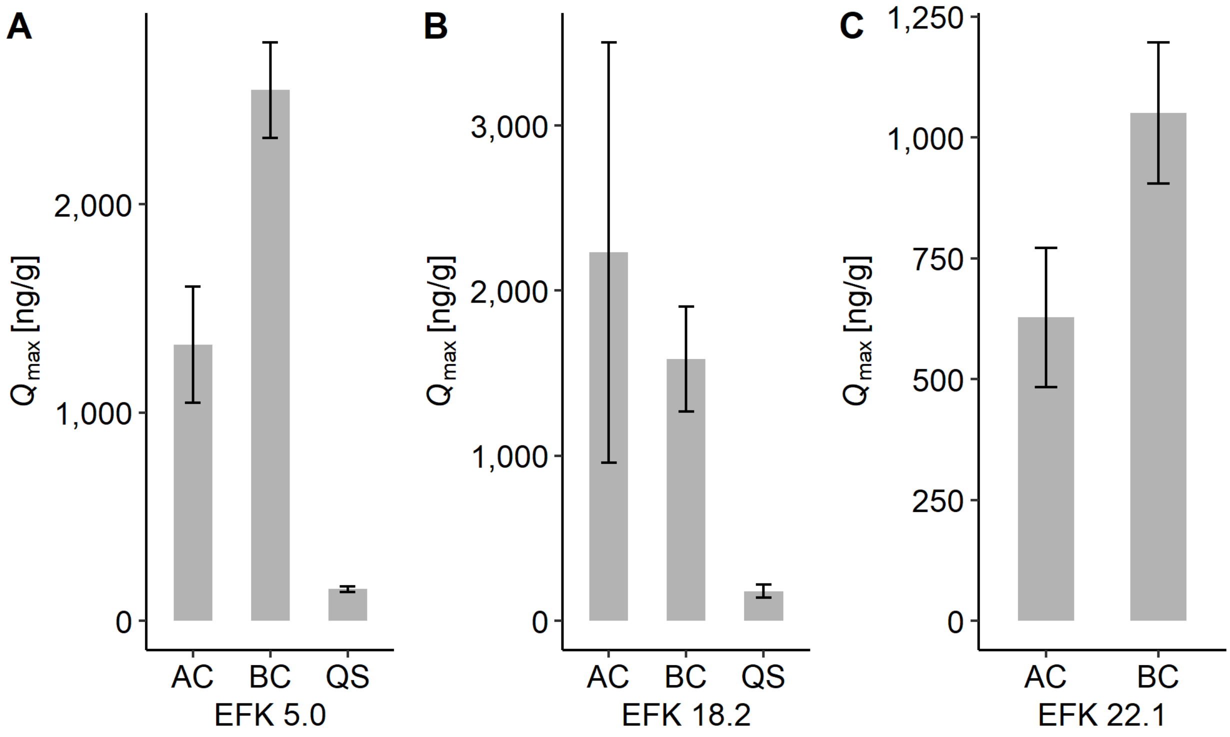

Figure 16. Comparison of *Q_{max}* parameters obtained for sorbent coupons deployed in creek sediments. (A) EFK 5.0, (B) EFK 18.2, and (C) EFK 22.1. QS = quartz sand (nonreactive control). The fit for QS did not converge. Error bars represent the standard error of the fit.

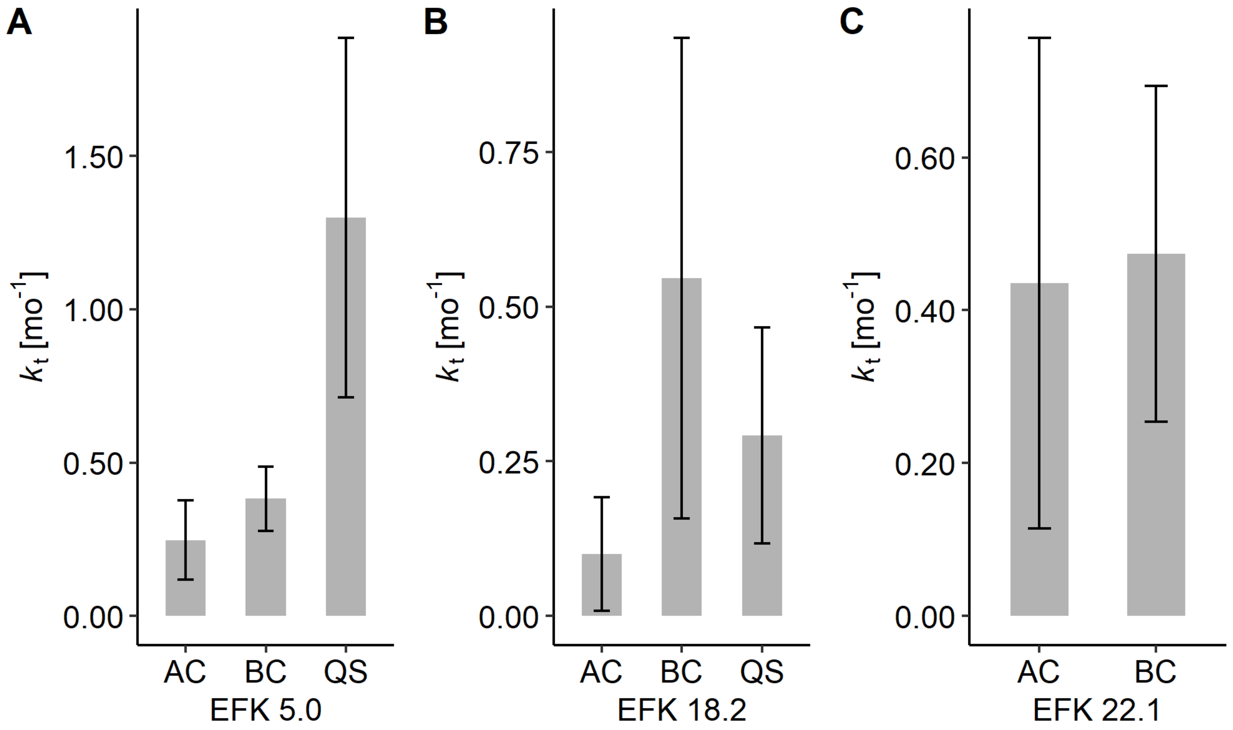

Figure 17. Comparison of k_t parameters obtained for sorbent coupons deployed in creek sediments. (A) EFK 5.0, (B) EFK 18.2, and (C) EFK 22.1. QS = quartz sand. The fit for QS did not converge. Error bars represent the standard error of the fit.

Despite significant variability between individual samples and sites, several trends are evident from the analysis of the sorbent coupon data. The placement of sorbents has a strong influence on Hg sorption. Saturation of sorbents occurred more rapidly in the sediment than the bank soil coupons. Sorbent coupons deployed in sediment reached concentrations of >2,500 ng Hg/g sorbent for BC. In comparison, Hg concentrations in sorbents deployed in creek banks were significantly less effective, except for sorbent coupons placed in the HRD layer, where Hg concentrations reached a maximum of 26,000 ng Hg/g sorbent for BC after 12 months. These results suggest that contaminant transport effects have a major influence on the effectiveness of sorbent materials. Sorbent coupons submerged in creek sediments were less transport-limited and could reach a steady state over a period of 12 months or less, whereas sorbent coupons in creek banks may not have reached their sorption capacity. However, in HRD soils, sorbent Hg concentrations were still three orders of magnitude higher relative to other EFPC BSs. The current results indicate that future studies should focus on Hg exchange processes between soils and sorbents, which will inform potential sorbent deployment strategies that maximize the effectiveness for immobilizing Hg in bank stabilization efforts.

2.1.5 Soil Research and Technology Development Needs

The overarching goal of this task is to understand how soils contribute to the flux of Hg in EFPC (i.e., Hg concentrations and soil erosion). In previous years, the areas of BSs having the highest Hg and MeHg concentrations and that thus constitute the highest priority for future investigations and potential remedial activities (Mathews et al. 2019, Dickson et al. 2018). In general, the region of the creek banks with the HRD layer have the highest concentrations. This year, lidar technology was developed to determine the extent of erosion of stream banks. In just a few minutes, lidar technology can collect thousands of points to represent the spatial configuration of a stream bank. A comparison of images of the same stream bank collected at different periods of time was used to determine changes in the volume of stream banks (i.e., erosion and deposition). Nine locations that have been monitored using erosion pins since 2013 or 2015 were chosen, and the results of the two techniques were compared. Lidar estimated between 0 and 0.79 m^3 of soil lost among the nine sites, whereas erosion pins suggested between 0 and 6.92 m^3 of soil was removed—a substantial difference. The lidar technique is much more accurate and sensitive than the erosion pins because it interrogates the entire stream bank at high resolution, whereas erosion pins are 1D point measurements. The extrapolation of the erosion pins from point measurements likely results in unrealistic 3D estimates of erosion. The lidar estimates corresponded to a range of 0 to 1,140 kg of soil removed by erosion considering all nine sites, which corresponds to 0 to 0.8 kg of Hg. Going forward, the yearly long-term data collection will be maintained using the erosion pins because the cost is minimal, but the routine use of the lidar technique will be prioritized and expanded to provide more accurate erosion estimates and to provide needed data for the watershed modeling task. This research demonstrates the continued importance of understanding the major sources of Hg in terms of both concentrations and erosional fluxes from the stream BSs (Figure 3).

Batch studies using contaminated HRD and creek BSs demonstrate that the release of Hg from the HRD soils is greater than for the remainder of the creek BSs. The release of Hg is proportional to the amount of Hg in the soils, however, and a linear dissolution model is appropriate to describe the data over a broad range of Hg concentrations. There are also strong differences in release as a function of particle size. The results of the Hg release experiments show that the BSs are a long-term source of Hg to EFPC and that Hg releases rapidly from the soils once introduced into water. Most Hg in EFPC soils are HgS compounds, but inorganic sulfide concentrations in EFPC water are low, and aqueous Hg concentrations are higher than predicted from aqueous speciation models for HgS and sulfides. This suggests that oxidative dissolution and mobilization by DOM may also contribute to the mobilization of Hg from EFPC soils. The results continue to suggest that the HRD soils are a significant reservoir of Hg and therefore constitute a high priority for remediation.

Regarding the engineered sorbents, a field deployment of small coupons demonstrated substantial uptake of Hg by all sorbents in both creek banks and EFPC waters, where concentrations increased over a year. There is variability, but Hg sorption appears to be proportional to Hg background levels. Equilibrium Hg concentrations appear to be highest when placed within the HRD soils, second highest when placed in EFPC, and lowest when placed in non-HRD creek BSs. These results are attributed to limitations in transport when the sorbents are placed in soils versus in water. However, extremely high Hg concentrations such as found in the HRD soils still result in transmission of high concentrations of HRD into the coupons. Therefore, future studies should focus on the kinetics and mechanisms of Hg exchanged between soils and sorbents, since these may be key to the effectiveness of sorbents when deployed in the field.

Additional lab-scale studies with the engineered sorbents and real EFPC water are still needed. In general, the chemistry of Hg in EFPC is dominated by complexation with DOM, which cannot be readily replicated. The presence of DOM induces aqueous complexation with Hg and dramatically decreases the reactivity of Hg with the sorbents. In addition, the role of oxidative dissolution of HgS minerals present in EFPC bank and HRD soils should be more thoroughly evaluated. Therefore, a new set of column studies are planned for the Aquatic Ecology Laboratory (AEL) involving the three most promising engineered sorbents and EFPC water, which will enable an improved understanding of long-term sorbent performance under conditions of Hg speciation that are found in EFPC. Overall, insights from the present laboratory and field studies will enable the development of technologies that can be deployed to minimize flux of Hg from contaminated BSs to EFPC.

2.2 SURFACE WATER AND SEDIMENT MANIPULATION

2.2.1 Importance of Surface Water Chemistry

The goal of water chemistry manipulation technologies is to disrupt Hg transport and loading, aqueous partitioning, methylation, and exposure/bioaccumulation mechanisms. By decreasing Hg_T and total MeHg ($MeHg_T$) concentrations in surface water, the expectation is for a decreased flux of these constituents and their concentration in fish tissue. New water chemistry manipulation strategies and technologies are sought to effectively decrease Hg and MeHg concentration and bioavailability and bioaccumulation while limiting unintended negative impacts to the environment.

During the previous 12 months, efforts within the surface water and sediment manipulation task focused on the rating curves at our monitoring stations and updating flux estimates along EFPC. Additionally, experiments were initiated to measure the effects of adding sorbents to sediments on Hg and MeHg accumulation in benthic invertebrates. A summary of our findings is presented here.

2.2.2 Improved Rating Curves and Updated Flux Estimates

Rating curves are empirical equations that relate water level in the stream to volumetric water discharge. Combined with concentration measurements, the discharge estimates enable the calculation of material flux. Rating curves are not static relationships—they depend on channel geometry, which changes with bed scour and deposition events that occur with flooding, bank erosion, and active stream management. Therefore, rating curves need to be verified and remeasured frequently. Additionally, accurate rating curves are developed by making measurements over a broad range of flow conditions to capture both base flow and storm flow. For a stream the size of EFPC, base flow discharge can be made via wading measurements—physically standing in the stream with instruments to make the measurements. However, even in EFPC, wading measurements are not safe under storm flow conditions.

Undiagnosed errors in rating curves for EFPC that date back to the early 1980s resulted in upstream flood discharge estimates being much greater than downstream discharge estimates. Consequently, water and material balances and fluxes that depend on those discharge estimates were unreliable, leading to incorrect source attribution and misunderstanding of essential components of watershed behavior.

During FY 2021, data collection and analysis of the rating curves were completed at monitoring stations at EFKs 16.2 and 5.4. The new data were collected with an acoustic Doppler current profiler and covered a broad range of flow conditions. The rating curve measurements at EFK 5.4 were in excellent agreement with measurements made in 2012–2014 and with those recorded by the US Geological Survey (period of record 1983–1988) (Figure 18A). Undiagnosed errors in historical rating curve measurements made at EFK 16.2 resulted in upstream flood discharge estimates being much greater than downstream discharge estimates. The new rating curve developed at EFK 16.2 (Figure 18B) resolves the previous discrepancies and flood discharges increase with downstream distance from EFK 23.4 to 5.4. The acoustic Doppler current profiler data are in good agreement with previous measurements for creek stage less than 4 ft, but above that water level, the measurements diverged, suggestive of the errors described earlier. The rating curve for EFK 16.2 exhibits a break point at creek stage of ~8.2 ft, likely because of a change in control structure for creek flow, which was likely associated with overbank flooding.

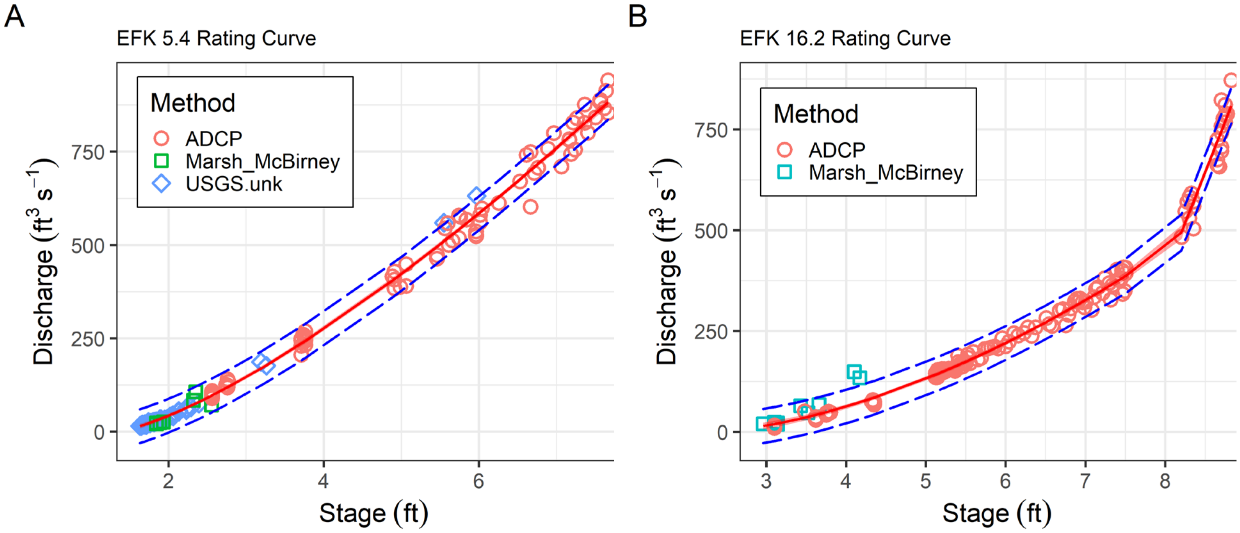

Figure 18. Rating curves for (A) EFK 5.4 and (B) EFK 16.2 relating creek stage to volumetric discharge. Symbols represent data points, the solid red line represents the rating curve fit to the data, the red ribbon represents the 95% confidence band, and the dashed blue lines represent the 95% prediction band. ADCP = acoustic Doppler current profiler; Marsh_McBirney = Marsh-McBirney flow meter; USGS.unk = data collected by the US Geological Survey, measurement method unknown.

Previously, Hg and MeHg flux estimates were reported along EFPC under base flow conditions (Mathews et al. 2019). Given the improved rating curve for EFK 16.2, the flux estimates were updated. As reported before, about 80% of the Hg flux measured at EFK 5.4 originates from diffuse legacy sources in the watershed outside of Y-12 (Figure 19). In contrast to the previous estimate, the majority of that Hg enters EFPC downstream of EFK 16.2, whereas it was estimated to come from the reach upstream of EFK 16.2 previously. The Oak Ridge Wastewater Treatment Facility (ORWTF) is not a significant source of Hg. Most of the Hg added below EFK 16.2 is associated with suspended particles, suggesting that the additional Hg comes from bank erosion or suspension of bed sediments. Nevertheless, the potential sources of that Hg are not known and merit further investigation. To date, the team's studies of BSs (Dickson et al. 2018) and bed sediments (Brooks et al. 2017) have not identified areas of high Hg concentration.

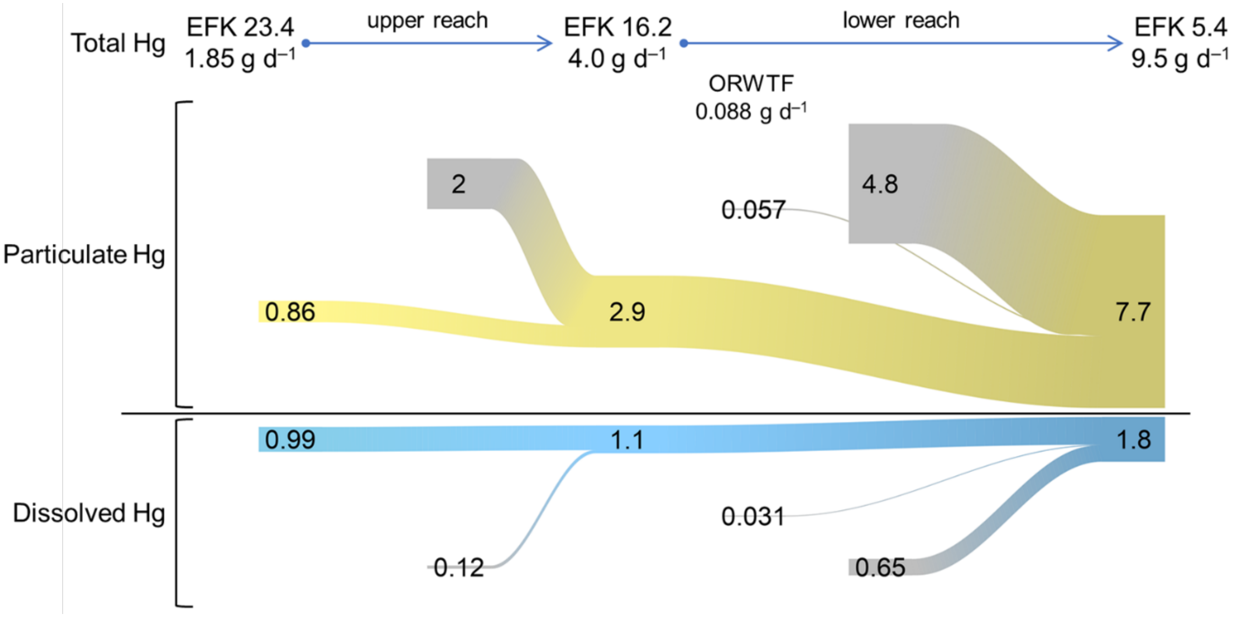

Figure 19**. Base flow Hg flux estimates along EFPC.**

The updated flux estimates for MeHg were similar to previous estimates except a larger proportion of the MeHg flux at EFK 5.4 is attributed to the reach downstream of EFK 16.2 (65% compared with 51%–57%) (Figure 20). In contrast to the estimates for Hg, most of the MeHg flux is dissolved as opposed to associated with suspended particles.

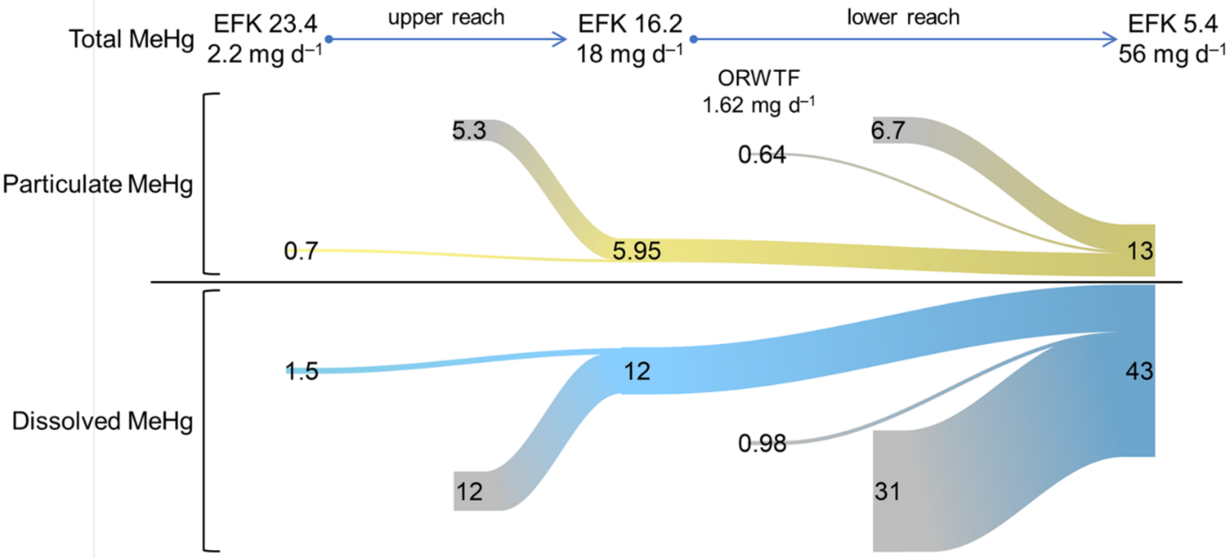

Figure 20**. Base flow MeHg flux estimates along EFPC.**

2.2.3 Effects of Carbon-based Sorbents on Hg and MeHg Bioavailability to Blackworms

In relatively simple water-sorbent systems to which a known Hg-methylating bacterium was added we demonstrated that the sorbents did not change the amount of MeHg produced (Muller and Brooks 2018).

Nevertheless, the sorbents showed varying degrees of effectiveness in removing MeHg from the aqueous phase and accumulating the MeHg on the solid phase (Muller et al. 2019). Sequestering MeHg onto the sorbents has potential implications for decreasing MeHg concentrations in biota. However, real sediments in EFPC have different geochemistry than the defined lab media and host diverse microbial communities rather than pure bacterial strains. These differences make it difficult to extrapolate the previous results to sediment-water-sorbent systems.

To better understand the effects of sorbent amendments to sediment on MeHg uptake by biota, mesocosm experiments were initiated using sediment and water from EFPC. California blackworms (*Lumbriculus variegatus*; Figure 21), a common benthic invertebrate found in North America, were added to the sediment and water as a representative receptor at the base of the food chain. The blackworms live in and eat the sediment, which passes through their digestive tract to extract nutrients. If sorbent addition to sediments lowers MeHg concentrations in blackworms, it would represent a break in the MeHg bioaccumulation and biomagnification pathway and may ultimately lead to lower MeHg concentrations in fish.

Figure 21. *Lumbriculus variegatus* (California blackworms) used in the bioaccumulation tests. The worms are 1–1.5 mm wide and 4–6 cm long and are pictured with guts full of sediment.

Mesocosms were established by collecting fresh sediment (wet-sieved in the field to pass through a 1 mm sieve) and water from EFK 5.4 and were added to buckets (2,100 g wet sediment, 2.6 L water). Sorbents were blended into the sediments at a loading of 5% of the sediment dry weight (i.e., 105 g). Five treatments were established: a negative control, which received no sediment amendment; a positive control, which received clean quartz sand; and three sorbent treatments, one each for BC, SediMite (SM), and AC. Nine replicate mesocosms were established for the negative and positive controls, and eight replicates were established for each sorbent. The mesocosms were equilibrated for one week, after which 180 blackworms were added to each bucket. Two weeks later, the mesocosms were destructively sampled and the worms, interstitial porewater, surface water, and sediments were collected for analyses. Worms were depurated (residual sediment and sorbent in gut removed) in clean water prior to preservation and analysis.

After two weeks of exposure in the sediment-water-sorbent mesocosms, Hg_T concentration in blackworms was significantly lower ($p < 0.05$) in sorbent treatments than in the control treatment (Figure 22A). BC, AC, and SM reduced Hg bioaccumulation by 25%, 49%, and 82%, respectively, relative to the control. Total Hg (water + sediment + worms) in mesocosms was similar among the different treatments and did not correlate with the differences in Hg concentration in the worms.

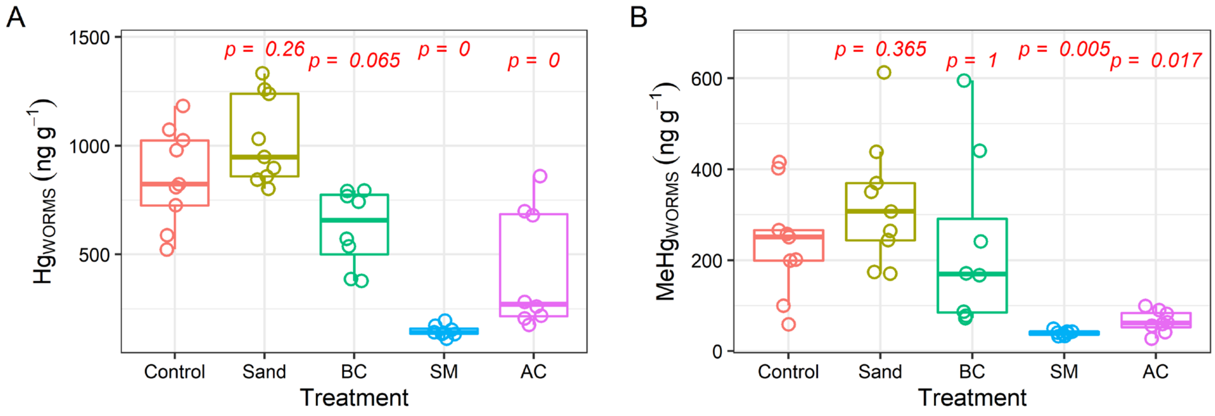

Figure 22. Total Hg (A) and total MeHg (B) in blackworms after two weeks in sediment-water-sorbent mesocosms. Box limits indicate the 25th and 75th percentiles, horizontal line in each box represents the median, upper whisker extends from the 75th percentile to the largest value no further than 1.5×IQR (IQR = 75th percentile – 25th percentile), and the lower whisker extends from the 25th percentile to the smallest value at most 1.5×IQR.

Control = negative control, sand = positive control, BC = biochar, AC = activated carbon, SM = SediMite. The numbers in red above each treatment are the resulting *p*-values using Dunnett's test to compare each treatment with the control.

Additionally, $MeHg_T$ in blackworms was significantly ($p < 0.05$) lower in the AC and SM treatments than in the control (Figure 22B). AC and SM decreased MeHg concentration in blackworms by 75% and 85%, respectively, relative to the control. In contrast to the results for Hg_T in the mesocosms, $MeHg_T$ (water + sediment + worms) was lower in the AC and SM treatments than in the control, sand, or BC treatments. Total MeHg in the AC and SM treatments was 42% and 61% lower, respectively, than in the control.

Lower net MeHg production in the sorbent treatments confounds the interpretation of the results. Lower MeHg in the worms for the AC and SM treatments may be due to lower MeHg production, stronger MeHg binding to the sediment-sorbent mixture, lower bioaccessibility of MeHg associated with sediments, or a combination of these. To compare the strength of MeHg binding to sediments, the sediment-water partitioning coefficient (K_{SW}) was calculated as

$$K_{SW}(L\ kg^{-1}) = \frac{[MeHg]_{sediment}(ng\ kg^{-1})}{[MeHg_D]_{PW}(ng\ L^{-1})}, \tag{2}$$

where $[MeHg_D]_{PW}$ = dissolved MeHg ($MeHg_D$) concentration in the interstitial pore water. There were no significant differences in K_{SW} among treatments, suggesting that simple sorption of MeHg onto the sediment-sorbent mixture alone does not account for the differences in MeHg content of the worms. Next, the bioaccessibility of MeHg to the worms was assessed by calculating the bioaccumulation factor (BAF), which normalizes the MeHg concentration in worms to the MeHg concentration in sediments, as

$$BAF(kg\ kg^{-1}) = \frac{[MeHg]_{worms}(ng\ g^{-1})}{[MeHg]_{sediment}(ng\ g^{-1})}. \tag{3}$$

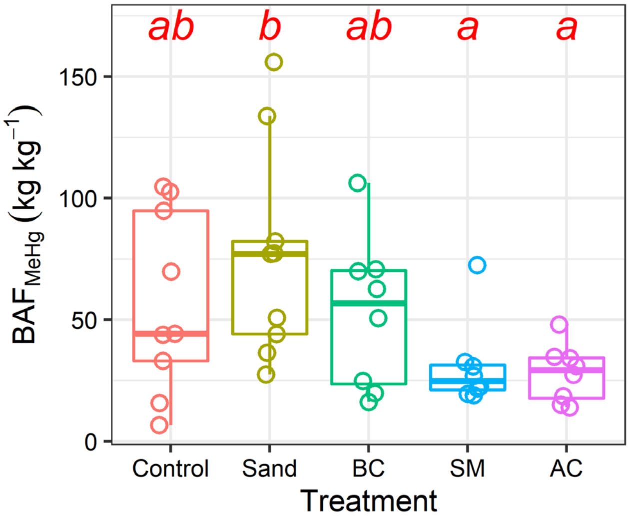

Figure 23. MeHg bioaccumulation factor (BAF) for each treatment. Letters above each treatment indicate groupings using Tukey's honest significance difference test. BC = biochar, AC = activated carbon, SM = SediMite.

The MeHg BAF was similar for AC and SM, and these two treatments had lower and less variable BAF than the other three treatments (Figure 23). The high variability in the control, sand, and BC treatments obscured a clear demonstration of significant differences among treatments. Still, these results suggest that AC and SM decrease MeHg uptake by the blackworms and that the lower MeHg concentration in worms was not simply an artifact of the lower MeHg concentration in those treatments.

There were moderate to strong correlations between MeHg in the worms and MeHg_D in the surface water and pore water (Figure 24). This correlation highlights several aspects of the sorbent additions to the sediments. First, it illustrates the positive relationship between MeHg concentrations in water and the worms. In other words, it supports the hypothesis that decreasing MeHg concentrations in water can lower MeHg concentrations in low trophic levels, which should ultimately result in lower MeHg concentrations in fish. Second, Figure 24 shows that both SM and AC treatments cluster in the lower left quadrant of the parameter space, showing the effectiveness of these two materials. Porewater MeHg_D concentration in the AC treatment spanned a large proportion of the MeHg_D concentration observed for all treatments, but MeHg concentration in worms remained well below that of the control, sand, and BC treatments (Figure 24B).

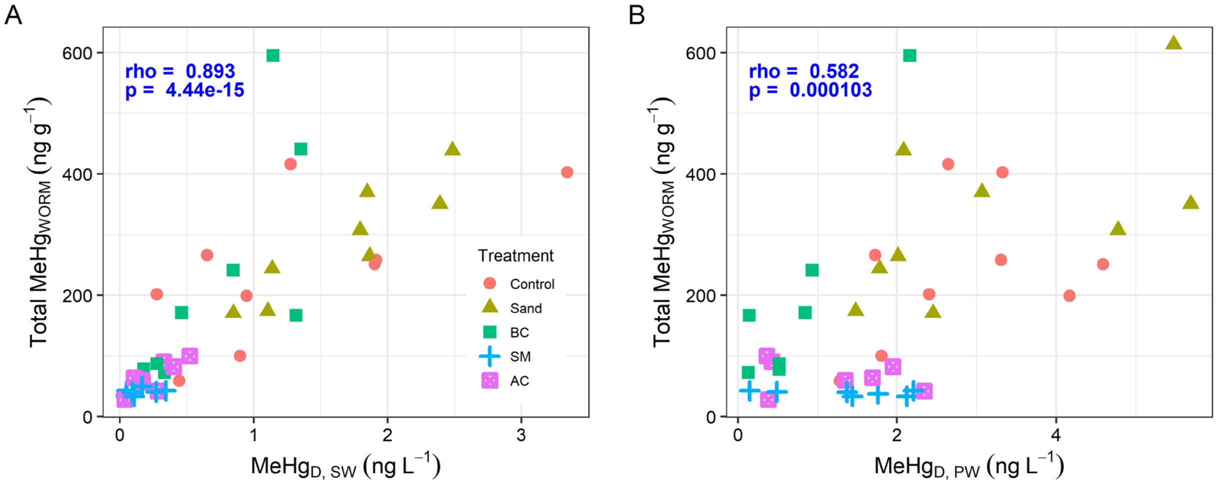

Figure 24. Relationship between MeHg concentration in worms and MeHg_D concentration in (A) surface water (SW) and (B) interstitial porewater (PW) in the sediment-water-sorbent mesocosm tests.

Potential for unintended consequences resulting from sorbent amendments to sediments

The results hold promise that sorbent amendments to sediments can lower MeHg concentration in benthic invertebrates by lowering net $MeHg_T$ concentration in the system and decreasing MeHg bioconcentration. At the same time, unintended negative consequences to the ecosystem as a result of directed interventions should be avoided. The sorbents used, particularly the BC and SM, release other solutes to solution that could alter the biogeochemistry of the system and potentially enhance MeHg production over longer periods (Table 4). For example, the BC releases significant amounts of dissolved organic carbon (DOC) and lesser amounts of nitrate, sulfate, and phosphate to solution. SM releases significant amounts of DOC, sulfate, nitrate, and phosphate. The DOC, if readily consumed by microorganisms, can result in the onset of anoxic conditions required for Hg methylation. Additionally, the addition of sulfate to the systems may favor the activity of sulfate-reducing microorganisms. Many of the known Hg-methylators are sulfate-reducing microorganisms. Several experiments were initiated to understand the potential effects of solute release from sorbents on the sediment-water system.

Table 4. Solute release from sorbents used in the mesocosm tests. All units are mg kg–1 dry weight.

	DOC	**Nitrate**	**Sulfate**	**Phosphate**	**Chloride**
Sand	15		5		20
BC	480	22	111	50	80
AC	5		6	2	20
SM	495	67	504	126	1,030

First, experiments were initiated to quantify the biodegradability of the DOC leached from the BC and SM. DOC is leached from the sorbents and subsequently inoculated with surface water from EFPC. The DOC concentration is measured after 16 days incubation in the dark at room temperature as an indicator of DOC availability to the native microbiota in the creek. Early results show that 56%–92% of the BC DOC is consumed over a 16 day period. There was no loss of BC DOC in uninoculated replicates. These results suggest that the DOC released by the BC could be used to stimulate microbial activity in the sediments. Additional testing is needed to determine whether this results in enhanced MeHg production.

Second, another set of sorbent-water-sediment mesocosms was established that will equilibrate for 90 days before blackworms are added. This will allow for a better assessment of the longer-term effects of sorbent additions on sediment biogeochemistry and net MeHg production, which will provide a better understanding on the efficiency of sorbent amendments in longer-term field application.

Ancillary experiments

To better understand the responses of blackworms when exposed to Hg-contaminated sediment-water systems and how sorbent additions may affect those responses, several ancillary experiments were conducted. For example, 96 h Hg toxicity tests using the blackworms were conducted to measure their sensitivity to aqueous Hg concentrations. The experiments were conducted in the absence and presence of DOM (added as 2 mg L^{-1} DOC) because DOM can strongly bind with Hg and change its chemical behavior. The results indicate a lethal concentration 50 (LC_{50}, concentration expected to kill 50% of the organisms) of 50 µg L^{-1} in the absence of DOM (Figure 25). Notably, when DOM was included in the experiments, there was no lethal toxicity. The precise mechanism by which DOM reduces toxicity is not understood because the mesocosms tests demonstrated that the blackworms take up Hg in the presence of DOM. Similar experiments are planned for MeHg.

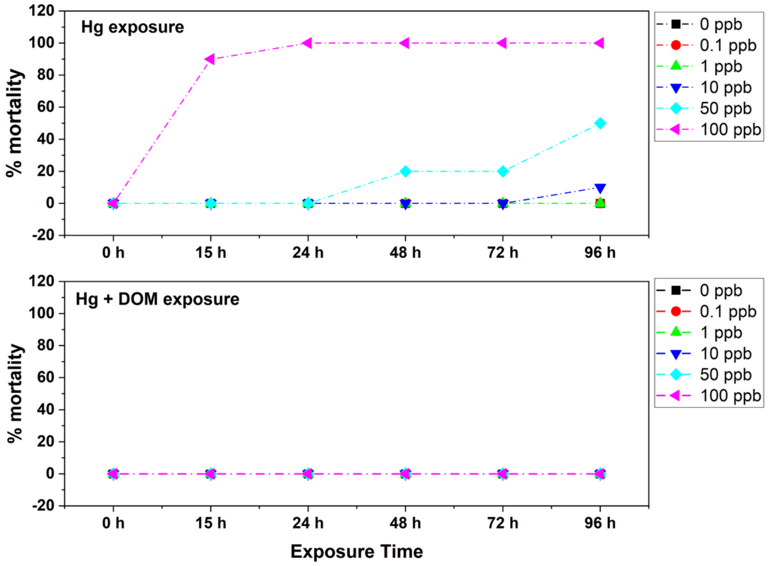

Figure 25. Blackworm mortality as a function of Hg_i concentration in the (upper panel) absence and (lower panel) presence of DOM added at a concentration of 2 mg L^{-1} DOC. In the absence of DOM, 50% of the worms are expected to die at a Hg concentration of 50 µg L^{-1}. Adding DOM eliminated Hg toxicity to the worms.

Also, experiments are being conducted to quantify the rate at which the worms take up Hg and MeHg and the rates at which Hg and MeHg are eliminated from the worms. Results of these experiments will lend further insight into whether the sorbents slow the rate of accumulation and will also indicate how quickly part of the food chain might respond once Hg and MeHg concentrations in EFPC water decrease.

2.2.4 Mercury Dynamics Altered by Increasing Temperatures and Flow Management

Stream restoration activities for EFPC included the initiation of a flow management program in 1996, in which water from a nearby lake was pumped to the head of the creek. Regular water sampling was conducted for two years along the length of EFPC during active flow management and for five years after flow management stopped. Total Hg and total MeHg concentration and flux decreased in the uppermost reaches of EFPC that were closest to the point of water addition. However, under a similar range of creek discharge, Hg_T and $MeHg_T$ concentrations increased at the downstream monitoring location after flow management stopped (Figure 26). Most water quality parameters, including DOC concentration, remained unchanged after flow management termination. However, $SUVA_{254}$, a measure of DOM composition, increased and coincided with increased Hg_D concentration and flux and decreased Hg solid-water partitioning coefficients throughout EFPC. Higher $SUVA_{254}$ and Hg_D concentration have potential implications for increased bioavailability and MeHg production. Total and dissolved MeHg concentrations increased in the lower reaches of EFPC after the end of flow management, and these increases were most pronounced during spring and early summer when biota are more susceptible to exposure and uptake. A general warming trend in the creek after active flow management ended likely acted in concert with higher Hg_D concentration to promote higher MeHg concentration. Total and dissolved MeHg concentrations were positively correlated with water temperature above a threshold value of 10°C. Concentration changes for Hg and MeHg could not be accounted for by changes in creek discharge that accompanied the cessation of flow management. In addition to the changing DOM composition in-stream, other watershed-scale factors likely contributed to the observed patterns since these changes occurred over months rather than instantaneously after flow management stopped. However, similar changes in MeHg have not been observed in a tributary to EFPC (Brooks et al. 2021).

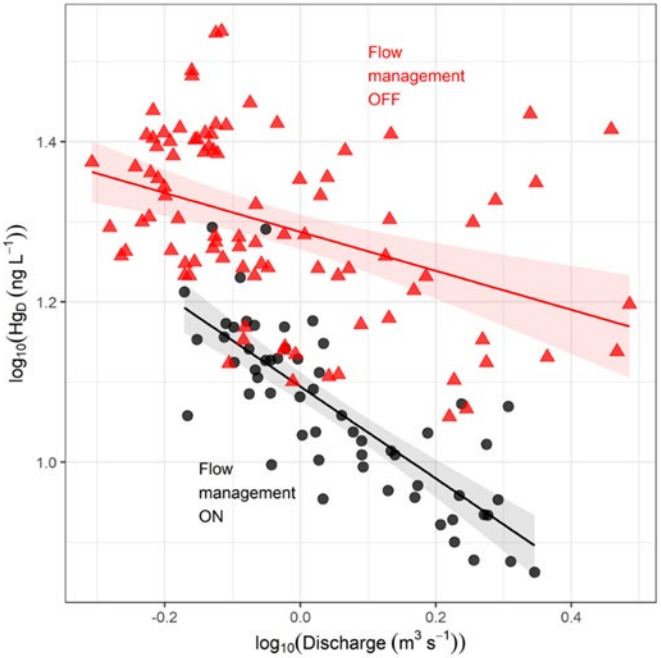

Figure 26. Dissolved Hg concentration versus discharge at EFK 5.4 during the time flow management was in effect and after the program was stopped. Over a similar range of flow conditions, Hg_D concentration is substantially higher after flow management stopped. The slopes of the lines are significantly different ($p = 9.05 \times 10^{-4}$).

2.2.5 Future Needs: Surface Water and Sediment

Within this task are several areas of continuing and new research that are warranted. Ambient water quality and flow data have supported new information on Hg and MeHg concentration, flux, and possible sources in the LEFPC watershed. Updated mass balance calculations indicate the lower reach of the study area harbors unidentified sources of legacy Hg that make significant contribution to the Hg load in the creek. An improved understanding of the locations, sources, and controls on Hg loading in the lower study reach is a pressing need. Additionally, both downstream monitoring points have experienced significant trends of increasing Hg and MeHg flux, demonstrating the dynamic changes that occur in the system without direct engineered intervention. Continued monitoring will strengthen the baseline record of flux and concentration against which system responses to natural forcings, directed actions (e.g., MTF construction, bank stabilization), and unintentional events (e.g., spills, leaks) can be compared.

Material flux under storm flow conditions: The previous mass-balance–based flux estimates have been limited to base flow conditions because of incomplete rating curves at our monitoring stations. However, updated rating curves will support monitoring storm-driven high-flow events at multiple locations to quantify Hg and MeHg flux along EFPC. Planning is underway to coordinate and stage in preparation for sampling future storm events. These storm sampling studies will provide data on Hg_T and $MeHg_T$ flux and dynamics during storm-driven flood events that provide insight into material sources, sinks, and watershed function.

Effect of sediment amendments on Hg transformations: Studies on the effects of sediment amendments on Hg transformations and bioaccumulation will continue, including the longer-term studies described earlier. Results to date suggest that when sorbents are blended into the sediments, less net MeHg is produced. It is not known if this is because of less Hg methylation, enhanced MeHg demethylation, or a combination of the two. Experiments will be conducted to address this question.

Additional sediment-water-amendment experiments are planned using other amendments. For example, we hope to use a novel proprietary amendment manufactured by Albemarle Corporation specifically for application in Hg-contaminated systems. Finally, evaluation of Mn-oxide amendments merits further investigation. These materials can poise the sediment redox at values that inhibit the activity of Hg-methylating microorganisms and may catalyze abiotic MeHg demthylation. However, the broader implications of both the Albemarle materials and Mn oxides on the ecosystem are poorly understood.

Nutrient effects on MeHg concentration. Finally, EFPC has a very high nutrient load and is mesotrophic to eutrophic along its length with respect to both nitrogen and phosphorous because of point source and diffuse discharges to the creek. Earlier and ongoing in situ studies in EFPC suggest that nutrient amendments alter microbial community composition and Hg methylation (Carrell et al. 2021). Controlled laboratory studies are being planned to better understand these potential effects that may lead to watershed best management practice recommendations to control MeHg concentrations in EFPC. These studies will rely heavily on the use of the renovated stream mesocosms and delivery of real creek water that are part of the AEL upgrade.

2.3 ECOLOGICAL MANIPULATION

2.3.1 Role of Ecology in EFPC

The primary goal of ecological manipulation in EFPC is to examine strategies to reduce Hg bioaccumulation in fish in EFPC through sustainable biological or ecological manipulations. In contrast to virtually all other metals, Hg (especially in its organic form, MeHg) biomagnifies, or becomes increasingly concentrated, as it is transferred through aquatic food chains to higher trophic levels, namely to fish. Consequently, the consumption of Hg-contaminated fish is the primary exposure route to humans. Therefore, the National Recommended Water Quality Criterion for Hg is based on a fish tissue concentration rather than an aqueous Hg concentration because the tissue concentration (0.3 mg/kg) is considered to be a more consistent indicator of exposure and risk to humans and aquatic life.

Although most Hg in the environment is Hg_i, a small proportion of Hg_T is microbially transformed to MeHg in the aquatic ecosystem. Anoxic-reducing environments such as wetlands are considered Hg-methylating hot spots, where large amounts of Hg_i are methylated by sulfate- and iron-reducing bacteria. However, research has highlighted freshwater streams as sites of Hg methylation with favorable conditions for methylation including increased temperatures, the presence of certain filamentous algae, and the presence or absence of certain organic nutrients (Tsui et al. 2010). The methylation of Hg from periphyton- and macrophyte-associated bacteria has also highlighted additional opportunities for Hg methylation within freshwater streams (Acha et al. 2012).

Methylmercury readily crosses cell membranes and binds with proteins, forming complexes that mimic essential amino acids. For this reason, MeHg is highly bioaccumulative, becoming incorporated into protein-rich tissues (e.g., muscle; typically, MeHg is >95% of the Hg_T in fish fillets) with long residence times. In aquatic animals, MeHg uptake rates from water and assimilation efficiencies from food are high, while elimination rates are low, leading to progressively increasing concentrations within organisms over time. This also leads to progressive concentrations of Hg within food chains as MeHg is transferred from one trophic level to the next.

One of the challenges to effective remediation at Hg-contaminated sites is that while Hg body burdens in fish are often more closely linked to aqueous MeHg than Hg_i concentrations (Tom et al. 2010), MeHg production is not easily predicted or controlled. For example, in systems contaminated by atmospheric deposition with low aqueous Hg_T concentrations (<10 ng/L), a correlation exists between Hg(II) and MeHg concentrations (Kelly et al. 1995). However, in point source–contaminated systems, waterborne Hg_i concentrations can range over several orders of magnitude, while MeHg concentrations in water and biota seldom differ by more than 10-fold (Southworth et al. 2004). Decreasing aqueous Hg_i concentrations and loading might often be a more achievable remediation goal than decreasing MeHg concentrations, but this approach has led to mixed results in terms of responses in fish bioaccumulation. A number of source control measures have resulted in rapid responses in lake or reservoir fisheries (Joslin 1994, Turner and Southworth 1999), but examples of similar responses in Hg-contaminated stream ecosystems are less common. Stream systems might actually be more susceptible than lakes to Hg bioaccumulation, highlighting the need to better understand the ecological drivers of Hg bioaccumulation in stream-dwelling fish (Chasar et al. 2009, Ward et al. 2010). Although Hg_i concentrations play a part in determining overall Hg concentrations in fish, methylation efficiencies and food web pathways are also important in determining fish tissue concentrations.

Effective Hg remediation in EFPC requires not only an understanding of the nature and magnitude of Hg inputs but also knowledge of the extent to which these inputs must be controlled to achieve the desired reduction of Hg contamination in biota necessary to meet the National Recommended Water Quality Criterion. However, because Hg is accumulated predominantly through the food chain rather than through aqueous exposure, understanding food web structures and transfer pathways for Hg to fish is a key component to successfully implementing strategies to mitigate Hg bioaccumulation. Uptake at the base of the aquatic food chain (e.g., algae/periphyton, invertebrates) is the most important concentration step for Hg (with Hg concentrating more than 10,000-fold between water and algae). However, although the relationship between Hg concentrations in water and fish has been characterized, transfer pathways from the base of the food chain remain largely unknown.

Resolving key questions concerning the role of ecological interactions in driving fish tissue Hg concentrations in EFPC required quantifying Hg and MeHg inventories throughout the food webs at various locations throughout EFPC (Peterson et al. 2015). Biological Hg and MeHg inventories serve several purposes for site management and technology development, including (1) supporting conceptual model development and site characterization; (2) assessing exposure and risk evaluation; (3) informing site prioritization; (4) informing remediation selection and design; and (5) providing baseline information for performance, compliance, and long-term monitoring and evaluation. The conceptual model for remediation targets in EFPC assumed that Hg accumulation in fish in EFPC was proportional to waterborne Hg_T. This assumption was the basis for derivation of the aqueous Hg target guiding Comprehensive Environmental Response, Compensation, and Liability Act efforts in UEFPC (200 ng/L). Over the past decade, aqueous Hg_T concentrations in UEFPC have fluctuated because of various activities (e.g., operation of the Big Spring Water Treatment System, storm drain cleanouts, cessation of flow augmentation, demolition activities), and fish do not appear to be responding to these changes. Lack of a clear response suggests that the relationship between Hg_i concentration and the MeHg production/bioaccumulation observed in UEFPC in the 1990s is not a straightforward, linear relationship.

To address these needs and fill knowledge gaps, biota throughout the food web at four biological monitoring sites in EFPC (EFKs 23.4, 18.2, 13.8, and 6.3) were sampled. Additionally, MeHg and $MeHg_T$ were quantified, and trophic status was estimated using stable isotopes of carbon and nitrogen to assess the relative importance of food web dynamics in determining Hg bioaccumulation in fish. A food web model was examined to identify the most important factors affecting Hg concentrations in fish, and based on the results, laboratory experiments were conducted to examine the potential effects of adding native freshwater mussel species to EFPC.

2.3.2 The Role of Mussel Filtration on Hg Dynamics

A statistical examination of the factors influencing Hg concentrations in fish in EFPC showed that, unsurprisingly, aqueous MeHg concentrations are significantly and positively correlated with Hg fish tissue concentrations. This examination, which considered 30 years of community structure data in EFPC, also showed that the percentage of collector filterers in the community is significantly and negatively correlated to Hg in fish (Figure 27). This finding led to an ongoing investigation of the potential of introducing native freshwater mussels into EFPC to mitigate Hg bioaccumulation in fish.

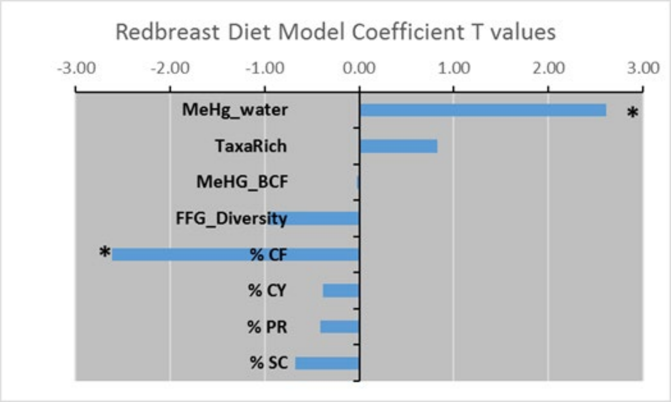

Figure 27. Linear mixed model developed for redbreast diets under different scenarios. The predictor variables for MeHg in the diet were aqueous MeHg, taxonomic richness, bioconcentration factors (BCF), functional feeding group (FFG) diversity, percentage of collector filterers (CF) in the invertebrate community, percentage of crayfish (CY), percentage of predators (PR), and percentage of scrapers (SC). Values shown are T value coefficients. Asterisks denote significant values.

Freshwater mussels are filter feeders, filtering large volumes of water over their gills to remove algal and detrital particles for nutrition. Because mussels filter particulates from the water column, they can significantly affect water quality (Figure 28) and thus play a critical role in freshwater ecosystems. These mussels are of interest in EFPC because they can affect Hg bioaccumulation throughout the food web by exerting effects on periphyton, DOM, methylating bacteria, and aqueous Hg concentrations. ORNL scientists are working closely with the Tennessee Wildlife Resource Agency (TWRA), which has a mission of restoring these native species to Tennessee waters. The reintroduction of native mussels to EFPC could mitigate Hg bioaccumulation and risks in this stream and provide other ecosystem services, including water quality improvement and propagation of sensitive native species.

Figure 28. Demonstration of clam and mussel filtration. All aquaria were initially inoculated with the same algal cell concentration. The aquarium on the left had no bivalves, the aquarium in the middle had Asian clams (*Corbicula fluminea*), and the one on the right had rainbow mussels (*Villosa iris*) and young pocketbook mussels (*Lampsilis ovata*). The photo was taken 2 h after adding algae.

To determine the potential impacts of mussel filtration on Hg dynamics in EFPC, (1) filtration or clearance rates of mussels under different environmental conditions, (2) Hg removal rates, and (3) effects of mussel filtration on Hg methylation rates had to be determined. In past years, field investigations were performed to quantify Hg bioaccumulation rates, as well as laboratory investigations to quantify filtration rates (FRs) for different species under different environmental conditions.

The field deployment results showed that Hg bioaccumulation rates in Asian clams (*Corbicula fluminea*) were much higher in the spring than in the winter (Mathews et al. 2019). This suggests a positive effect of water temperature on FRs. Most biological and metabolic rates are affected by temperature. Microbial activity is also affected by temperature, and Hg methylation rates (which are controlled by microbes) and concentrations are therefore also higher in the spring in EFPC than in the winter. These results suggest a seasonal component to the efficiency of Hg removal but that filter feeders would remove Hg at times critical to Hg methylation. The results also show that unlike fish bioaccumulation patterns, clam bioaccumulation is proportional to aqueous Hg concentrations. There is a strong spatial pattern of higher Hg concentrations upstream where aqueous concentrations are highest and significant decreases with increasing distance downstream.

Field collections of resident Asian clams in EFPC show a similar spatial pattern to deployed clams, with the highest Hg_T concentrations at upstream sites within EFPC and decreasing concentrations with distance downstream (Mathews et al. 2019). Unlike fish tissue, where Hg is predominantly found as MeHg, clams accumulate high concentrations of Hg_i, and MeHg comprises only a small fraction of Hg_T. No difference was observed between concentrations in resident clams collected in the spring and fall, likely because once Hg is assimilated, loss rates are low. The concentrations of Hg_T in resident clams in EFPC were comparable to clams that were deployed at these same sites for 4 weeks in the spring, suggesting that rather than being a threshold concentration for these organisms, Hg concentrations are coming to an equilibrium between aqueous phase and biological tissue.

The clams collected in EFPC are significantly smaller in size (mean wet weight ~2 g) than those collected at reference locations (mean wet weight ~4 g), suggesting either that the age structure of the population in EFPC is significantly different than in reference sites or that the population is stunted.

One of the key tasks for the project will be to determine how many mussels would be required to make a significant difference in aqueous Hg concentrations. The first step to determining this is to quantify uptake, loss, and FRs of different species under different environmental conditions. Then, the estimated filtration capacity of Asian clams currently populating the creek can be used to make decisions going forward.

Quantifying FRs

The non-native Asian clam is currently the only bivalve species living in EFPC. To assess filtration capacity and quantity of bivalves, including native species, to remediate Hg in the creek, a series of experiments was performed in the laboratory to assess the effects of biotic and abiotic factors on the FRs of native mussels species (*Lampsilis ovata* and *Utterbackia imbecillis*) and Asian clams.

Asian clams were collected from Sewee Creek in Meigs County. Paper pondshell mussels (*U. imbecillis)* were collected by TWRA personnel from Sumner Sportsman Club Lake in Portland, Tennessee (36.604280, −86.487226). Pocketbook mussels (*L. ovata*) were cultured in TWRA's Cumberland River Aquatic Center.

Bivalves were brought to the laboratory in a cooler with an air bubbler. No mortality was recorded during transportation. The bivalves were kept in 700 or 450 L tanks supplied with flow-through water from First Creek (FC) on the Oak Ridge Reservation (water renewal: 50–150 L h^{-1}; ambient temperature: 14°C–28°C; light/dark: 12 h/12 h) and acclimated to the laboratory for at least four weeks prior to the experiment. In addition to the supply of food particles coming from the water inlet (i.e., ~1,000 particles mL^{-1}), bivalves were fed a daily diet of fresh algae: *Chlamydomonas reinhardtii* and *Navicula* sp. (~7×10^7 cells ind^{-1} d^{-1}) using a peristatic pump or medical IV drip bags for continuous feeding.

Effects of light, food, and temperature on the filtration of freshwater bivalves: Asian clams and paper pondshell mussels

In 2020, the influence of various abiotic and biotic factors on FRs of the Asian clam and the poorly studied native species paper pondshell mussels and pocketbook mussels were studied. Filtration activity was assessed through the determination of clearance rates of the studied species (i.e., volume of water cleared of suspended particles per unit of time).

Overall, these studies found that the invasive Asian clams filtered significantly faster in the dark compared with the native paper pondshell mussels, and the FR of the two species did not differ significantly in the light (Hills et al. 2020). Furthermore, the effects of light, food, and temperature on Asian clams and pocketbook mussels were studied, and the relative contribution of the tested variables was species-dependent (Pouil et al. 2021a). Temperature had the largest effect on clearance rate of Asian clams, and food had the most significant effect on the clearance rate of pocketbook mussels. Interestingly, temperature had virtually no effect on pocketbook mussels, and food had no effect on Asian clam clearance rates.

Relationship between size and FR of Asian clams

Many physiological processes scale with the size of the organism, a feature known as allometric scaling. The FR of Asian clams may be such a process, as has been observed in other bivalve species. This is important to quantify to predict the filtration capacity of bivalves in EFPC. To quantify this effect, we measured the FR of various sizes of Asian clams ranging from 0.5 to 4.5 g whole-body weight fed two phytoplankton species of different sizes and biovolumes (*C. reinhardtii* and *Pseudokirchneriella subcapitata*) as food.

Asian clams were collected and held in the lab in the manner described above. We used two species of algae of differing cell size to assess FRs in Asian clams, *C. reinhardtii* (5–6 µm in equivalent spherical diameter and average of 78 μm^3 in volume equivalent spherical diameter) and *P. subcapitata* (e.g., *Raphidocelis subcapitata*; average: 4–5 µm and average of 56 μm^3 in volume equivalent spherical diameter). Previous work has shown that phytoplankton cell size may affect the FR of bivalves. Bivalves were fed algae at a concentration of 100,000 cells/mL. Prior to the experiment, individual Asian clams (*n* = 100, 0.36–4.83 g wet wt, 8.7–20.8 mm shell length) were carefully dried of excess moisture and weighed using a microbalance and shell length and width were measured using a digital caliper. Each individual was randomly selected and placed in a food-grade polyethylene terephthalate container filled with 200 mL of 75 µm–filtered stream water with air bubbling to keep the water well circulated. Clams were acclimated to experimental containers for 4 h prior to the experiment. Depending on its weight, each clam was assigned to an experimental treatment (i.e., one of two algal species used) to get a comparable size range between the two species of algae used (*n* = 50 clams per treatment). At the start of the experiment, concentrated live algae cells were pipetted into each polyethylene terephthalate container filled with filtered stream water to add the targeted initial concentration. The initial cell concentration was immediately verified by analyzing 4 mL samples from each of the three control containers using flow imaging cytometry. A 4 mL sample was taken from each plastic container 10 min after the algae addition, and a second 4 mL sample was taken at the end of the 40 min filtration period. Samples were placed in 5 mL centrifuge tubes containing 800 µL of 10% formalin solution, a common preservative for phytoplankton samples, and were mixed immediately.

The FR experiment was performed using an initial algal cell concentration of 100,000 cells mL^{-1} using two phytoplankton species (*C. reinhardtii* and *P. subcapitata*). Combining the two species, and across all sizes of Asian clams, FRs for Asian clams (*n* = 17–30) ranged from 0 to 347 mL g^{-1} h^{-1} (median value: 52 mL g^{-1} h^{-1}), or 0 to 478 mL ind^{-1} h^{-1}. Although the highest FR values were observed in clams that fed on *P. subcapitata*, no statistical difference in FR was found between the two experimental food types across all clam sizes (Figure 29A), and the proportion of non-filtering individuals during this experiment remained similar for clams that fed on *P. subcapitata* (53%) and *C. reinhardtii* (60%) (Figure 29B).

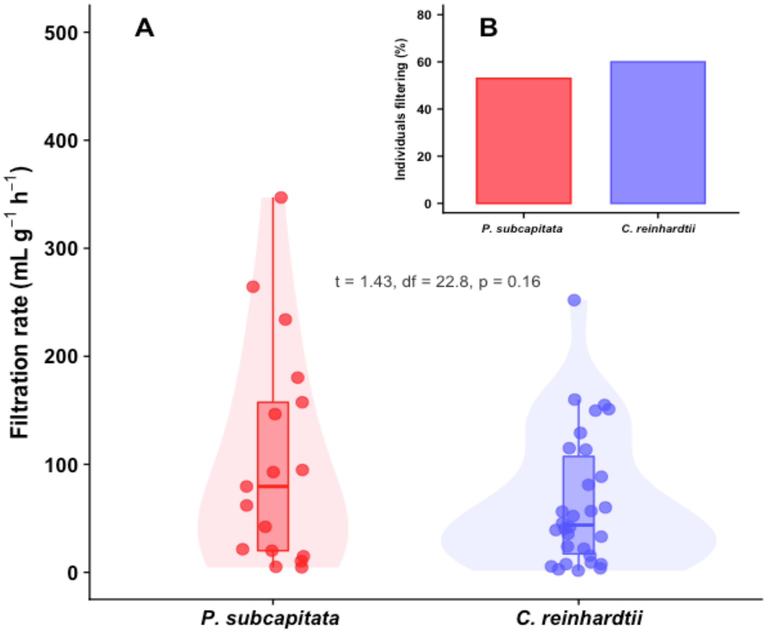

Figure 29. (A) FRs (mL g fresh weight^{-1} h^{-1}) of Asian clams (*n* = 17–30) fed on two phytoplankton species (*C. reinhardtii* and *P. subcapitata*), and (B) percentage of individuals filtering during the experiment for the two food conditions.

FRs for both phytoplankton species were inversely related to clam shell size, soft body weight, and whole-body fresh weight in Asian clams, indicating that smaller (younger) individuals had higher FRs than larger (older) individuals in the tested particle size range (i.e., 4–6 µm diameter equivalent to spherical diameter; Figure 30). When significant, these allometric relationships were described by a power function:

$$\mathrm{FR} = a \times \mathrm{WW}^{b} \text{ (wet weight, g) and } \mathrm{FR} = a \times \mathrm{SL}^{b} \text{ (shell length, mm)} \tag{4}$$

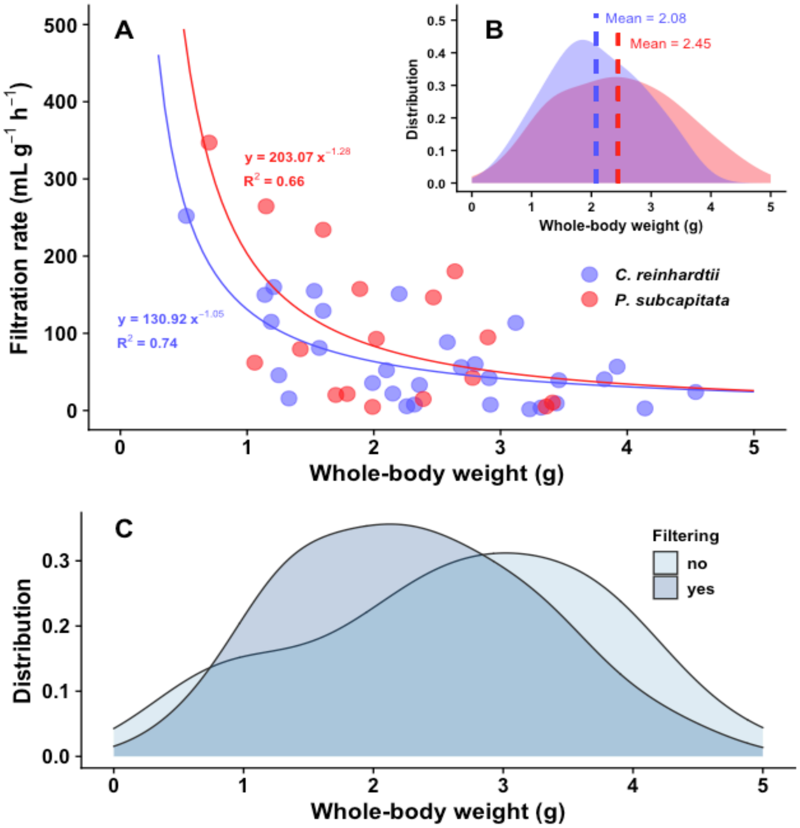

Figure 30. (A) Relationships between FR and whole-body wet weight (g) in Asian clams that fed on two phytoplankton species (*C. reinhardtii* and *P. subcapitata*), and (B) distribution in size for each food condition and (C) among the non-filtering and filtering individuals.

Allometric relationships in FRs of Asian clams that fed on the two phytoplankton species were not significantly different (i.e., $a = 130.92 \pm 13.02$ and $b = -1.05 \pm 0.16$ for *C. reinhardtii*, and $a = 203.07 \pm 32.71$ and $b = -1.28 \pm 0.35$ for *P. subcapitata*; Figure 30A and B), although the size of the individual algal cells varied by 150% in volume (*C. reinhardtii* is larger). Thus, although the average FRs did not change with the two algal species used, at a concentration of 100,000 cells mL^{-1}, the average volume of ingested cells in 40 min was 1.1 µL per individual for clam fed on *C. reinhardtii*, and this value reached 0.7 µL per individual in clams that fed on *P. subcapitata*. These volumes suggest that the clams feeding on the larger cells may get more carbon and other nutrients. Some studies performed on other species have shown that small differences in particle size may strongly affect their selection and retention by the bivalve and thus affect the determination of FR. In the present study, the absence of difference in FRs, as well as the absence of pseudo-feces in Asian clams using the two phytoplankton species, suggests that the size and volume of the particles were indifferently selected both by juvenile and adult clams.

Some of the Asian clams did not filter during the experiment; this non-filtering behavior may be related to the size of the clams. A slightly different distribution of sizes was found between filtering and non-filtering individuals in which larger individuals were more likely to be non-filtering (Figure 30C). Other studies have found that larger (older) organisms can maintain lower metabolic rates by closing their valves for hours, and the results corroborate the findings with higher proportions of larger individuals non-filtering (Figure 30C).

This study highlights the importance of considering the effects of size on FR in Asian clams to better understand the effects of this species on freshwater ecosystems, and in particular the flow of nutrients generated by filtration activity. Asian clams' ability to filter faster as a small individual may be part of the species' suite of r-selected species traits that enable it to successfully invade novel habitats by allowing faster colonization and population establishment. The species has higher filtration and assimilation rates than other freshwater bivalve species, which adapt it for life in unstable environments. Non-native Asian clams can be less sensitive to contaminants than native bivalve species—as shown, for example, for Hg—and thus maintain populations in EFPC where other bivalve species are not present. Through the continuous filtration of water and their benthic lifestyle in relation to the sediment, Asian clams can strongly accumulate certain compounds, including contaminants. These findings also help to refine the potential use of this species in biomonitoring and/or bioremediation programs for contamination.

2.3.3 Mercury Toxicity in Aquatic Invertebrates

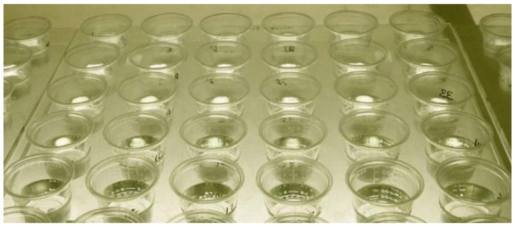

Figure 31. Mercury toxicity test (example) with water fleas for preliminary baseline data for future mussel work.

The described experiments provided data on Hg uptake and loss in Asian clams, as well as FRs. The next steps will be to gather similar data on freshwater mussels. Some FR data on some species of native mussels is available, they have not been exposed to Hg yet. This is a key part of estimating the number of mussels needed to naturally remediate some Hg from EFPC. Therefore, toxicity tests were performed to assess the effects of Hg on a model aquatic invertebrate, the water flea (*Ceriodaphnia dubia*), and the potential for $SnCl_2$ to remove Hg without causing toxicity. In this species, the effects of Hg on survival, reproduction, and growth with and without $SnCl_2$ were examined (Figure 31). Such data are useful to provide a baseline of Hg sensitivity to invertebrates and assess the effects of mitigation strategies, such as the use of $SnCl_2$ (Mathews et al. 2015).

This study consisted of two chronic toxicity tests. In Experiment 1, the toxicity of different concentrations of Hg (500, 500, 10,000, 17,500, and 25,000 ng L^{-1}), along with a control of DMW (diluted mineral water) synthetic freshwater media. In Experiment 2, water fleas were exposed to nine different treatments. The first two treatments tested the toxicity of Hg concentrations at the IC_{25} concentrations (inhibitory concentration at which there is a 25% reduction compared with the control) for Hg for survival and reproduction determined in Experiment 1. Two treatments contained the same IC_{25} Hg concentrations spiked with $SnCl_2$ at a Sn:Hg stoichiometric ratio of 5:1 and bubbled for 16 h (i.e., 4,440 and 10,545 ng Sn L^{-1}, respectively). Toxicity of Sn alone was assessed in two treatments prepared with the same Sn concentrations used for Hg stripping. A control treatment with DMW (no Hg or Sn amendments) was used. In addition, to assess environmental relevance of the results from artificial media (i.e., DMW-based), two treatments were prepared using water from FC, an uncontaminated stream on the Oak Ridge Reservation. FC water was filtered (75 µm) before use to avoid introduction of water flea predators. The first of these natural water-based media was kept Hg-free, and the second was spiked with Hg at a nominal concentration of 5,000 ng L^{-1}, a concentration that was shown in Experiment 1 to affect survival and reproduction in water fleas. The tests were carried out according to EPA guidelines. Briefly, 15 neonates from laboratory cultures born in the same 8 h period the day before the experiment were used per condition. Each neonate was transferred in a 20 mL borosilicate vial filled with DMW media with the appropriate concentrations of Hg. All the neonates were kept in an incubator set at 25°C with 16 h of light per day (10–20 µmol m^{-2} s^{-1}).

Every day during the 7 day experiment, media for the different conditions were prepared and Hg concentrations were checked by cold vapor-atomic absorption. The treatment water was then changed in all of the experimental vials, and neonates were transferred into the freshly prepared vials and fed with 3×10^6 cells ind^{-1} of *P. subcapitata* (e.g., *R. subcapitata*) and 100 µL of yeast. Survival and reproduction were followed every day during the transfer of each daphnid. Water quality (pH, conductivity, O_2) of the DMW media was checked every day before and after exposure.

Growth, estimated by measuring the length of the water fleas from the top of the eye to the base of the spine, was checked every 2 days during the experiment using a stereomicroscope (Leica M80), which was calibrated using a 200 µm stage micrometer.

The intrinsic rate of increase (*r*) of a daphnid population exposed to each treatment was measured using the Euler equation:

$$1 = \sum_{x=0}^{k} e^{-rx} l(x) b(x) \qquad (5)$$

where *l(x)* represents survival from birth to age *x*, and *b(x)* represents the average number of neonates born per day to a female of age *x* (also called the *fecundity schedule*); both are calculated daily from the start ($x = 0$) until the end of the experiment ($x = k$). The Euler equation was numerically solved to find the value of *r* for the entire data set using the “uniroot” function in R Statistical Software (Ver 4.0.1). The data were resampled with replacement 1,000 times using a bootstrapping technique, and values for *r* were recalculated based on resampled data sets to estimate the uncertainty around these values.

In Experiment 1, which tested the effects of Hg alone on water fleas, survival, reproduction, and growth were all significantly affected, especially at the highest Hg concentrations. Survival gradually decreased with increasing Hg concentrations such that no individuals survived at the end of the test at Hg concentrations ≥17,500 ng L^{-1} (Figure 32A). The IC_{25} was determined as 2,109 ng Hg L^{-1} for survival. Reproduction rate was also strongly dependent on the Hg concentrations with a clear decrease in the number of neonates produced by a surviving female per day in water fleas exposed to Hg concentrations ≤500 ng L^{-1} (Figure 32B). Average reproduction rate was reduced by 70% at 5,000 ng Hg L^{-1} compared with the control, and no reproduction was observed at Hg concentrations ≥17,500 ng L^{-1}. The IC_{25} was determined as 888 ng Hg L^{-1} for reproduction. Finally, growth was also significantly affected by Hg. Growth kinetics have been best fitted using linear models (R^2: 0.94–0.96), and a significant difference in slopes was found when water fleas were exposed to 5,000 ng L^{-1} with a significant reduction of the length at the end of the experiment (0.94 ± 0.05 mm against 1.12 ± 0.04 mm for the control and 500 ng Hg L^{-1} treatments) (Figure 33).

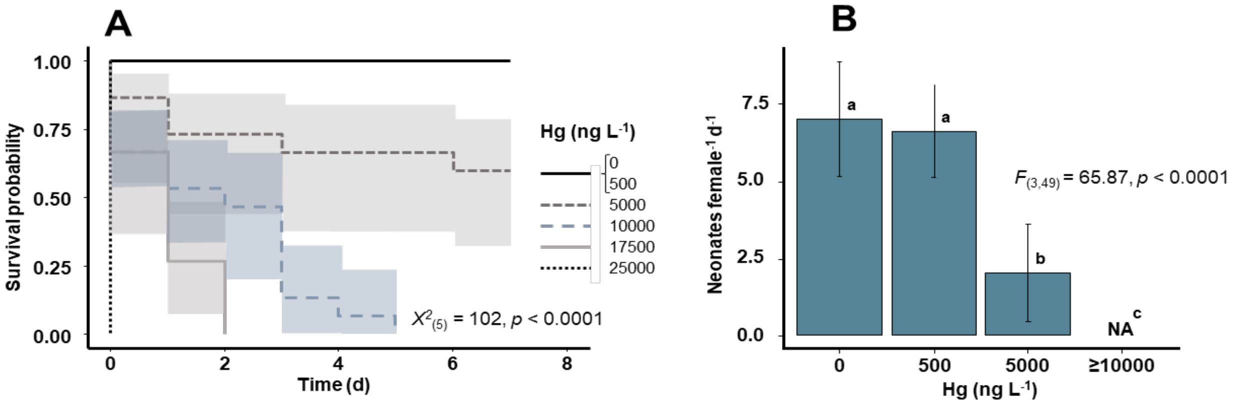

Figure 32. (A) Survival kinetics and (B) reproduction rates (expressed as the number of neonates female^{-1} d^{-1}, means ± standard deviation; see Section 2.5 for details) of water fleas (*n* = 10–15 per condition) exposed for 7 days to DMW media containing a gradient of Hg concentrations. Letters denote significant differences.

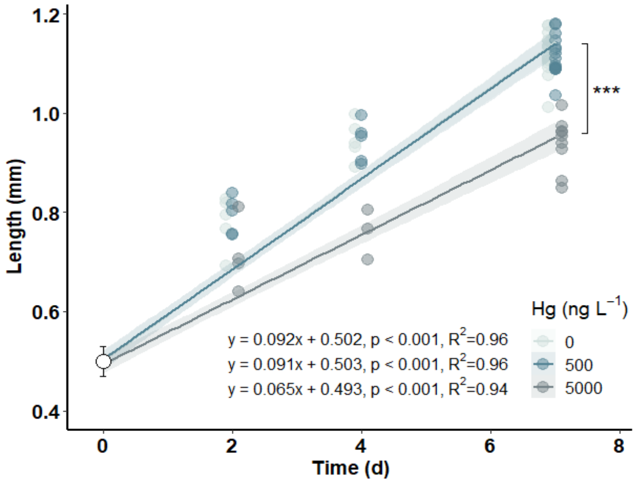

Figure 33. Length (from the top of the eye to the base of the spine) of *Ceriodaphnia dubia* exposed to a gradient of Hg_D concentrations.

The effect of Hg exposure on survival and reproduction also manifested to predicted effects at the population level, as estimated by the calculation of the long-term population growth rate (*r*) of water fleas exposed to these treatments (Figure 34A). Populations with $r > 0$ are predicted to grow exponentially, whereas populations for which *r* values cannot be calculated (due to lack or reproduction or survival) or $r < 0$ are predicted to decline to extinction. Concentrations higher than 10000 ng Hg L^{-1} are predicted to cause extinction of populations of *C. dubia* (Figure 34A). Concentrations as low as 5,000 ng Hg L^{-1} significantly decrease the long-term population growth rate compared with the control and also dramatically increase the variability in these estimates (shown as the larger error bars in Figure 34A).

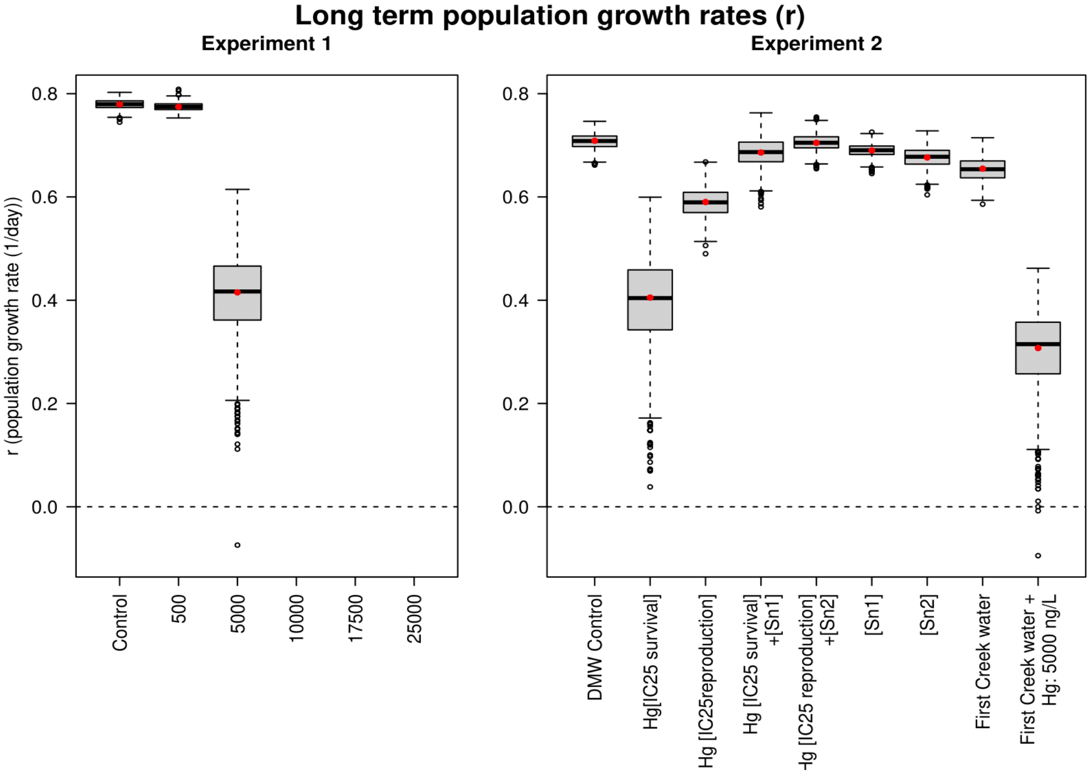

Figure 34. Long-term population growth rates (*r* values) for *C. dubia* exposed to experimental media containing $SnCl_2$ (Experiment 1, left panel) and/or Hg based on DMW or FC water (Experiment 2, right panel). Population growth rates cannot be calculated for treatments in which no individuals survived or reproduced (e.g., Hg concentrations above 10,000 ng L^{-1}), but these populations are predicted to decline to extinction, similar to those with negative *r* values. The box plots represent the distribution of 1,000 iterations of bootstrapped *r* values with replacement (see text for methods description) and the red dots represent the r value of the data set.

In Experiment 2, the effects of $SnCl_2$ treatment on Hg bioaccumulation and toxicity in *C. dubia* were evaluated, as well as the potential toxic effects of the added Sn on *C. dubia*. The results confirmed the efficiency of Hg removal from aqueous samples by $SnCl_2$ and air stripping, with 100% of the Hg removed at both Hg concentrations examined. These results were reflected in the biological endpoints observed in *C. dubia*.

When exposed to a nominal concentration of 2,109 ng Hg L^{-1} in Experiment 2, *C. dubia* survival was reduced by 30% compared with the control treatment, validating the IC_{25} value calculated in Experiment 1. In media with the same nominal Hg concentration treated with $SnCl_2$ at a Sn:Hg stoichiometric ratio of 5:1 (Sn1), no mortality was observed (Figure 35A). The same observation was made in *C. dubia* exposed to Sn alone at the same concentration. In the Sn2 treatment, one adult was found dead, tangled in its molt, on the last day of the experiment.

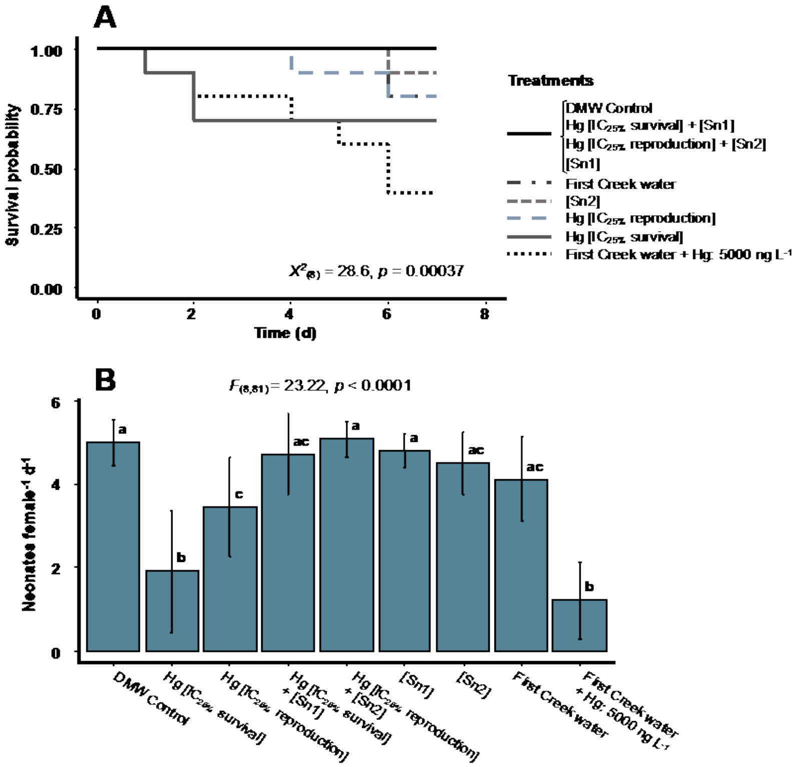

Figure 35. (A) Survival kinetics and (B) reproduction rates (expressed as the number of neonates female^{-1} d^{-1}, means ± standard deviation; see Section 2.5 for details) of *Ceriodaphnia dubia* (*n* = 10 per condition) exposed for 7 days to experimental media containing $SnCl_2$ and/or Hg based on DMW or FC water. Letters denote significant differences.

In Experiment 2, similar to results seen for survival, when exposed to the calculated IC_{25} for reproduction from Experiment 1 (i.e., 888 ng L^{-1}), a 30% decrease in reproduction rate was observed, validating the IC_{25} values for reproduction estimated in Experiment 1 (Figure 35B). Also similar to results seen for survival, *C. dubia* exposed to the same Hg concentrations treated with $SnCl_2$ had a reproduction rate similar to the control treatment. Exposure to $SnCl_2$ alone did not affect the reproduction rate in either of the tested Sn concentrations (Figure35B).

C. dubia growth was not affected by $SnCl_2$, with similar total length measurements observed among the $SnCl_2$-treated Hg, $SnCl_2$, and control treatments at the end of Experiment 2 (i.e., 1.03 ± 0.03 for all the Sn-containing media and 1.05 ± 0.01 mm for the DMW control; Figure 36).

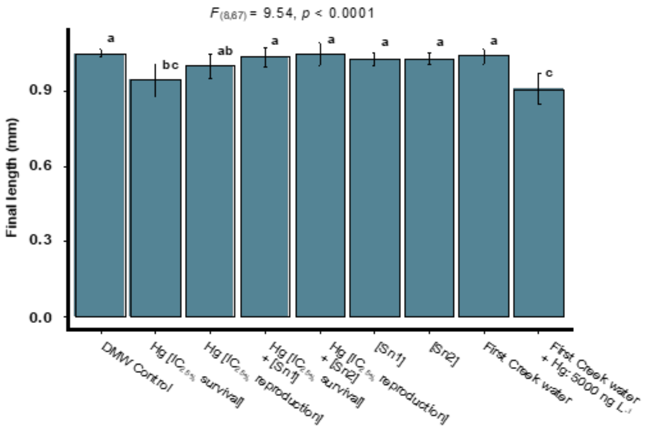

Figure 36. Final length of *Ceriodaphnia dubia* (*n* = 4–10 per condition) exposed for 7 days to experimental media containing $SnCl_2$ and/or Hg based on DMW or FC water. Letters denote significant differences.

C. dubia exposed to media in which Hg was stripped out of solution using $SnCl_2$ had predicted population growth rates similar to controls (Figure 34B). At initial concentrations of Hg that otherwise have a large effect on *r* values (through decreased predicted population growth and increased variability in population growth), treatment with $SnCl_2$ removed this threat from predicted population-level effects. Furthermore, $SnCl_2$ itself is not predicted to have a large effect on populations of *C. dubia*.

Standard toxicity tests often use artificial freshwater media, so Hg speciation and therefore toxicity may be significantly different in natural waters. Similar effects were observed on *C. dubia* survival when exposed to 5,000 ng L^{-1} Hg in DMW and FC water with respective decreases of 60% and 50% of survival compared with the control media (i.e., Hg-free DMW and FC; Figure 35A). Similar results were observed on *C. dubia* growth, with decreases of 16% and 13% when exposed to the same concentrations of Hg in DMW and FC water compared with the respective control treatments (Figure 36). Effects of Hg on reproduction rate were greater in FC than in DMW with decreases of 72% in FC versus 53% for DMW relative to the controls (Figure 35B). The calculated *r* values also indicate that our lab experiments may be relevant for estimation of the ecological risk of Hg in natural systems (Figure 34). First, the DMW control *r* values ($r = 0.78$ and 0.71 day^{-1} from Experiments 1 and 2, respectively) are slightly higher but very similar to the value found for *C. dubia* in FC ($r = 0.65$ day^{-1}; Figure 34). Furthermore, the *r* values are similar in *C. dubia* exposed to 5,000 ng Hg L^{-1} in DMW and FC ($r = 0.42$ and 0.31 day^{-1}), but again, there is a greater negative response in FC compared with DMW, but this may be caused by experimental differences (Figure 34). *C. dubia* in general had lower *r* values for comparable treatments in Experiment 2 compared with Experiment 1, which could indicate some subtle difference in the individuals in the different experiments. This could explain the decreased *r* value for *C. dubia* exposed to 5,000 ng Hg L^{-1} in FC in Experiment 2 compared with the *r* value for *C. dubia* exposed to 5,000 ng Hg L^{-1} in DMW in Experiment 1. Overall, these data support the comparison between the predicted effects of Hg in artificial medium (DMW) and stream water (FC water) on *C. dubia* populations.

A $SnCl_2$ treatment was experimentally used to remove Hg from DMW media, and this remediation method was tested to determine whether it also removes Hg toxicity to a model freshwater invertebrate. Previous field pilot studies have demonstrated the efficiency of $SnCl_2$ for Hg stripping from water. In the present study, $SnCl_2$ used at a Sn:Hg stoichiometric ratio of 5:1 and coupled with air bubbling air was effective for Hg stripping with 100% of Hg removed after a 16 h treatment regardless of the initial concentrations of Hg used (i.e., 888 and 2019 ng L^{-1}). Although $SnCl_2$ appeared to be effective in reducing concentrations of toxic heavy metals in field trials, the effects of the added Sn to aquatic ecosystems had not been previously evaluated. The present study demonstrates the absence of toxicological effects of Sn at concentrations of 2.1 ± 0.4 and 10.9 ± 0.6 µg L^{-1} in the model invertebrate, *C. dubia*. As a comparison, Mathews et al. (2015) found that a pilot $SnCl_2$-based treatment system increased aqueous Sn concentrations from <0.5 to ~12 µg L^{-1} in a treated stream. In addition to the absence of toxicological effects of Sn on growth, survival, and reproduction, Hg stripping using $SnCl_2$ allowed a full recovery of the three investigated endpoints, including predicted population-level effects. The effectiveness of $SnCl_2$-based remediation of Hg has already been demonstrated in the field, but the toxicological risks of this remediation treatment were previously unknown.

2.3.4 Mercury Biokinetics in EFPC Fish

The primary goal of the ecological manipulation task is to reduce Hg bioaccumulation in fish in EFPC. In 2020, a biokinetic model was examined to estimate Hg in fish, incorporating many dynamic natural factors; a progress update is provided in this report. The biokinetic model, known in the literature as the DYMBAM model (e.g., Luoma and Rainbow 2005), predicts the concentration of a contaminant (here, Hg) within an organism (C_t) based on two modes of influx and two of efflux. The internal concentration of Hg (C_t) increases from aqueous exposure (I_W) and through ingestion of contaminated food (I_F). The internal Hg concentration decreases because of the rate of efflux (the organism excreting Hg in some way at a rate k_e) and growth (at a rate g). The latter is referred to as *dilution due to growth*—as the organism grows, the contaminant is diluted because of an increase in biomass (the denominator of the internal concentration, C_t). The equations are defined below with parameters listed in Table 5.

$$\frac{dC_t}{dt} = (I_W + I_F) - (k_e + g)C_t \tag{6}$$

$$I_W = k_u C_w \tag{7}$$

$$I_F = AE \times IR \times C_F \tag{8}$$

Table 5. Parameters of Biokinetic model.

Parameter	Description	Source of value
k_u (L/(g_{fish} × d))	Uptake rate of Hg into from water	Literature
k_e (1/d)	Efflux rate of Hg from fish into water	Literature
g (1/d)	Growth rate	Estimated from mark recapture data
C_w (mg_{Hg}/L)	Hg concentration in water	EFPC data
C_F (mg_{Hg}/g_{food})	Hg concentration in food	EFPC data
AE	Assimilation efficiency	Literature
IR (g_{food}/(g_{fish} × d))	Ingestion rate	Literature

The data for this model include Hg concentrations from EFPC fish (redbreast sunfish and rock bass) collected by the team from 2008 to 2019. EFPC data includes many fish that have been PIT (passive induced transponder)-tagged and recaptured to compare Hg levels in recaptured and one-time measurement data. It also incorporates data from an extensive literature search to identify parameter values for the model (Table 6).

Table 6. Brief summary table of literature review of Hg biokinetic studies in multiple species of fish.

Form of Hg	Dietary parameter	Freshwater	Marine
Hg	*AE* (%)	8.5–51.3	10.4–38
	k_e (d^{-1})	0.003–0.042	0.026–0.104
	k_u (ml g^{-1} d^{-1})	38–78	5–305
^{203}Hg	*AE* (%)	13.2–35	1.9–43
	k_e (d^{-1})	0.039–10.5	0.071–0.131
	k_u (ml g^{-1} d^{-1})	86	15–80
	half life (days)	18	
MeHg	*AE* (%)	32–98	55.6–95.4
	k_e (d^{-1})	0.0042–0.021	0.0018–0.024
	k_u (ml g^{-1} d^{-1})	185–1,280	350–1,900
^{203}MeHg	*AE* (%)	50–95.4	10–99
	k_e (d^{-1})	0.0055	0.004–0.02
	k_u (ml g^{-1} d^{-1})	333	1,155–4,375

To parameterize this model, weekly water concentration data of Hg from Station 17 (EFK 23.4) were collected and correlated to the seasonal water data collected at the four EFK sites at which data were collected on Hg concentrations in fish (EFKs 24.4, 18.2, 13.8, and 6.3). Using these data sets, weekly concentrations of Hg in water at all four EFK sites were estimated. To estimate the concentration of Hg in what the fish are eating, FishBase (a global database of fish species) was used to identify the diet composition of rock bass and redbreast sunfish in EFPC. Data from the 2015 survey of Hg and MeHg concentrations in prey items in EFPC were used to calculate bioconcentration factors based on the water concentrations of Hg measured at the site at which each prey item was collected on the closest sampling date (water and prey sampling dates differed by a maximum of 4 days). The bioconcentration factors quantify the amount of Hg taken up from the water into the prey organism per unit biomass. Once these bioconcentration factors were calculated, the concentration of Hg in all potential prey items was estimated through time using the concentration of Hg present in the water. The reconstructed water and diet concentrations of Hg in redbreast and rock bass sunfish are shown in Figure 37.

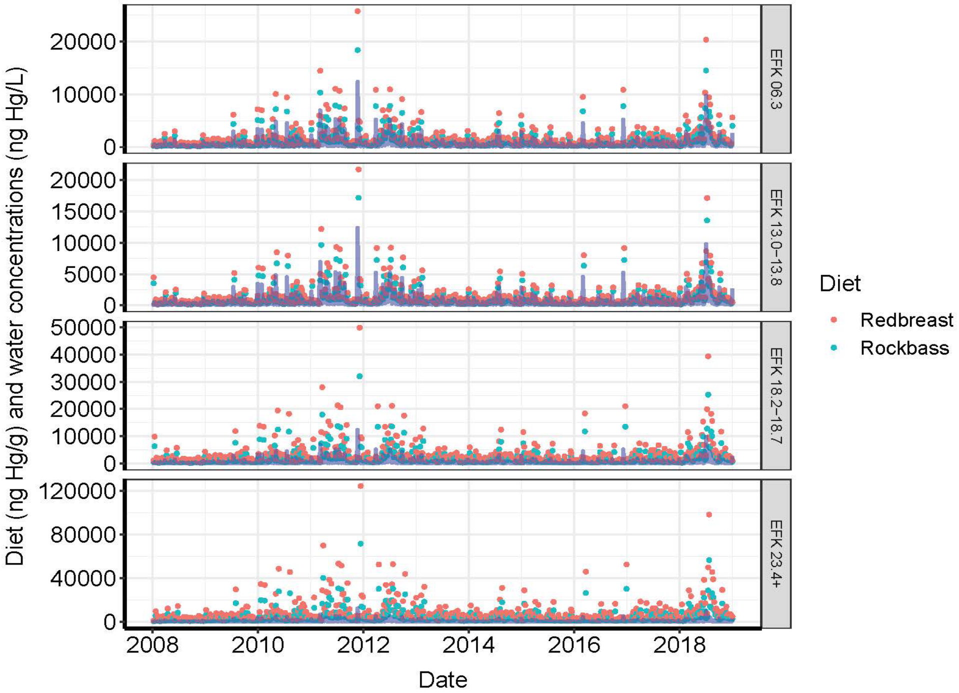

Figure 37. Reconstructed water (blue lines) and diet (pink and green points) concentrations of Hg for sunfish in EFPC from 2008 to 2019. These concentrations are used in a biokinetic model to predict the concentrations of Hg in the sunfish.

These concentrations along with parameter values from the literature and calculated from the data set facilitate the prediction of Hg body burdens of sunfish in EFPC. This work is still in progress, but a preliminary model fit is shown in Figure 38 for redbreast and rock bass in UEFPC.

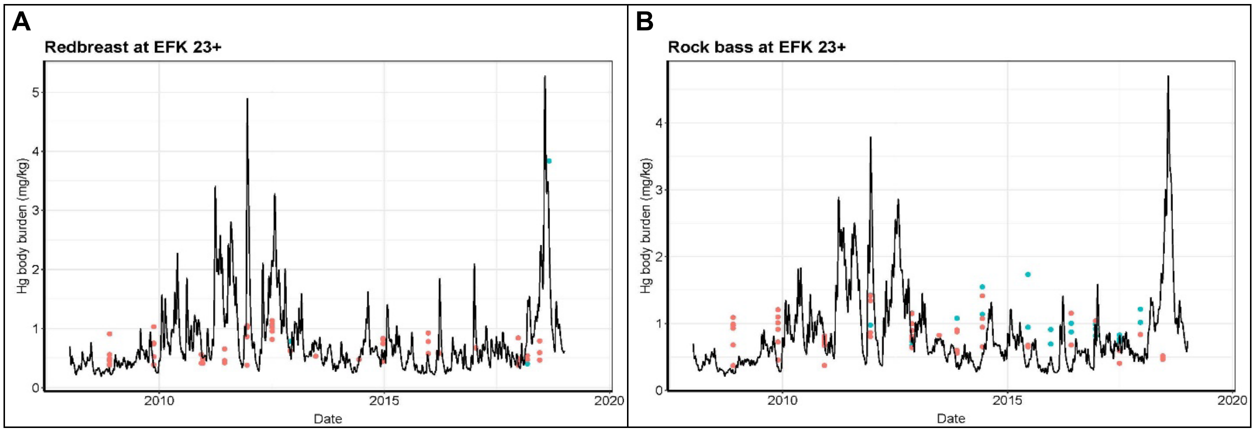

Figure 38. Biokinetic model predictions of (A) redbreast and (B) rock bass sunfish concentrations at UEFPC. Teal points denote fish that were marked and recaptured (used to estimate the growth rate parameter), and red data points denote fish that were not marked and recaptured (data points that were not used for parameterization).

Successful parametrization of this biokinetic model to the data on EFPC would enable the prediction of Hg concentration in fish based on the aqueous and dietary concentrations of Hg in EFPC. Analysis of this model will also allow for a quantitative comparison of the relative impact of Hg aqueous and dietary exposure on the Hg concentration in fish. Additionally, this model is being parameterized separately for MeHg and Hg_T, facilitating the direct comparison of the two forms of Hg on bioaccumulation in fish.

Furthermore, this model could be used in the future to estimate the aqueous and dietary concentrations of Hg in EFPC needed to achieve the desired reduction of Hg contamination in biota necessary to meet the National Recommended Water Quality Criterion. Identifying these target concentrations is crucial to estimate the number of bivalves needed in EFPC to decrease aqueous Hg concentrations to a level that will have a meaningful effect on concentrations of Hg in EFPC fish.

2.3.5 Ecological Manipulation Future Needs

Within this task, several areas of continuing and new research are warranted. Because periphyton serves as the base of the food chain and is likely a large factor contributing to MeHg production and bioaccumulation in EFPC, understanding periphyton dynamics (e.g., standing stock biomass, growth rate) is critical. Data were collected on Hg inventories in periphyton, and methods are being developed to characterize biomass in the stream (see Section 2.4). In the lab, preliminary growth of periphyton from EFPC will begin, which will allow for an investigation of natural species from the creek and to estimate the Hg methylation rate and capacity of current periphyton communities, as well as better understand the interactions among freshwater mussels, FRs, and periphyton density under controlled conditions.

Lab populations of Asian clams and native species are being built up for Hg bioaccumulation and toxicity experiments in fall 2021.

One fundamental need for the ecological manipulation task is to determine the suitability of EFPC as a habitat for native mussels. Currently, only Asian clams are present in the stream, and having very low species diversity (in this case, a single species of mollusks) reduces the capacity and effectiveness of mussels to filter nutrients, bacteria, particulate and dissolved organic matter, and metals from the water column.

Mussels biomagnify Hg in their soft tissue relative to water and sediment concentrations. The rate and capacity of adult mussels to accumulate Hg has not been carefully studied and plays a direct role in determining the population of mussels necessary to significantly affect Hg concentrations in EFPC and thereby reduce the Hg burden in fish tissue. Experiments will aim to determine the relationship between mussel soft tissue and water concentrations of both Hg_i and MeHg. Additionally, the filtration behavior of mussels may reduce the aqueous concentration of nutrients, particulate and dissolved organic matter, and microorganisms. This may reduce the potential for periphyton growth and limit the suitable environments and substrate necessary for the bacteria in the periphyton responsible for Hg methylation.

Further laboratory, field, and modeling work is needed to better understand the factors affecting mussel and clam filtration and Hg removal rates and to determine the implications of mussel filtration on Hg methylation. Although experiments to date have focused on FRs, upcoming experiments will focus on Hg removal and bioaccumulation rates. Critical to this discussion is a modeling exercise to determine the density of mussels needed to achieve Hg removal in the stream and whether the food web in EFPC could support such a density. These studies will rely heavily on the use of the renovated stream mesocosms that were a part of the AEL upgrade. Finally, additional modeling work is needed to evaluate the potential of additions or removals of fish or mussel species to mitigate Hg trophic transfer in the stream.

2.4 PERIPHYTON DYNAMICS AND DISTRIBUTION

2.4.1 Background

Previous research in EFPC suggested that key controls on net MeHg concentration occurred in the stream or on the stream bed, and several lines of evidence pointed to benthic algal biofilms as central agents of MeHg production. Periphyton biofilms (also known as benthic algae) are complex assemblages comprising algae, bacteria, fungi, detritus, extracellular polymers, invertebrates, and mineral particles. Controlled laboratory experiments using field-derived periphyton biofilms and ambient creek water from EFPC have demonstrated that actively photosynthesizing biofilms may generate a significant fraction of the MeHg in EFPC (Olsen et al. 2016, Schwartz et al. 2019). Ancillary measurements showed that over a biofilm depth of less than 2 mm, dissolved oxygen was consumed and both Fe(III) and SO_4^{2-} reduction occurred—conditions that are favorable for Hg methylating bacteria. Genetic analysis of periphyton samples has shown the presence of *hgcA* (one of two required genes for Hg methylation) from each of the three major clades containing Hg methylators (*Deltaproteobacteria*, *Firmicutes*, and *Archaea*). In addition to being a source of MeHg production, these biofilms accumulate significant amounts of MeHg from their surroundings. The largest step in MeHg biomagnification is from water to algae with a biomagnification factor on the order of $10^4\times$ to $10^5\times$; biomagnification factors along the remaining steps of the trophic ladder are on the order of 10×.

Because periphyton biofilms form the base of the aquatic food web, the fact that they are a source of MeHg generation coupled with high biomagnification factors is of central importance to understanding and perhaps controlling MeHg concentrations in fish. Recently, microbial community composition in these biofilms was discovered to potentially be equally or more important in governing MeHg production than the mere presence of Hg methylating organisms (Carrell et al. 2021). Methylation rate for biofilms cultured under different conditions was correlated with many bacteria that do not methylate Hg and was related to the overall community connectedness. Despite these insights, the ability to scale these findings to a whole-creek level is limited by a lack of information on the extent of periphyton coverage on the bed of EFPC and lack of quantitative estimates of the algal representatives in these biofilms.

Traditional methods for the quantification of periphyton distribution and abundance in the field are time-consuming and labor-intensive. Even the most ambitious sampling campaigns will have large spatial gaps, requiring tenuous interpolation and extrapolation methods to fill those gaps but introducing significant uncertainty. Estimates of percent cover require visual identification of general taxonomic or phenotypic groups and rigorous surveying of known areas using transects and sampling grids. Estimates of biomass (generally in terms of chlorophyll *a* content per unit area) require scraping algae from known areas of substrate and quantifying biomass in the laboratory, which limits the ability for high levels of sample replication. High spatial heterogeneity (patchiness) of periphyton requires numerous samples to be collected, even in smaller stream systems, to estimate biomass per unit area. Standard methods for estimating organic and inorganic carbon biomass may require acidification and combustion of samples. Standard methods for estimating algal biomass of these samples require mechanical lysis and chemical extraction of algal pigments (i.e., chlorophyll *a*) prior to spectrophotometric quantification. However, given that these methods are destructive, they do not allow for identification of the taxonomic composition of the sample at any level. Such identification requires additional samples with the depth of the identification limited by the level of the taxonomist's training; genus- and species-level identification often require highly trained algal taxonomists, further increasing the labor and time required.

Recent advances in in situ fluorescence-based techniques provide an opportunity to better estimate the distribution and abundance of periphyton-associated algal biomass in the field (Catherine et al. 2012). Handheld instruments such as the BenthoTorch (bbe-Modaenke, Germany) enable the rapid (10–20 s per measurement) and nondestructive quantification of periphyton chlorophyll biomass. Furthermore, fluorescence properties of diagnostic pigments can be used to discriminate the relative contribution of different taxonomic groups (e.g., photosynthetic cyanobacteria, diatoms, green algae) to the total chlorophyll *a* biomass. Several studies evaluating instrument performance have identified limitations and caveats for its use, including a small sampling area (1 cm^2), underestimation from high chlorophyll *a* biomass samples, poor penetration of thick algal mats, dependence on the photophysiological condition of the algae, and potential underestimation of contributions from green algae and phycoerythrin-containing cyanobacteria (Kahlert and McKie 2014, Harris and Graham 2015, Echenique-Subiabre et al. 2016, Kaylor et al. 2018, Rosero-Lopez et al. 2021). However, this approach has merit, provided it is accompanied by routine comparisons with standardized methods to check for data agreement (Rosero-Lopez et al. 2021).

One approach to address the scaling issue associated with the labor-intensive periphyton field data collection is to use remote sensing approaches in combination with field data collection to map periphyton distribution and abundance. Publicly available satellite imagery such as Landsat are too coarse in spatial resolution to detect smaller streams such as EFPC. Because ORNL is a federally funded institution, the team has access to high-resolution satellite imagery from DigitalGlobe, but these data are still somewhat spatially coarse for small streams. Airborne imagery can offer significant resolution improvements over satellite imagery but can be quite costly to acquire. Near-surface remote sensing via unoccupied aerial systems (UASs) is a cost-effective (Sankey et al. 2017) and flexible alternative for targeted data collections in smaller study areas such as the EFPC watershed. In this new task, methods were developed, and the use of UAS remote sensing techniques combined with field and lab data collection and analysis was explored to further the understanding of periphyton dynamics and distribution in Bear Creek and EFPC. UAS data collection missions of multi/hyperspectral imagery were seasonally conducted, along with a suite of ground data collections, including periphyton fluorescence using the BenthoTorch, physical habitat characteristics, periphyton samples for chlorophyll *a* concentrations and biomass, and samples for various water quality parameters, including Hg and MeHg.

2.4.2 Methods

UAS remote sensing

A novel multimodal imaging payload containing five sensors was used onboard a UAS. A hyperspectral pushbroom sensor, a 5 band multispectral camera, a longwave infrared thermal camera, a lidar scanner, and an RGB camera were mounted onto a Class-1 UAS (Duncan et al. 2019). The heavy lift UAS (Strelka) was designed by the ORNL Unmanned Vehicle Development Laboratory to carry modular payloads (Figure 39). The Strelka UAS has a maximum flight time of 45 min and can carry a maximum payload of 12 lb. The lidar sensor onboard the UAS is a Velodyne Puck LITE, which uses a 903 nm Class 1 laser at 600,000 points s^{-1} in dual return mode. A high-resolution hyperspectral imager, the Resonon Pika L, was the most used sensor onboard the aircraft in this study. The Pika L has 300 spectral bands within the 400–1,000 nm spectral region (Figure 39) (Duncan et al. 2019). Additionally, a FLIR Duo Pro R dual-sensor thermal/RGB and 5 band MicaSense RedEdge-M multispectral sensor were flown. The multispectral sensor has 5 spectral bands in the following regions: blue (465–485 nm), green (550–570 nm), red (663–673 nm), red edge (712–722 nm), and near-infrared (820–860 nm).

Figure 39. Multimodal imaging payload onboard the Strelka UAS; MicaSense RedEdge-M (multispectral), FLIR Duo Pro R (thermal and RGB), Resonon Pika L (hyperspectral), and Velodyne Puck LITE (lidar) (Duncan et al. 2019).

A second platform was also used during this study, the Wingtra One (Figure 40). The Wingtra One is a VTOL (vertical take-off and landing) tail sitter UAS with a maximum flight time of 60 min. The payload flown on the Wingtra was a 5 band MicaSense RedEdge-MX multispectral sensor.

Figure 40. Wingtra One VTOL UAS at EFK 6.3.

For a leaf-off winter data collection, the Wingtra One was flown on March 9, 2021, over Bear Creek kilometer (BCK) 7.0 and EFK 6.3. Ground control points were used to precisely georeference images, and a white reference panel was imaged before and after flight to convert the data to reflectance values during post-processing. The UAS was flown at approximately 370 ft above ground level at both locations, which produced a spatial resolution of 7.83 cm. Pix4D post-processing software was used to generate georeferenced orthomosaics for each spectral band.

On April 15 and August 12, 2021, data collection missions were flown with the Strelka UAS and hyperspectral sensor at 245 ft above ground level, which produced a spatial resolution of 5 cm. A calibrated LabSphere white reference panel was imaged before flight for conversion from radiance to reflectance values. The hyperspectral data cubes were post-processed to reflectance and georectified using SpectrononPro software. Hyperspectral data were collected for EFK 6.3 in both April and August, and for BCK 7.0 in August. At BCK 7.0, two flights were conducted over two portions of the creek. For the August data collection, more than 88 GB of hyperspectral data were collected.

Imagery and geospatial analysis

Analysis of the multispectral and hyperspectral imagery from the UAS platforms was conducted using ENVI 5.6 (L3Harris Geospatial) and ArcGIS Pro 2.8.1 (ESRI). The Seamless Mosaic tool in ENVI was used to create seamless mosaics of the hyperspectral data cubes from April and August, and the Spectral Resampling tool was used to resample the hyperspectral data to match the response of the MicaSense RedEdge-MX. Then, the Raster Calculator in ArcGIS Pro was used to calculate the normalized difference chlorophyll index (NDCI) for all UAS missions from March, April, and August to visualize spatial patterns in aquatic vegetation and compare across seasons. The NDCI was calculated using the band formula: [red edge − (red/red edge) + red]. ArcGIS Pro was used to clip the imagery to the stream corridor, and then the Iso Cluster Unsupervised Classification tool was used to distinguish water from non-water pixels and create water masks for each site and date.

A WorldView-2 multispectral satellite image from March 29, 2016 was downloaded from the DigitalGlobe Global Enhanced GEOINT Delivery web portal to calculate the NDCI and other chlorophyll indices (Buma and Lee 2020) for aquatic vegetation in EFPC at that time. WorldView-2 imagery has a spectral resolution of 8 bands and a spatial resolution of 2 m. The team attempted to fit a model using the different chlorophyll indices as the response variables, and explanatory variables from the 2013 EFPC kayak survey, the December 2015/January 2016 US Geological Survey 3D Elevation Program lidar data, and other layers derived from previous geospatial data integration efforts performed for this project in previous years. Explanatory variables from the kayak survey included substrate type, substrate grain size, depth, and habitat type (i.e., riffle, run, pool). Lidar-derived predictors included numerous direct and diffuse solar radiation metrics for the stream channel, and riparian vegetation density. Other predictors included distance on the EFPC mainstem from the Oak Ridge wastewater treatment facility discharge, and high-resolution land cover data for stream reach subwatersheds and entire upstream watersheds. The Forest-based Classification and Regression machine learning tool in ArcGIS Pro was run to model the different chlorophyll indices.

Field data collection

Habitat assessment

The team used 12 in. square quadrats in the field to establish locations for instream data collection. For the April 15 collection at EFK 6.3, 11 transects were established throughout the surveyed reach, and a quadrat was placed at left, middle, and right channel locations at each transect. The transect locations were selected to capture a variety of instream habitat and tree canopy cover conditions. At each quadrat, nine BenthoTorch readings collected (that were subsequently averaged), along with water depth, substrate type, visual periphyton characterization, and a sub-meter GPS position. On August 12, 2021, quadrats were opportunistically placed in areas with open tree canopy throughout the surveyed reaches at BCK 7.0 and EFK 6.3 to capture more spatially rich data than the transect approach. Data were collected at 50 quadrat locations at BCK 7.0, and 25 locations at EFK 6.3, more than doubling the number of quadrat locations from April. The same suite of parameters was collected as for the April event, except fewer BenthoTorch readings (3–4) were collected to allow for data collection at more locations. For the March 9 collection event, instream data collection was very limited because of time constraints resulting from technical difficulties encountered with the UAS in the morning.

Periphyton collection

At each site, one to two rocks were collected in a plastic container with stream water and transported to the lab on ice. In the laboratory, each rock was scrubbed in the plastic container with a small brush to remove periphyton. An aliquot of the resulting periphyton slurry (typically 10 mL) was filtered through a GCF filter while keeping the sample in the dark. Each filter was placed into a 50 mL polypropylene tube and then placed in a −20°C freezer in the dark until chlorophyll *a* processing occurred. Estimates of the periphyton-covered surface area of each rock were calculated by wrapping the scrubbed portion of each rock in aluminum foil, tracing the outline of the scrubbed portion, and cutting out the shape.

Fluorometric characterization of chlorophyll content in periphyton

Algal biomass and taxonomic composition were assessed at each quadrat in the stream using the BenthoTorch fluorometer (bbe-Moldaeke, Germany). This instrument emits LED light pulses at 470, 525, 610, and 700 nm, records the chlorophyll *a* response, and uses predefined algorithms to identify the relative proportion of the fluorescence signal associated with diatoms, cyanobacteria, and green algae. At the center of each quadrat, the algal assemblages present on a 1 cm^2 area of natural substrate were excited for 10 s, and the fluorescence was measured without any dark adaptation. This was repeated three times within each quadrat to reduce variation. In addition, fluorometric estimates of total chlorophyll *a* were made on varying amounts of freshly scraped periphyton to compare in situ fluorometric estimates with standard extraction-based laboratory methods. Algae were placed on black polyvinyl chloride calibration discs with recessed centers that are included with the benthoTorch to provide a consistent background reflection. A total of 10 samples were measured using the Benthotorch ($n = 3$) and then rinsed into 50 mL polypropylene tubes and stored in the dark until processing in the laboratory.

Water sampling

Bulk 500 mL water samples were collected from mid-stream in new glycol-modified polyethylene terephthalate bottles by triple-rinsing the bottles with creek water prior to sample collection. A separate 1 L sample was collected in an opaque high-density polyethylene bottle for chlorophyll *a* analysis. A separate sample for total suspended solids (TSS) was collected in two 1 L high-density polyethylene bottles. Concurrent with water sampling, ambient water conditions (temperature, specific conductance, pH, dissolved oxygen) were measured using an In-Situ AquaTroll 9500 (In-Situ Inc., Fort Collins, Colorado). Water samples were processed as soon as possible in the field and placed on ice until returning to the lab for storage until analysis. An unfiltered aliquot of each sample was retained for quantification of Hg_T and $MeHg_T$, and the remaining sample was filtered through a 0.2 µm pore size polyethersulfone filter using an analytical filter unit for analysis of Hg_D and $MeHg_D$, DOC, and ultraviolet–visible spectroscopy absorption. Unfiltered and filtered Hg and MeHg samples were preserved to 0.5% (v/v) trace metal-grade HCl in glycol-modified polyethylene terephthalate bottles, and DOC samples were preserved to 0.1% (v/v) trace metal-grade HCl in amber glass bottles. Samples for ultraviolet–visible spectroscopy analysis were kept in amber glass bottles. All samples were stored in the dark at 4°C until analysis.

Samples collected for TSS analysis were filtered in the lab through a tared Whatman glass fiber filter with 0.7 µm particle retention. TSS was determined by drying the filters to constant weight in a 60°C oven, subtracting the filter tare mass, and dividing the resulting mass by the volume of water filtered.

Hg analyses were conducted using a Lumex instrument. Bromine monochloride was added to all Hg samples at a minimum of 24 h before analysis. Stannous chloride was added to the samples, and the Hg(0) produced was purged from solution and measured via cold vapor atomic absorption. Ambient MeHg was analyzed using modifications of US Environmental Protection Agency method 1630, which involves the distillation of the water sample followed by ethylation, purge, and trap onto Tenax traps; gas chromatographic separation of the Hg species; and detection by ICP-MS. This analysis was performed with a Brooks Rand MERX-M instrument coupled with a Perkin Elmer NexION ICP-MS. An internal standard ($Me^{200}Hg$) was added to samples prior to distillation and this isotope was used to quantify MeHg concentrations. Analysis of Hg_T and $MeHg_T$ in periphyton was conducted by nonaqueous phase extraction of the MeHg, back extraction into water, and processing as described earlier for water samples.

DOC concentrations were measured using high-temperature platinum-catalyzed combustion followed by infrared detection of CO_2 (Shimadzu TOC-5000A or Shimadzu TOC-L). Ultraviolet-visible spectra were collected at 1 nm intervals and 0.5 s exposure time from 190 to 1,100 nm wavelengths with an HP 8453 spectrophotometer using a 1 cm path length quartz cuvette.

2.4.3 Results

Imagery and geospatial analysis

Table 7 summarizes the winter (Figure 41), spring (Figure 42), and summer (Figure 43) UAS data collection events.

Table 7. Summary of UAS data collection events.

Site	Date	UAS platform	Spectral sensor	Stream reach length	Spatial resolution
EFK 6.3	March 9, 2021	Wingtra	MicaSense RedEdge-MX	666 m	8 cm
	April 15, 2021	Strelka	Resonon Pika L	275 m	5 cm
	August 12, 2021	Strelka	Resonon Pika L	275 m	5 cm
BCK 7.0	March 9, 2021	Wingtra	MicaSense RedEdge-MX	900 m	8 cm
	August 12, 2021	Strelka	Resonon Pika L	400 m	5 cm

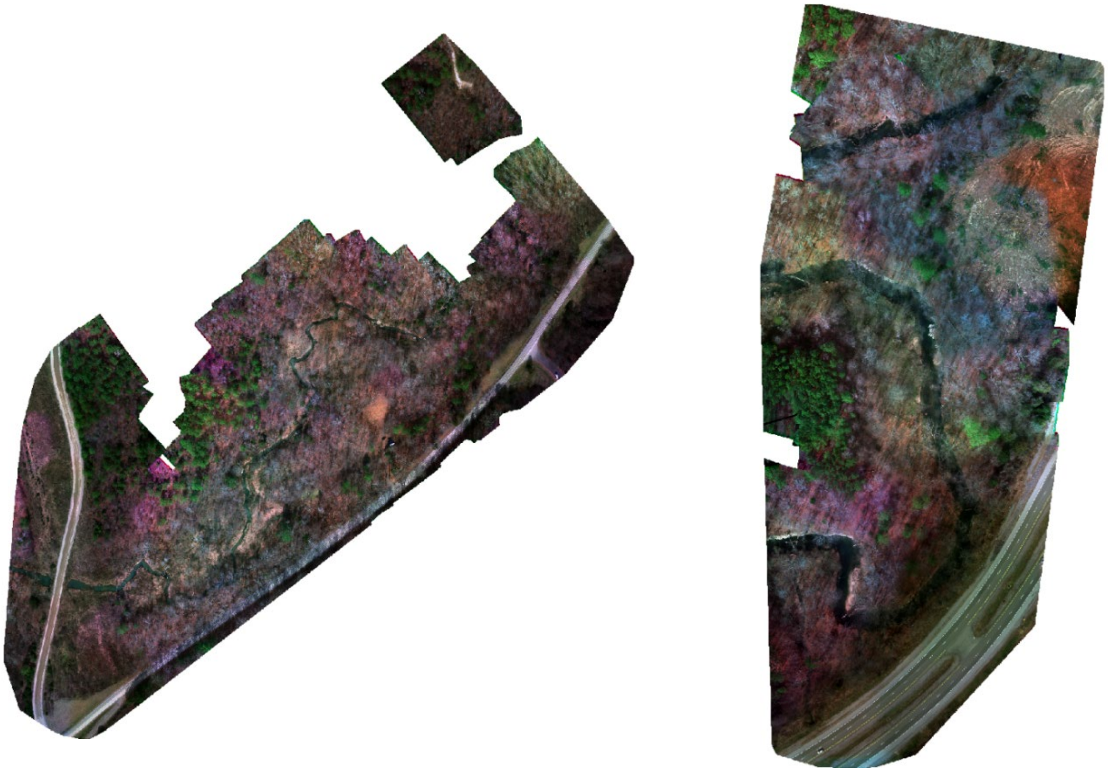

Figure 41. True color images from MicaSense RedEdge-MX for winter (March 9, 2021) collection at (left) BCK 7.0 and (right) EFK 6.3.

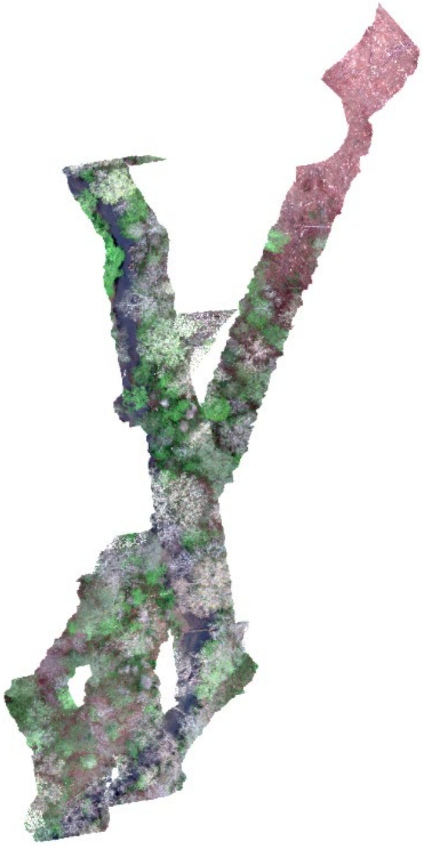

Figure 42. True color image from hyperspectral mosaic for spring (April 15, 2021) collection at EFK 6.3.

Figure 43. True color images from hyperspectral mosaic for summer (August 12, 2021) collection at (A) EFK 6.3, (B) BCK 7.0 flight 1, and (C) BCK 7.0 flight 2.

At EFK 6.3, NDCI values for water pixels appear to be generally similar for the winter and spring collections but significantly higher for the summer collection (Figure 44). At BCK 7.0, NDCI values showed a significant increase from winter to summer (Figure 45). This follows the expected seasonal trend of higher periphyton growth in the summer in areas with open canopy and thus higher sun exposure. Periphyton growth can be limited by light or nutrients, or both, and is influenced by stream temperature. Assuming nutrient levels are relatively constant throughout these short stream reaches, chlorophyll *a* concentrations would be expected to increase with warmer water temperatures and more sun exposure in the summer. As leaf-out occurred from winter to summer, canopy cover obstructed increasingly more of the stream, resulting in less area assessed from winter to summer. However, the high-resolution data

(Figure 46, Figure 47) can show changes in chlorophyll *a* patterns in areas with open canopy at a very fine scale and can be very informative for assessing vegetation patterns in small patches of stream.

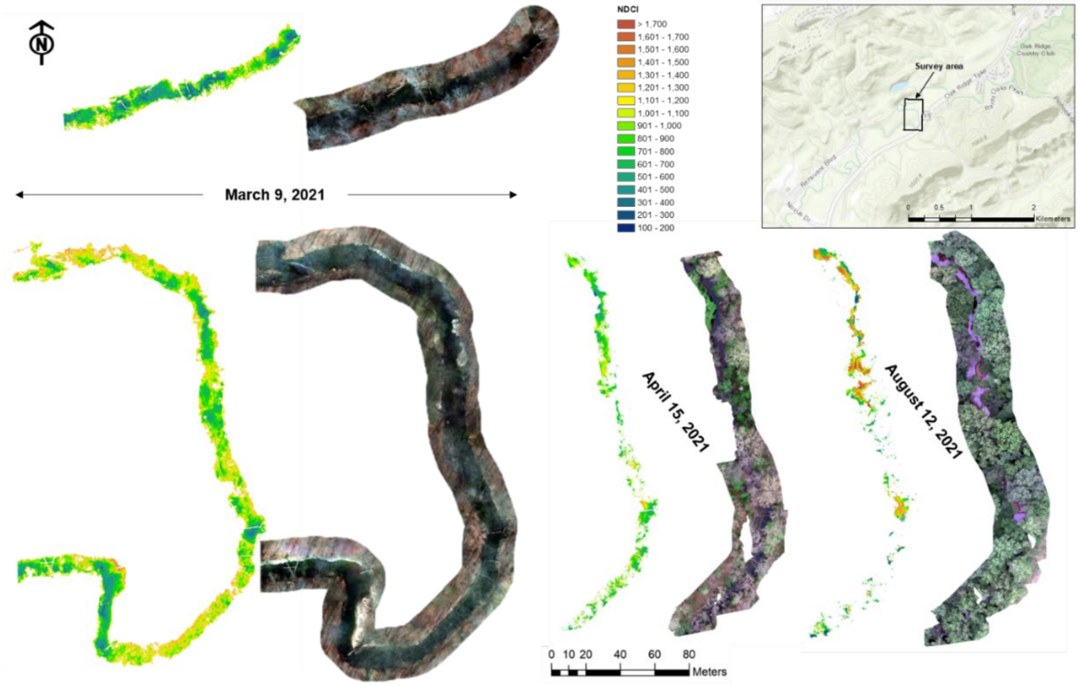

Figure 44. UAS data collected at EFK 6.3 in winter, spring, and summer. NDCI and true color images are shown from left to right for each date. Survey area is shown in the inset map.

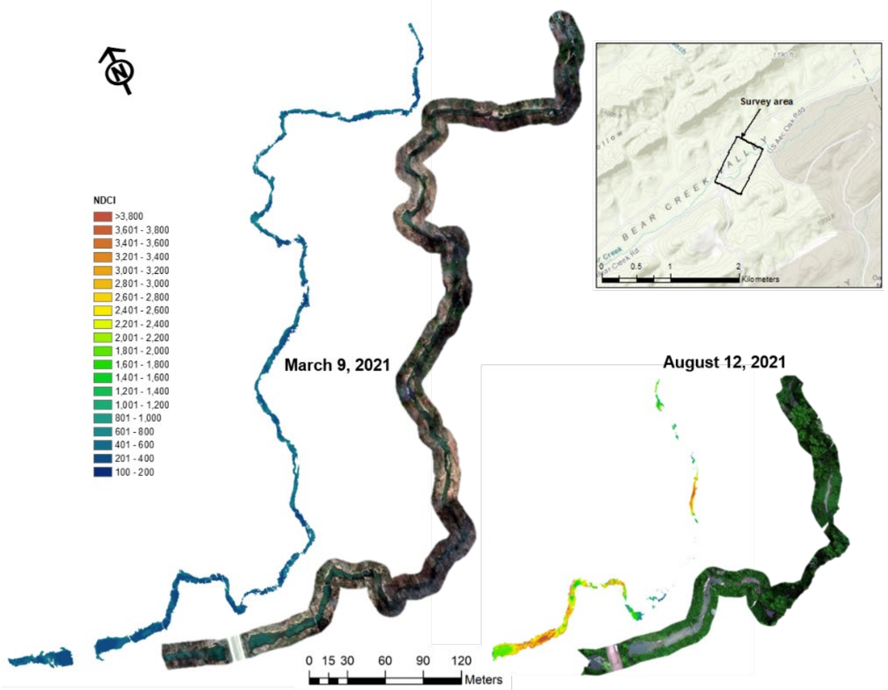

Figure 45. UAS data collected at BCK 7.0 in winter and summer. NDCI and true color images are shown from left to right for each date. Survey area is shown in the inset map.

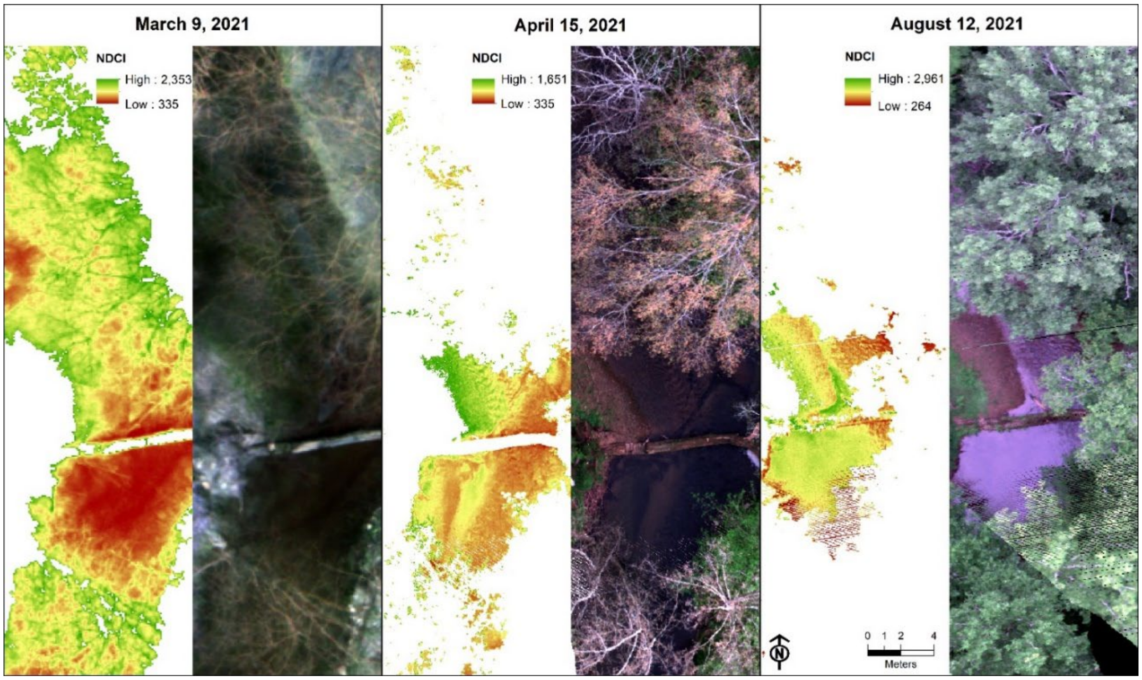

Figure 46. Close-up of section of EFK 6.3 for winter, spring, and summer. NDCI and true color images are shown from left to right for each date. Spatial resolution is 8 cm for the winter data and 5 cm for the spring and winter data. Note the NDCI value ranges are different for each date.

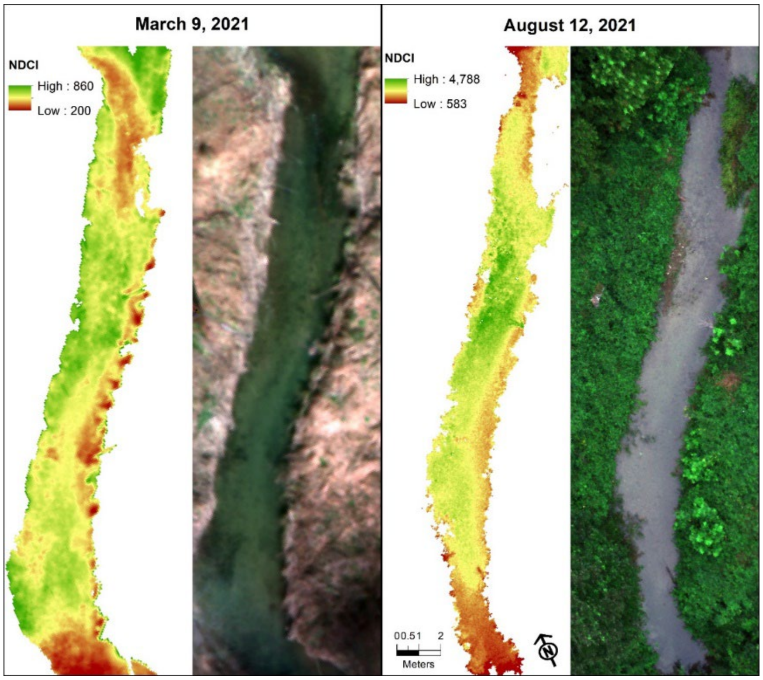

Figure 47. Close-up of section of BCK 7.0 for winter and summer. NDCI and true color images are shown from left to right for each date. Note the NDCI value ranges are different for each date.

The machine learning NDCI model (Figure 48) developed for EFPC stream pixels from the March 2016 WorldView-2 imaging using high-resolution land cover, lidar-derived solar exposure and vegetation metrics, and habitat attributes from the kayak survey as explanatory variables yielded relatively poor model fit with an R^2 of 0.4. This likely indicates drivers of instream aquatic vegetation dynamics that could not be included as predictors because of a lack of sufficient data.

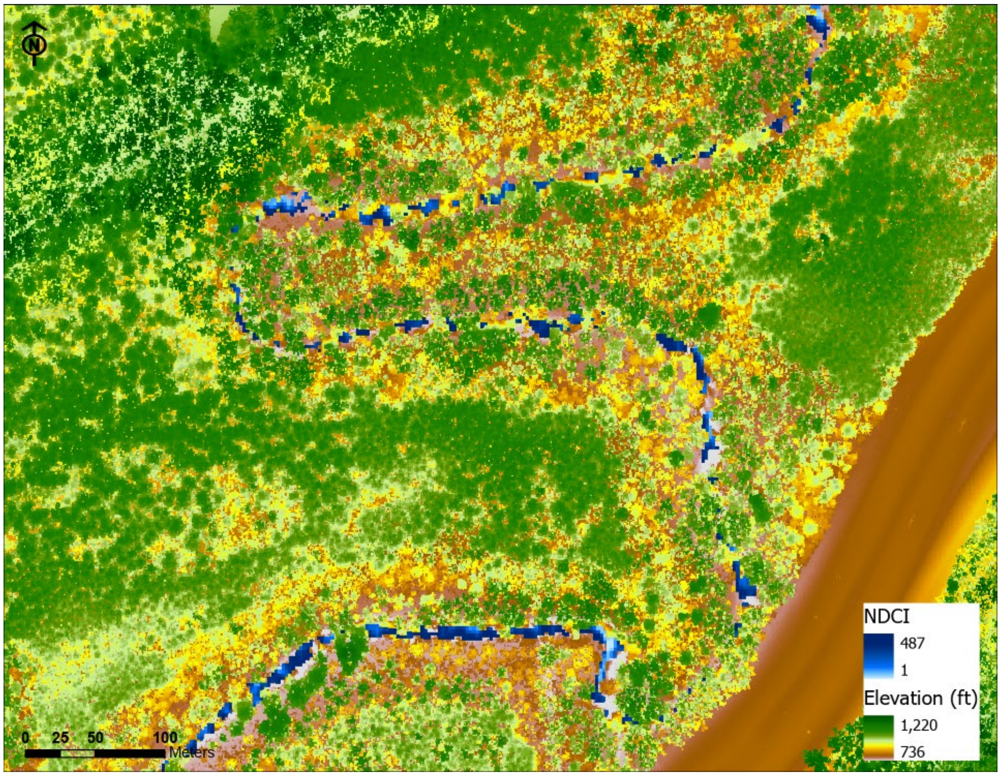

Figure 48. NDCI for water pixels from March 29, 2016 WorldView-2 image near EFK 6.3, overlaid on digital surface model elevations calculated from December 2015/January 2016 3D Elevation Program lidar.

Periphyton lab analyses

Periphyton algal biomass using rock scrapings from which chlorophyll was extracted in the laboratory were quantified using standard spectrophotometric methods. Samples comprised all periphyton scraped from one to two rocks found within riffle, run, and pool habitats at a site during each survey date (minimum of one rock per habitat type) with three technical replicate samples quantified for each scraped sample. Mean chlorophyll *a* biomass ranged from 0.3 to 52 mg cm^{-1} of the rock with large ranges within a site and high levels of variation within a sample (Figure 49). Spring samples collected from EFK 6.3 showed the highest mean chlorophyll values and the highest variability between technical replicates. Data describing the amount of organic carbon present within each sample based on ash-free dry weight were not yet available at the time of writing this report.

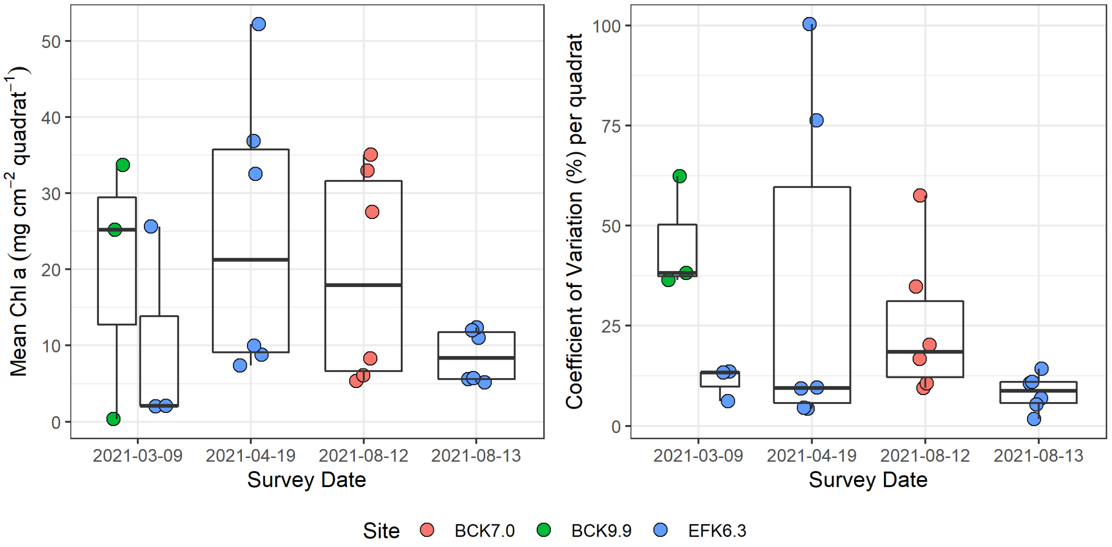

Figure 49. (left) Mean chlorophyll *a* biomass and (right) coefficients of variance estimated for periphyton samples scraped from rocks and quantified in the laboratory using standard spectrophotometric methods.

In situ fluorometric characterization of algal biomass, composition, and distribution

Chlorophyll *a* biomass was estimated fluorometrically within 33 quadrats distributed across 11 transects during the survey at EFK 6.3 on April 15, 2021 (Figure 50). Mean total chlorophyll *a* biomass ranged from 0.090 to 7.6 µg cm^{-2}, with the highest concentrations detected in shallow riffles with coarse gravel substrate, and the lowest concentrations in deeper runs and pools with sand substrate.

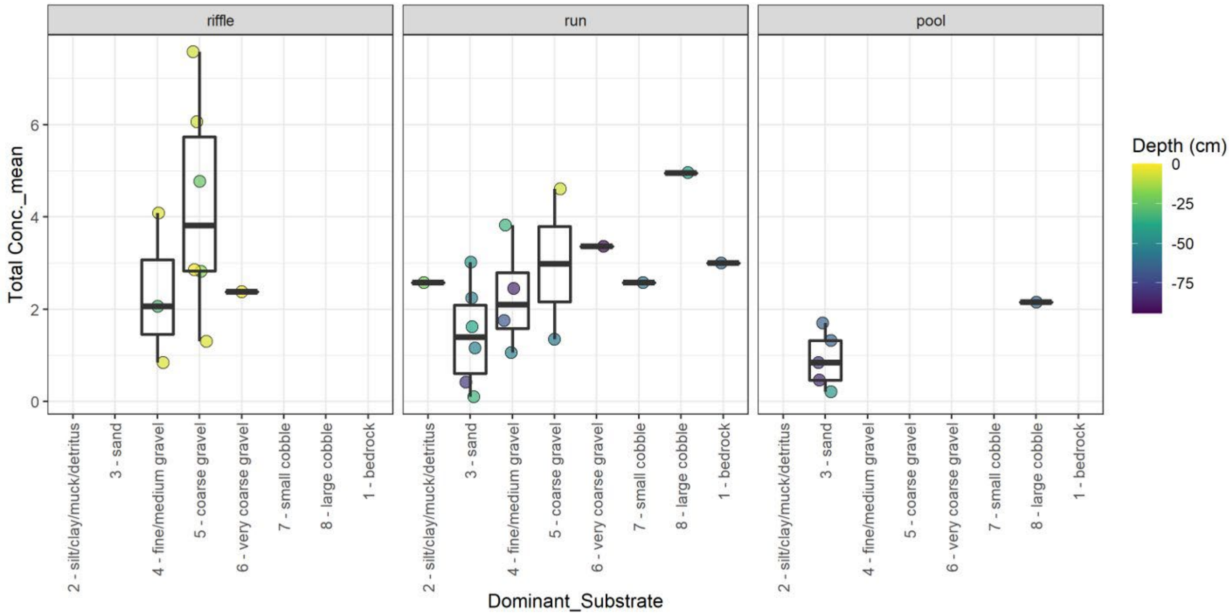

Figure 50. Chlorophyll *a*, depth, habitat type, and substrate from April 15, 2021 survey at EFK 6.3.

Chlorophyll *a* biomass was estimated within 50 quadrats during a survey in Bear Creek on August 12, 2021 and within 25 quadrats during a survey in EFPC on August 13, 2021. Mean total chlorophyll *a* biomass ranged from 0.090 to 3.43 µg cm^{-2} at BCK 7.0 and 0.053 to 5.27 µg cm^{-2} at EFK 6.3, with slightly higher mean biomass at EFK 6.3 (1.52 µg cm^{-2}) than BCK 7.0 (1.04 µg cm^{-2}) (Figure 51). The two quadrats with the highest mean chlorophyll *a* biomass also had very large proportions of chlorophyll associated with green algae (59% and 62%), which was otherwise uncommon in the quadrats (mean of 11%). Most of the chlorophyll biomass was associated with diatoms at both sites (64% at BCK 7.0 and 60% at EFK 6.3), followed by cyanobacteria (32% at BCK 7.0 and 28% at EFK 6.3), with green algae being less common (4% at BCK 7.0 and 12% at EFK 6.3) (Figure 52). Furthermore, green algae were not detected in 64% of the surveyed quadrats at BCK 7.0 or 44% of the surveyed quadrats at EFK 6.3 while diatoms and cyanobacteria were detected in all quadrats at both sites. Preliminary data from EFK 6.3 suggest that taxonomic contributions to chlorophyll *a* biomass may fluctuate across seasons, with higher relative contributions to total chlorophyl from diatoms in spring than summer (78% versus 60%; Figure 53).

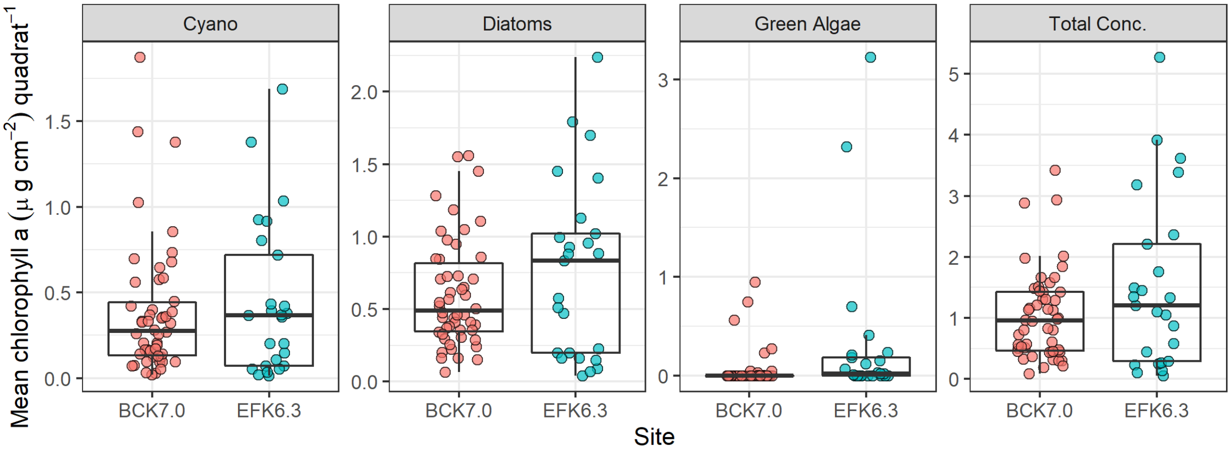

Figure 51. Mean fluorometric estimates of chlorophyll *a* biomass for each taxonomic group (cyanobacteria, diatoms, and green algae) and the total concentration from Bear Creek (red) and EFPC (teal) surveys on August 12 and 13, 2021. Each point represents the mean value (*n* = 3) for each quadrat sampled (BCK 7.0: n = 50; EFK 6.3: *n* = 25).

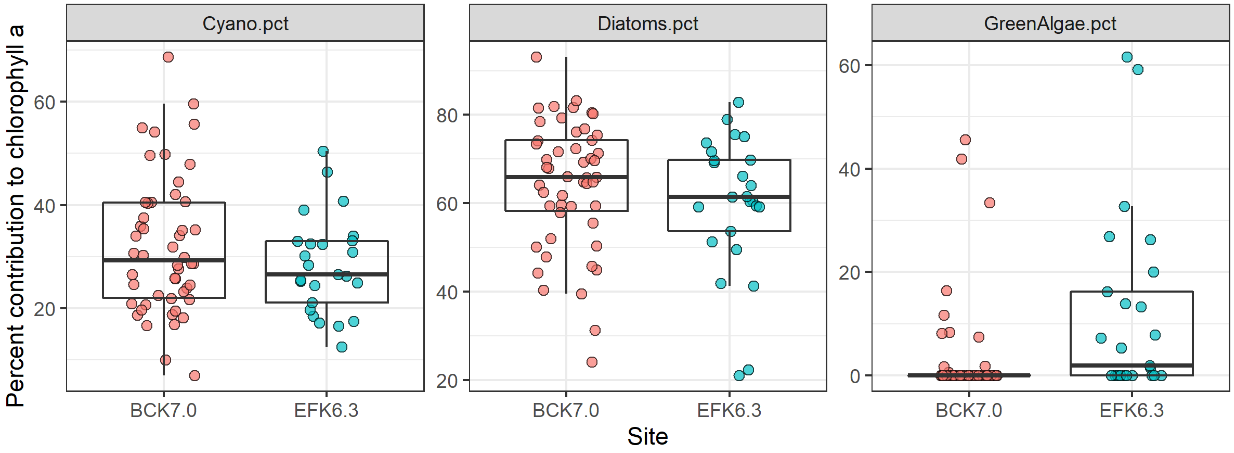

Figure 52. Mean relative abundance of fluorometric total chlorophyll *a* associated with each taxonomic group from Bear Creek (red) and EFPC (teal) surveys on August 12 and 13, 2021. Each point represents the mean value (*n* = 3) for each quadrat sampled (BCK 7.0: *n* = 50; EFK 6.3: *n* = 25).

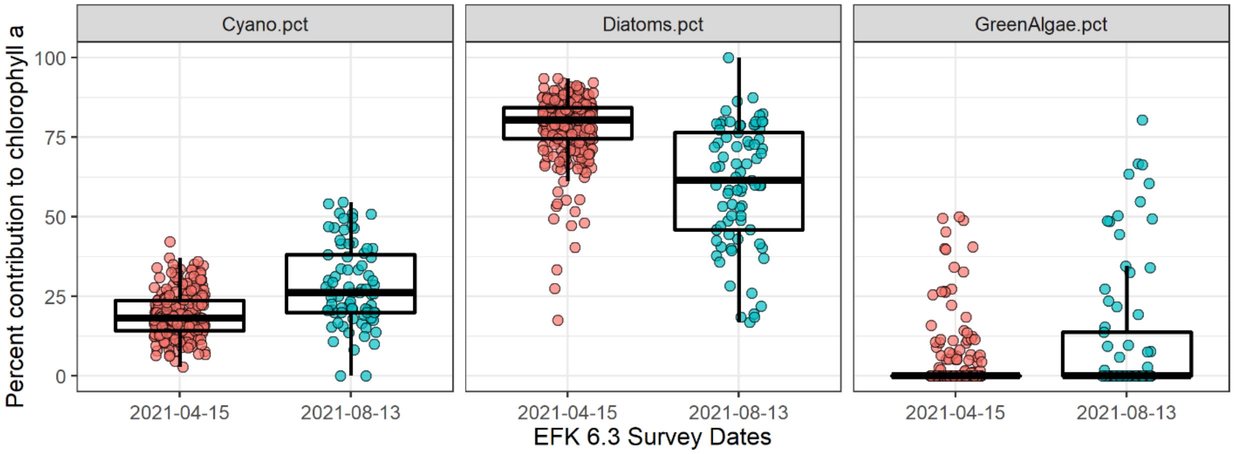

Figure 53. Comparison of taxonomic contributions to chlorophyll *a* biomass in spring (April 15, 2021) and summer (August 13, 2021) at EFK 6.3 based on fluorometric measurements. Each point represents a single fluorometric measurement with sample sizes varying greatly because of different survey methods (*n* = 298 in spring; *n* = 78 in summer).

Associations between fluorometric chlorophyll *a* biomass and habitat were explored at the quadrat scale in Bear Creek and EFPC. Across the eight dominant substrate classes, five were present at both sites. The highest mean chlorophyll biomass measurements were found on gravel at both sites, although biomass on this substrate showed a wide range, particularly at BCK 7.0 (Figure 54). In general, chlorophyll biomass tended to decrease with water depth, with a sharp decline at depths >15 cm (Figure 55). Higher chlorophyll *a* biomass measurements at deeper quadrats may be related to areas of slower water movement, where drifting unattached algae may collect; this will require more investigation in the future.

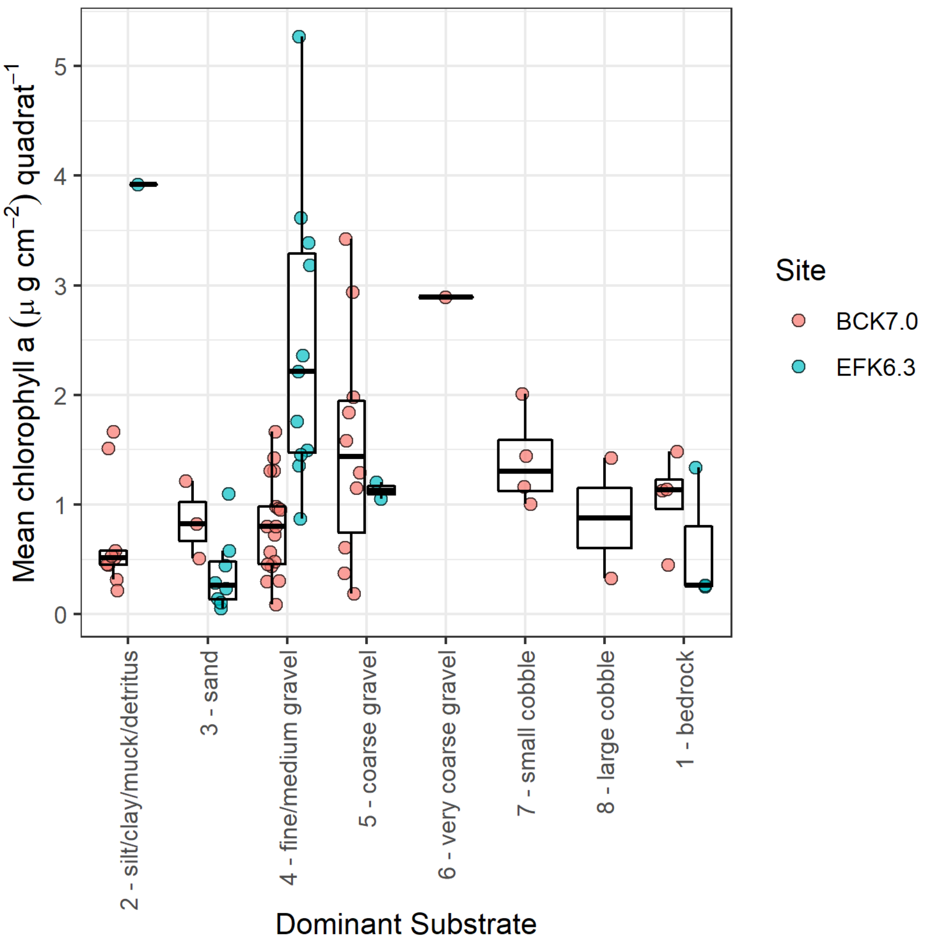

Figure 54. Mean fluorometric estimates of total chlorophyll *a* biomass associated with dominant substrates from Bear Creek (red) and EFPC (teal) surveys on August 12 and 13, 2021. Each point represents the mean value (*n* = 3) for each quadrat sampled (BCK 7.0: *n* = 50; EFK 6.3: *n* = 25).

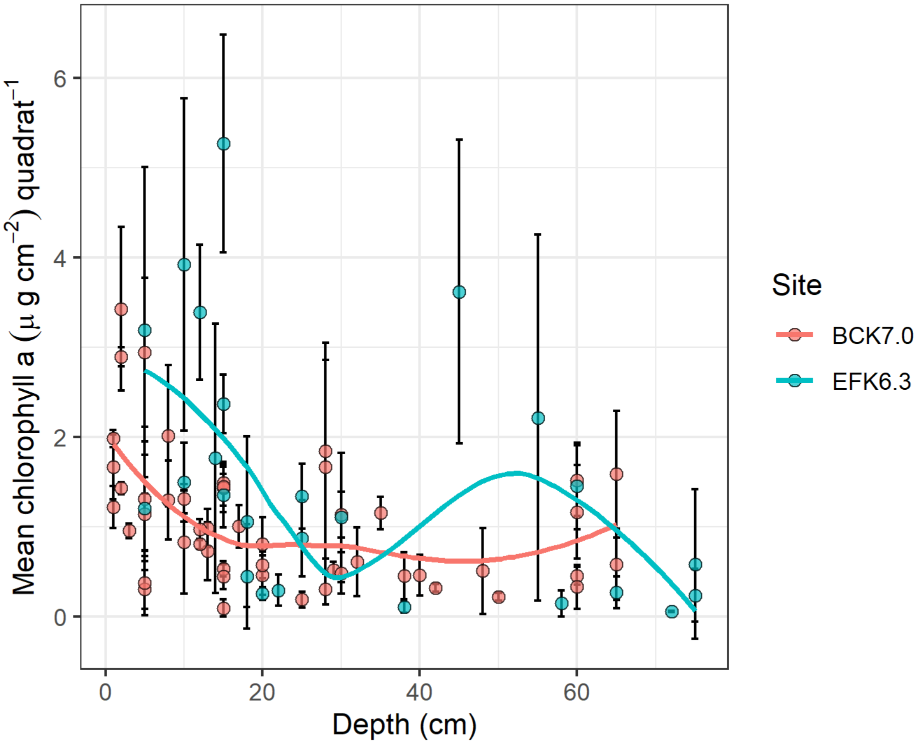

Figure 55. Relationships between fluorometric estimates of total chlorophyll *a* biomass (mean ± standard deviation) and depth from Bear Creek (red) and EFPC (teal) surveys on August 12 and 13, 2021. Each point represents the mean value (*n* = 3) for each quadrat sampled (BCK 7.0: *n* = 50; EFK 6.3: *n* = 25). Colored lines represent loess lines of best fit for each site and are for reference only.

Water sampling

At the time of this writing, water samples from the summer sampling event are still being processed, and results are not yet available. Water quality results for both Bear Creek and EFPC were within expected ranges based on previous springtime sampling events (Table 8). Dissolved oxygen concentrations were higher in the winter samples owing to a combination of less canopy coverage promoting greater algal growth in the creeks and lower temperatures supporting higher dissolved oxygen solubility. DOC concentrations were on the high end of expected ranges, likely because of the high algal activity indicated by the dissolved oxygen results. Total and dissolved MeHg concentrations were higher in EFPC than in Bear Creek. Methylmercury associated with suspended particulates was ~10 times higher in EFPC than in Bear Creek. Notably, MeHg concentration in periphyton from EFPC was nearly 10 times higher than in Bear Creek, emphasizing the important role these complex biofilms play in Hg cycling, MeHg generation, and entry of MeHg into the base of the food web. The MeHg concentrations in periphyton samples from EFPC collected on March 9, 2021 are likely significantly underestimated. Methylmercury levels in one of the samples was high enough to have likely saturated the instrument, resulting in high uncertainty in the true concentration. The sample will be reanalyzed under more appropriate conditions, and the results will be updated.

Table 8. Water quality results for samples collected at BCK 9.9 and EFK 6.3 in spring 2021.

Parameter	BCK 9.9	EFK 6.3	EFK 6.3
	March 9, 2021	March 9, 2021	April 15, 2021
Dissolved oxygen (mg L^{-1})	12.19	12.47	9.57
DOC (mg L^{-1})	3.87	5.19	4.23
MeHg in periphyton (µg kg dw^{-1})	1.68	10.30	
$MeHg_D$ (ng L^{-1})	0.08	0.24	0.34
Particulate MeHg (mg kg dw^{-1})	0.0014	0.015	
Particulate MeHg (ng L^{-1})	0.0038	0.028	0.06
$MeHg_T$ (ng L^{-1})	0.08	0.27	0.40
pH	8.34	8.62	7.78
Spec. cond. (µS cm^{-1})	245.50	295.80	304.70
$SUVA_{254}$ (L mgC^{-1} m^{-1})	1.03	0.92	
Temperature (°C)	9.00	11.48	15.50
TSS (mg L^{-1})	2.70	1.80	
Turbidity (FNU)	1.95	0.00	

2.4.4 Periphyton Dynamics Future Needs

Within this task, several areas of continuing and new research are warranted:

1. Conduct lab/field studies to improve understanding of relationship among benthic algal instrument readings, periphyton measured biomass, and spectral reflectance values from multispectral or hyperspectral sensors

2. Develop a spatially explicit lidar system mounted to UAS and ready for data collection

3. Perform UAS flyovers in late winter/early spring to collect as much spectral/lidar data for as much of Bear Creek and EFPC as possible before leaf-out

4. Use aquatic drone to measure nutrients, temperature, and perhaps other parameters simultaneously with UAS data collection

5. Continue developing machine learning algorithm for chlorophyll indices using spectral imagery, lidar, physical habitat data, and water quality data

6. Acquire and assess utility of NEON hyperspectral and lidar data sets for the purposes of this study

2.5 WATERSHED MODELING

2.5.1 Background

A quantitative and functional understanding of Hg transport from contaminated landscapes is essential for developing site-specific strategies for remediation. In the EFPC watershed, Hg dispersal over soil, groundwater, streambanks, and drainage channels of several upstream sub-watersheds makes remediation of Hg in EFPC a challenging task. Therefore, identifying Hg sources in the EFPC and quantifying the factors that transport Hg to the stream and transform Hg within the stream are essential for planning effective remediation. In this context, process-based models—both watershed-scale hydrology models and instream hydraulic and biochemical models that can provide information for characterizing the movement and transformation—would help in developing a quantitative and functional understanding of transport and effect of Hg in the EFPC. In addition, integrated process modeling would also be useful to test efficacy of new Hg remediation methods and approaches that came out of Hg remediation research.

The goal of this modeling task was to sequentially integrate different models to characterize the hydrology, hydraulics, and biochemical process that drive the Hg transportation and transformation in EFPC. Accordingly, capturing the hydrology of EFPC using a watershed model was the initial focus of the research, followed by instream hydraulics and biochemical process modeling. The watershed models used in this research have been successfully applied to manage non-point/point source pollutants across heterogeneous landscapes (Borah and Bera 2004, Kannan et al. 2007, Jha 2011). This study used a watershed model, Soil and Water Assessment Tool (SWAT), to quantify the drivers of Hg transport over the landscape, including surface and sub-surface flow and suspended solid transport. Furthermore, an empirical link was drawn between simulated flow and suspended solid transport in EEPC with Hg flux (Figure 56). Initial analysis of watershed hydrology revealed three distinct hydrologic patterns in EFPC depending on the sub-watershed.

1. Sub-watershed with significant flow management:

   The head watershed of EFPC, UEFPC, is an industrialized sub-watershed contaminated with Hg. The flow in UEFPC is managed over the years as a Hg remediation measure to reduce Hg flux from UEFPC. Thus, over the years, flow from the UEFPC sub-watershed EFPC behaves more like a point source than natural flow, a stark difference from the rest of the sub-watersheds in EFPC.

2. Sub-watersheds with steady change in land use (LU) from upstream to downstream:

   The second group of sub-watersheds characterizes a steady change from urban land cover upstream to a mix of urban and woodland and then to woodland downstream. This group of sub-watersheds belongs to LEFPC sub-watersheds. Soil and stream banks of several sub-watersheds in LEFPC is contaminated with Hg.

3. Sub-watersheds dominated with woodlands:

   Bear Creek watershed (BCW) is a sub-watershed dominated with woodland land cover. BCW is a watershed with little human intervention and hence is modeled as a separate watershed. The outflow from BCW serves as input into LEFPC at downstream sites.

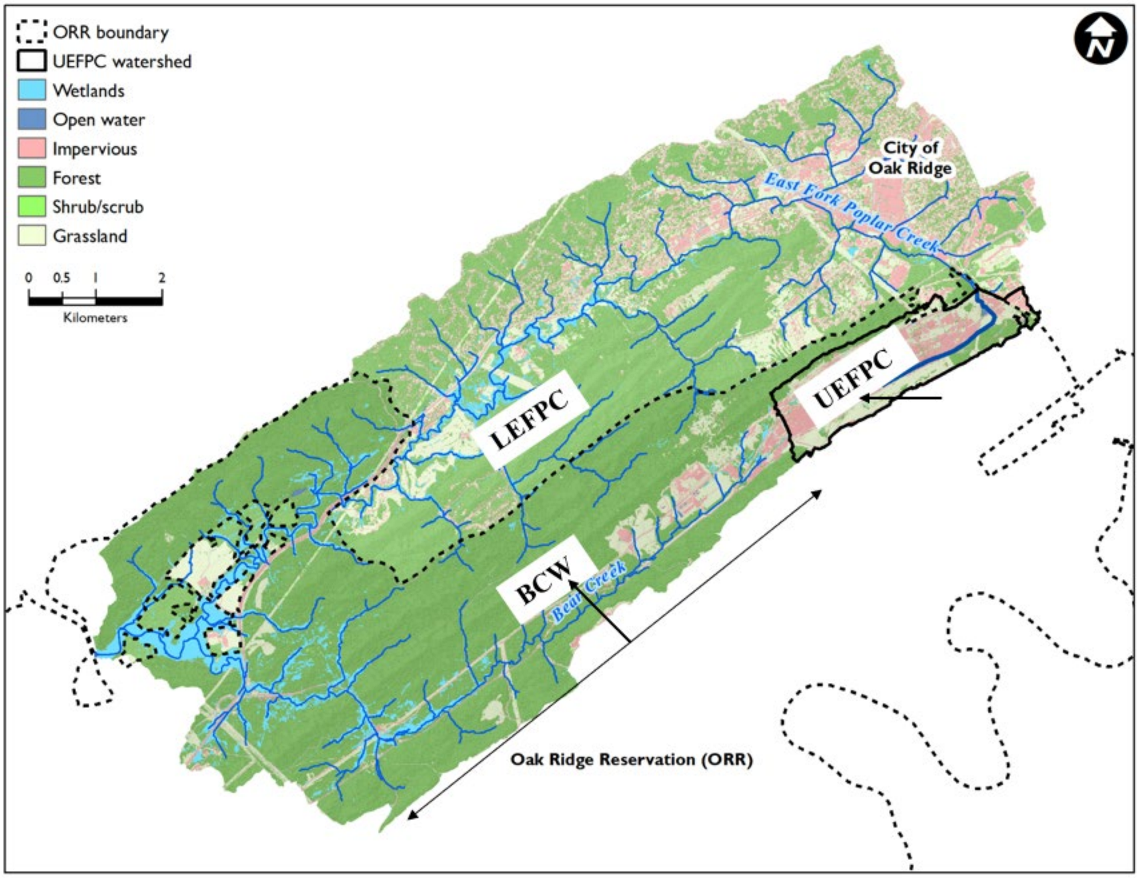

Figure 56. EFPC watershed.

Accordingly, UEFPC, LEFPC, and BCW were modeled separately to capture the complexity in these sub-watersheds by reducing uncertainty in modeling.

2.5.2 Method

Three watershed models were developed using SWAT—SWAT-UEFPC, SWAT-LEFPC (which also included the BCW component), and SWAT-BCW—to represent complexities and heterogeneity in the EFPC watershed and apply these models in a sequential way to capture dynamics of transport of Hg in EFPC watershed, which are at different stages of development (Table 9). For example, calibration and validation of flow and TSS and Hg transport function is estimated for SWAT-UEFPC and SWAT-LEFPC. In contrast, SWAT-BCW is in initial stages of development, in which setting up of SWAT-BCW model is finalized (Table 9).

Table 9. Current status of watershed modeling efforts in EFPC.

	SWAT-Setting Up	Calibration & Validation	Hg Trasportfunction	Scenario Analysis
SWAT-UEFPC	☑	☑	☑	☑
SWAT-LEFPC	☑	☑	☑	
SWAT-BCW	☑			

This report briefly documents the progress in the research on the watershed modeling task over a year, including the baseline Hg dynamics for SWAT-UEFPC modeling and the Hg transport function for UEFPC. Additional results from the scenario analysis with SWAT-UEFPC—including analyzing the effect of an operational MTF on Hg flux from UEFPC, analyzing the effect of building demolition on flow accumulation and flow direction UEFPC, quantifying possible maximum Hg flux from Hg cleaning that would not affect aquatic ecosystems in UEFPC, and SWAT-LEFPC calibration, validation, and Hg transport function estimation—are also reported and discussed.

2.5.3 Result

2.5.3.1 *Baseline spatial and temporal Hg flux dynamics in UEFPC*

The modeled Hg flux over the baseline period was 28.82 g day^{-1} at Station 17, with high variability (standard deviation of 45.25 g day^{-1}) (Figure 57A). Understanding the sources of variability in Hg flux is useful to find ways to reduce the daily Hg flux from the watershed. Therefore, the temporal, spatial, and human-induced influences on variability in Hg fluxes were further explored. Seasonal analysis of daily Hg fluxes at Station 17 revealed higher average daily Hg fluxes during the winter and summer (Figure 57A), with relatively high variability in daily Hg flux in the winter and the lowest variability in daily Hg flux in the summer. In contrast, spring and fall showed lower average daily Hg flux, and fall had the highest daily Hg flux variability. Consistent with previous studies, base flow regimes dominated in Hg flux from the UEFPC, contributing 62.79% of Hg flux to Station 17 across all seasons (Figure 57B), with storm flow and extreme flow contributing 22.09% and 15.12% of the annual daily Hg flux, respectively (Figure 57B).

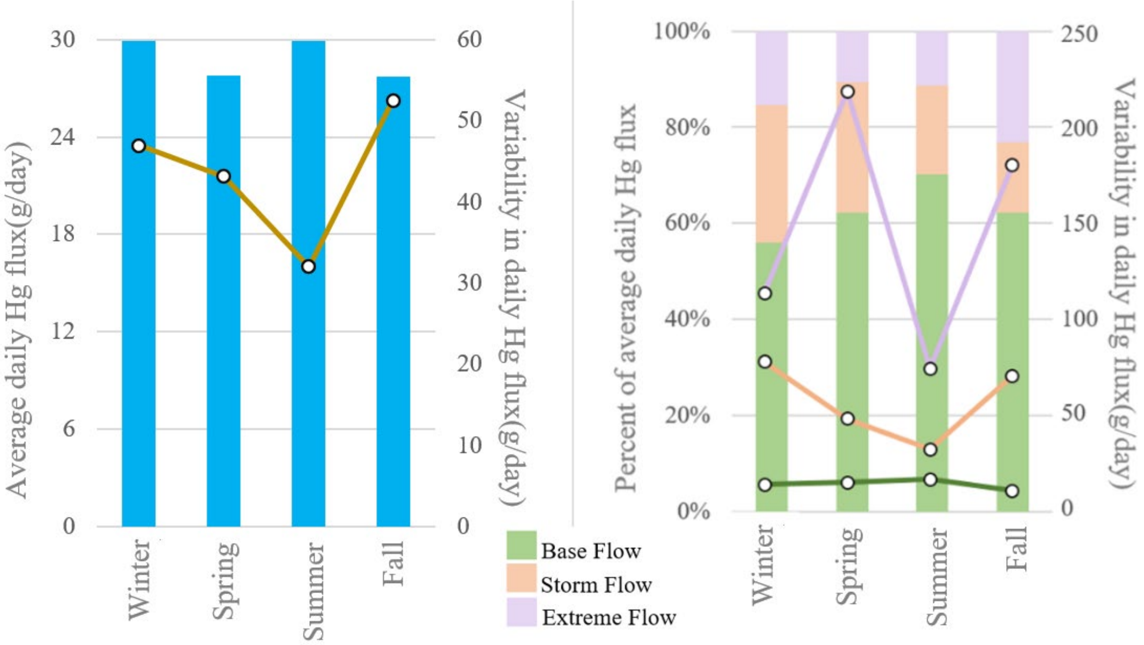

Figure 57. (A) Modeled seasonal daily average flux (g day^{-1}; y1-axis) and variability in daily Hg flux (g day^{-1}; y2-axis) at Station 17; (B) modeled seasonal percentage share (y1-axis) and variability as lines (y2-axis) across flow regimes at Station 17.

Average daily Hg flux at Station 17 was highest in the summer, and base flow contributed to the increase in flux.

2.5.3.2 *Scenario analysis of UEFPC*

Two scenarios were analyzed to further explore: the effect of the MTF on Hg flux dynamics from UEFPC, and the influence of future proposed land cover change in 2040 (no building demolition but land cover change, reduction in impervious land cover) together with the MTF on Hg flux from the watershed (MTF + 2040 LU).

The analysis revealed that an active MTF would substantially reduce the daily average Hg flux from UEFPC, a drop from 28.82 g per day for the baseline scenario to 11.34 g per day for the MTF scenario. However, a land cover change scenario demonstrated a marginal reduction in Hg. In the MTF scenario, the reduction of Hg comes through the active removal of Hg from the surface flow. In contrast, land cover change would marginally increase the chances of less intense surface flows, which would lead to a comparatively lower decrease in Hg. Because the efficiency of removing Hg by the MTF is independent of seasons, the results show a homogeneous reduction in Hg flux over seasons (Figure 58). The MTF also significantly decreased the variability in daily average Hg flux from 46.75 g per day without the MTF (baseline) to 26.14 g per day with the MTF. A decrease in variability of Hg flux with the MTF demonstrates that stormwater storage structures effectively minimize the high fluctuations in Hg flux from extreme flow events (e.g., storms), and land cover changes further reduce intense surface flows. The variability of Hg flux over the seasons for the MTF scenario following the seasonal variation in the storm and extreme flow indicates the importance of flow regimes in Hg flux from UEFPC. Therefore, the analysis was expanded to explore the role of flow regimes on changes in Hg flux over the Hg management scenarios.

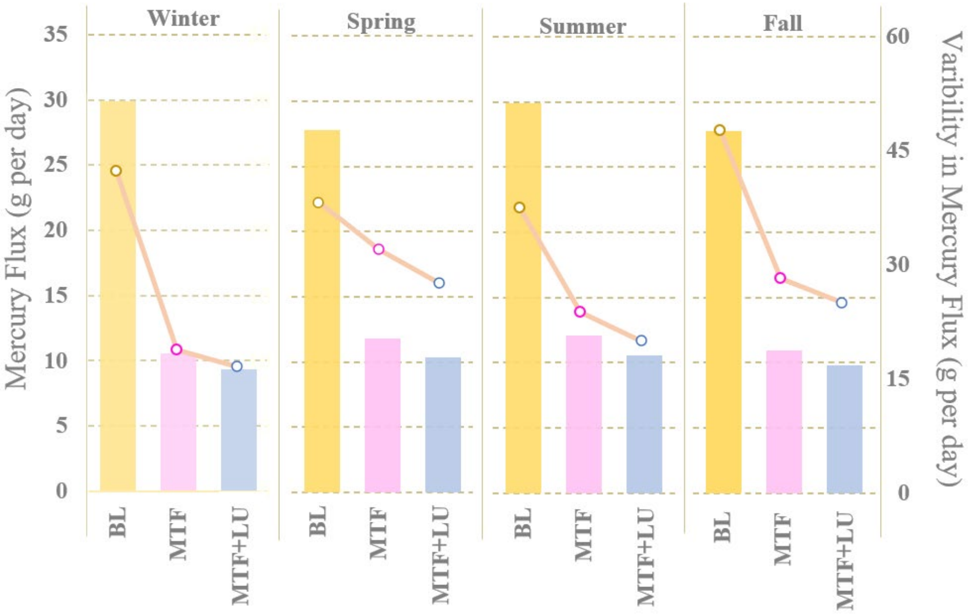

Figure 58. (A) Modeled seasonal daily average flux (g day^{-1}; y1-axis) and variability in daily Hg flux (g day^{-1}; y2-axis) for baseline (BL), MTF, and MTF + 2040 LU at Station 17.

The analysis of Hg flux over the flow regimes and across scenarios showed that base flow contributed the majority (62.79%) of Hg flux at Station 17 across all seasons for baseline simulation, and storm flow and extreme flow contributed 22.09% and 15.12% of the average daily Hg flux, respectively (Figure 59). In contrast, with the MTF, the share of base flow increased to 82.35%, with a corresponding decrease in storm and extreme flow of 11.80%, and 5.85%, respectively. The increase in base flow contribution over MTF and MTF +2040 LU scenarios resulted from a greater reduction of Hg flux from the storm and extreme flow compared with base flow. During extreme flow cases (e.g., storms), the concentration of Hg inflows was very high compared with the base flow, leading to a larger reduction in Hg for such events compared with base flow, which led to an increase in the percent contribution from base flow for MTF and MTF + 2040 LU scenarios. In addition, the average daily Hg flux at Station 17 was highest in the summer, with base flow contributing to the highest share in baseline simulation. A seasonal component to variability in flow regimes was also identified, which affects both the average Hg flux across seasons and the variability in Hg flux. For example, storm and extreme flow played a smaller role in determining Hg flux in the summer. The variability in Hg flux is lowest during the summer. Daily Hg flux at Station 17 positively correlated with base flow (Pearson correlation, $r = 0.51$) and negatively correlated with storm flow ($r = -0.60$) and extreme flow ($r = -0.88$) for the baseline scenario. However, storm flow showed a positive correlation with average daily Hg flux from Station 17 ($r = 0.60$), and extreme flows did not correlate with Hg flux ($r = 0.04$) in the MTF scenario.

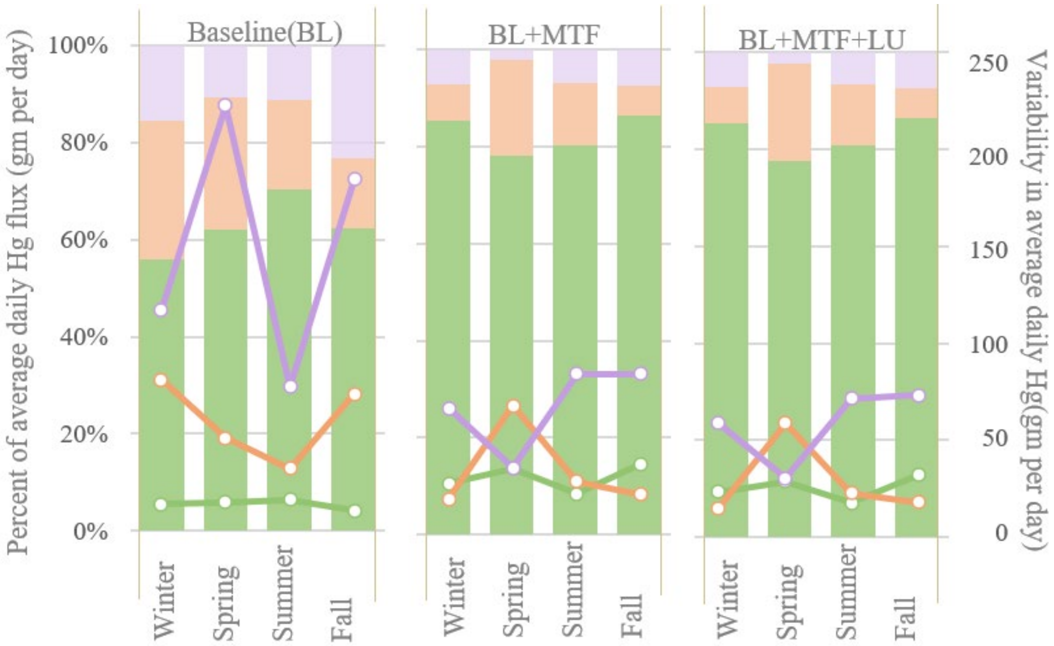

Figure 59. Modeled seasonal percentage share (y1-axis) and variability (y2-axis) across flow regimes for baseline (BL), MTF, and MTF + 2040 LU at Station 17.

Additionally, a drastic decrease in variability of Hg flux across the seasons for the MTF scenario, especially for extreme flow regimes, further indicates the effectiveness of the MTF in reducing Hg flux during storm and extreme flow events, which subsequently resulted in lower variability in Hg flux. In contrast, variability in Hg flux from base flow was seemingly similar over seasons, which indicates a disproportionate reduction of Hg flux from baseline to MTF flow regimes. There is a significant decrease in Hg flux by MTF for the storm and extreme flows compared with the base flow.

The results of monthly Hg flux across three scenarios showed a similar drop in Hg flux by MTF and MTF + 2040 LU over the months (Figure 60). For all the scenarios, March, July, and December reported the highest predicted monthly Hg fluxes across these scenarios, whereas May, June, August, and September had the lowest predicted fluxes. The effective rate of influent (flow at Outfall [OF] 200 + flow from storm water storage) and its Hg concentration determines the efficiency of the MTF. A more highly concentrated Hg influent with a daily effective flow rate close to the treatment efficiency of the MTF would be ideal for maximizing the treatment potential of the MTF. The variation in these two factors determined the variability in monthly effluent concentration from the MTF.

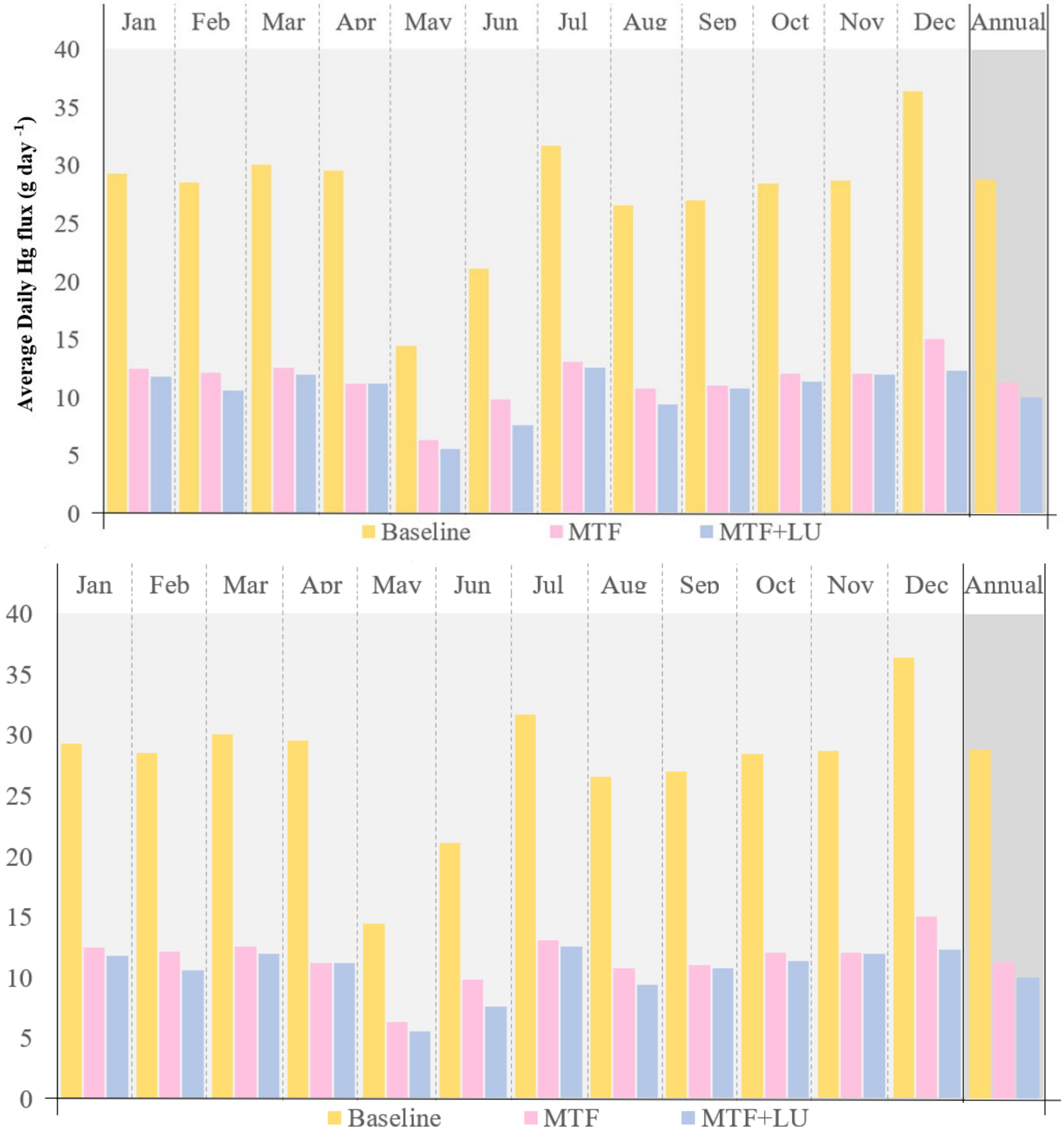

Figure 60. Average daily Hg flux (g day^{-1}) by month for baseline (BL), MTF, and MTF + 2040 LU scenarios at Station 17.

2.5.3.3 *Application of SWAT-UEFPC model*

The SWAT-UEFPC model was used to estimate the average Hg discharge from East COLEX (OF150) that would not exceed the Hg concentration of 10,000 ng/L at OF200 to support the COLEX Hg cleaning efforts. The analysis was implemented in three steps:

1. Simulate flow for OF200 and upstream outfalls using SWAT-UEFPC.

2. Use simulated flow with estimated Hg transport functions to derive the Hg fluxes from OF150, OF160, OF163, OF169, and OF200.

3. Estimate a truncated regression of Hg concentration at OF200 as a function of Hg concentration (Figure 61) from OF150, OF160, OF163, and OF169, with lower truncation value derived from Hg concentration from OF160, OF163, and OF169 and upper truncation value of 10,000 ng/L, beyond which toxicity may be observed in the stream ecosystem.

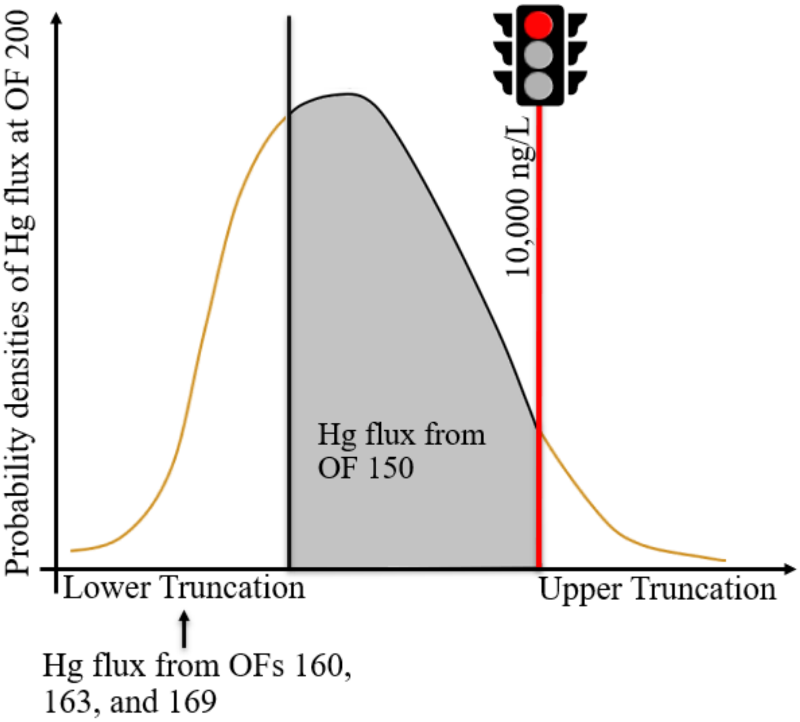

Figure 61. A truncated regression for Hg concentration at OF200 as a function Hg flux from OF150, OF160, OF163, and OF169.

The truncation at the upper end of the probability density function allows for a zero probability for an event resulting in an Hg concentration of 10,000 ng/L at OF200. In contrast, truncation at the lower end of the probability density function would accommodate higher Hg flux from OF160, OF163, and OF169. The upper truncation point was randomly picked from within a range of 9,485 to 10,514 ng/L, and a 95% confidence interval around the target value. The lower truncation point was randomly chosen from 500 to 5,000 ng/L. A total of 50 regressions were estimated with randomly selected upper and lower truncation values, and the maximum possible Hg flux from OF150 was calculated for all 50 cases. The analysis showed that an average Hg concentration of 20,193 ng/L or below from OF150 would ensure that Hg concentrations at OF200 remain below 10,000 ng/L.

2.5.3.4 *Developing SWAT-LEFPC*

Data requirements for the initial setup of SWAT are shown in Table 10. A high-resolution (0.72 m) lidar-derived digital elevation model (DEM) and a high-resolution (1:24,000 scale) stream network from the National Hydrography Dataset were used to delineate the watershed and 152 sub-watersheds for LEFPC. Using the National Land Cover Dataset (Homer et al. 2015) and medium-resolution (1:250,000 scale)

STATSGO soil data (USDA-NRCS 2006), the SWAT model further divided 237 sub-watersheds into 461 HRUs (hydrologic response unit) in the LEFPC watershed. Weather data inputs for the watershed model, specifically rainfall data, were compiled from two data sets (2000–2019); rainfall data for the LEFPC watershed area within the Oak Ridge Reservation were obtained from weather data from Oak Ridge Reservation Meteorology. For the rest of the LEFPC watershed area, rainfall data from DATMET weather data set were used after a bias correction using daily rainfall data from the Oak Ridge Reservation site.

Table 10. Data inputs and sources for initial SWAT setup.

Data Input	Spatial resolution	Source
Topography (DEM)	0.72 m	TNGIS
Climate		Oak Ridge Reservation, Daymet
Soils	Medium	STATSGO US Department of Agriculture
LU	30 m	US Geological Survey
Stream network	High	NHDPlus V2
Drainage Network Y-12	High	Y-12

The first step in setting up the SWAT model was to delineate the UEFPC watershed. In general, watersheds have been developed using bare earth DEM and a natural stream layer, which would represent flow generation and flow accumulation by changing the curve number associated with LU. However, it cannot account for the changes in flow direction and emergence of more connected flow paths with the urban landscapes. This aspect is important to account for Hg transport in LEFPC because the HRD area of Hg resides in urbanized areas upstream of LEFPC. Therefore, an effective topography (DEM + building and other structures) and stream layer for LEFPC was used for developing LEFPC topography to better represent the flow paths in the watershed. Lidar-derived 3D structures of buildings and other structures in LEFPC were used in combination with the existing bare earth DEM to create the effective topography, the final DEM, for LEFPC.

The entire simulation period, 1995–2018, was divided into three sections:

1. The first 5 years, 1995–1999, were used for model warm-up.
2. The following 10 years, 2000–2009, were used for calibration of the model.
3. The remaining 9 years, 2010–2018, were used to validate the model at the downstream monitoring point of LEFPC, New Horizon.

Because Hg contribution varies across the stream segments in the LEFPC watershed, the validated model was evaluated at Wiltshire Drive (EFK 16.2) and downstream of the Oak Ridge Wastewater Treatment Facility (EFK 13.5). The Nash-Sutcliffe coefficient of efficiency (E) and the linear regression coefficient of determination (R^2) of simulated values of flow and TSS against the observed values (Pineiro et al. 2008) were used to measure the performance of the model.

The results of the daily time series for the validation periods for flow and suspended solids at the New Horizon monitoring point are provided in Figure 62. In general, the trends in predicted streamflow and suspended solid concentrations were consistent with those of observed streamflow. Additionally, calculated efficiency measures for streamflow ($R^2 = 0.82$ and $E = 0.66$) and TSS ($R^2 = 0.94$ and $E = 0.89$) demonstrated a high match between simulated and measured variables. The internal flow monitoring points at Wiltshire Drive and downstream just below the Oak Ridge Wastewater Treatment Facility also showed good agreement between simulated and measured streamflow.

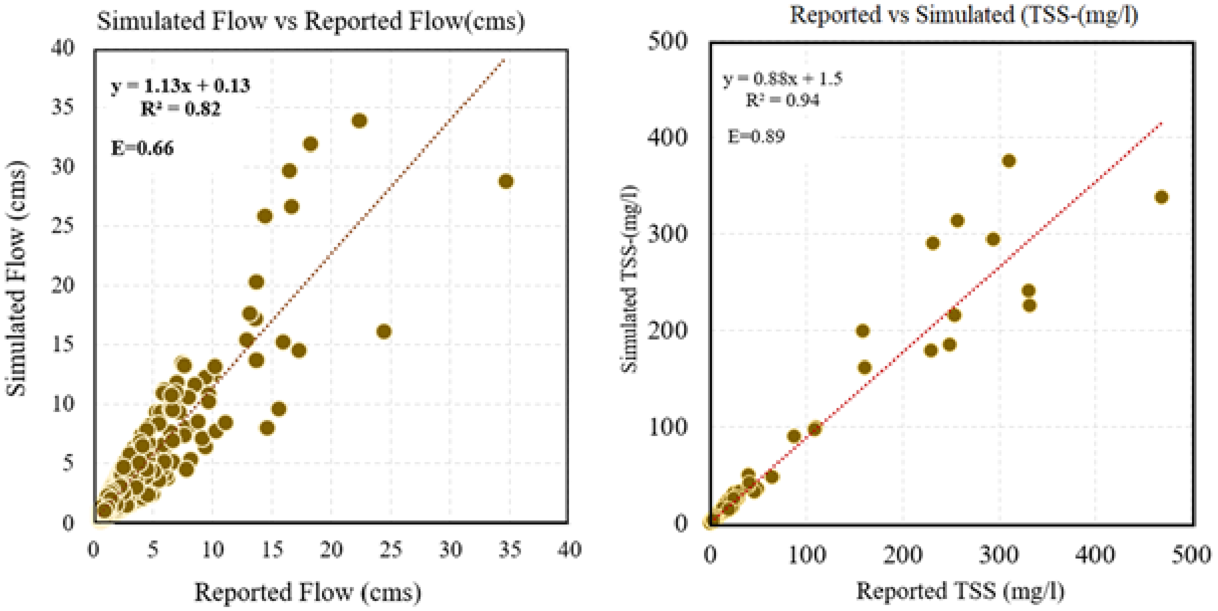

Figure 62. The relationship between simulated flow and TSS by SWAT-LEFPC and reported flow and TSS values.

2.5.3.5 *Hg loading function for New Horizon*

A statistical Hg transport model was estimated to quantify Hg flux from the simulated flow, suspended solids, and other relevant variables. Long-term Hg monitoring data sets for LEFPC (from the Oak Ridge Environmental Information System and Science Focus Area-Hg by DOE) and simulated flow and TSS were used to establish a quantitative functional relationship between Hg flux with the simulated flow and suspended solids for LEFPC at New Horizon.

$$Hg_{NH} = f(Flow_{NH}, TSS_{NH}, FR, FA, LU, Flow_{NH} \times FR, Flow_{NH} \times FA, Flow_{NH} \times S, TSS_{NH} \times LU, TSS_{NH} \times FR, TSS_{NH} \times FA, TSS_{NH} \times S, TSS_{NH} \times LU) \qquad (9)$$

where *NH* is New Horizon and represents estimated Hg flux and simulated flow at New Horizon, and the control variables were added to isolate the influence of season (*S*), flow regime (*FR*), flow augmentation (*FA*), and land use change (*LU*) on Hg flux at *NH*. Two flow regimes were considered for the study: base flow (<12.5 mm rainfall) and storm flow (≥12.5). The control variables, including *S*, *FR*, *FA*, and *LU*, were introduced as dummy variables. For example, *LU* is assigned a value of 1 after a significant land use change happened in the watershed for a specific year. Otherwise, it received a value of 0. In this case, construction of a Kroger grocery store at the intersection of South Illinois Avenue and Oak Ridge Turnpike was considered. As land preparation started in early August 2013, *LU* received a value of 1 after July 2013 and otherwise received a value of 0. Similarly, three dummy variables were added to represent four seasons, and one dummy variable was added for three flow regimes.

Separate Hg transport functions for Hg_D and Hg_T for the New Horizon monitoring point were estimated. Results showed that Hg_D displayed a linear relationship with its covariates, including flow and TSS, flow regimes, and seasons, whereas Hg_T exhibited a log-log relationship with its drivers. Furthermore, both Hg-flux regressions showed a high predictive ability with an adjusted R^2 value of 0.70 for Hg_D and 0.73 for Hg_T (Table 11).

Table 11. Estimated Hg flux function at New Horizon.

	Hg_D		**Hg_T**	
	Regression coefficient	**‘t value**	**Regression coefficient**	**‘t value**
Functional form	**Linear**		**Log-log**	
Intercept	0.14	0.17	1.31	11.48
Flow	1.09	7.12		
TSS	0.34	7.57	0.95	9.89
BF	2.77	2.33	−4.79	−14.71
Winter	7.79	2.11	−0.18	−1.72
Summer			−0.11	−1.92
BF × flow				
Summer × BF	−1.41	−1.87		
FA × flow	−0.93	−1.92		
LU change × flow	0.50	2.71		
FA × TSS			−0.04	1.52
LU change × TSS			0.03	1.89
Adjusted R^2	0.70		0.73	

BF = base flow, BF × flow = interaction between flow and base flow; LU change × flow = interaction between LU change and flow; FA × flow = interaction between flow augmentation and flow Grey shaded areas indicate the variable that is not significant in the model.

TSS significantly influenced Hg_T flux. The regression coefficient for TSS indicates that a 1% increase in TSS would result in a 0.95% increase in Hg_T in the watershed. Additionally, base flow, summer, and winter negatively influenced the Hg_T flux. The cessation of FA decreased HgT, whereas LU change increased HgT through loading more TSS. Flow management was considered as one of the remediation measures, and the result showed the opposite impact, stopping FA reduced HgT at New Horizon (FA increased the HgT)Analysis was further extended so that different models were estimated sequentially to understand which variable overshadowed the effect of the flow on Hg_T. Initially, a null model was estimated—Hg_T as a function of TSS and flow—and explained 60% of the variation in Hg_T. However, when base flow was added to the null model, the R^2 value increased to 0.72, but flow was not significant, and TSS and base flow were substantial. Base flow evidently controls the variation induced by the flow on Hg_T in LEFPC. Therefore, the Hg_T function was re-estimated by adding an additional flow × BF, along with TSS, flow, and BL. TSS and BL remain significant in this new specification, as well. The analysis reconfirms that BF overshadowed the influence of flow. Another empirical specification was estimated with TSS as the dependent variable, and flow, *FA*, *FR, S*, and *LU* as the independent variables to understand how TSS and flow are linked together (Table 12). The results show that flow, storm flow, and LU change positively contributed to TSS, whereas winter and spring seasons and stopping flow augmentation negatively affected TSS loading in the watershed.

Table 12. Estimated Hg flux function at New Horizon.

	TSS	
	Regression coefficient	‘t value
Intercept	–0.18418	–2.66637
Flow	2.201875	15.21788
BF	4.13949	53.63065
BF × flow	–0.87844	–5.39028
Winter	–0.47414	–3.7215
Spring	–0.34591	–2.01915
FA	–0.11228	–2.15789
LU-change	0.04882	1.91
Adjusted R^2	0.93	

3. CONCLUSIONS AND FUTURE DIRECTIONS

Significant scientific and technological progress has been made during the 7 years of the Mercury Remediation Technology Development project. A strategy was developed early in the program that is consistent with the adaptive management paradigm and DOE’s Technology Readiness Level guidelines. Initially, field studies were prioritized to better understand the Hg sources, transformations, transport, and fate processes in the EFPC system. Systems-level studies have pointed to the importance of stream BSs—and especially HRDs—in the upstream section of EFPC as a source of Hg to the creek, the relatively small role of groundwater and floodplain sources, the importance of flow and other water chemistry and particle characteristics on the form of Hg, the importance of periphyton on Hg methylation, and the role of MeHg found in prey species on fish receptors. A watershed approach to EFPC remediation is used because it considers all the contributing factors that affect Hg transformations in the environment. Quantitative modeling received a greater focus in FY 2021 to simulate remediation and technology development scenarios and better inform future remedial decision-making (Figure 63). Understanding the potential outcomes of environmental change could lead to opportunities for decreasing Hg risks while also managing and restoring the stream for natural resource benefits and/or water quality improvement.

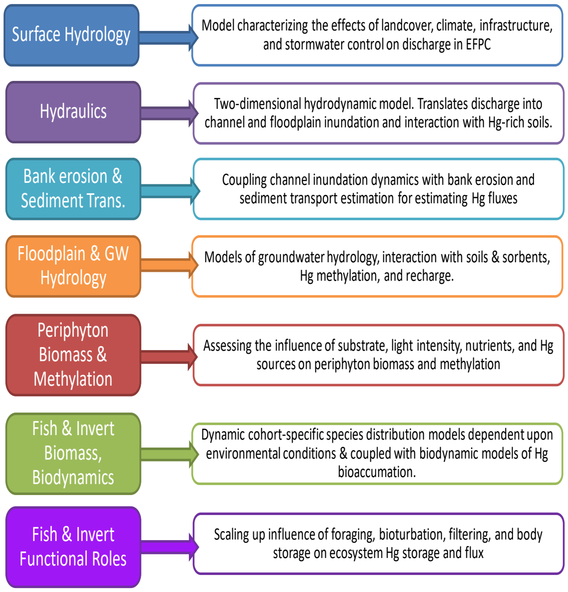

Figure 63. EFPC ecosystem model sections informing the understanding of the EFPC watershed ecosystem using SWAT and the US Army Corps of Engineers Hydrologic Engineering Center River Analysis System.

With a better spatial and temporal understanding of the watershed system, specific technologies and strategies are being assessed as potential abatement actions. These approaches are being applied to Bear Creek. Studies have been conducted to evaluate alternative treatment chemicals on Hg flux, the role of sorbents on Hg and MeHg with DOM, and the use of bivalves as a tool for reducing particle-associated Hg in the water column.

Future directions for Hg research and technology development in LEFPC will include targeted field studies to inform key process and research questions, enhancement of the watershed-scale understanding through quantitative modeling, a greater emphasis on mesoscale studies of potential technologies in the upgraded AEL (Figure 64), and remediation and technology simulation to inform the LEFPC remedial alternatives evaluation in the mid-2020s. In FY 2020, the design and construction of new experimental capabilities in the AEL at ORNL was completed. The modernized facility will provide a unique capability to evaluate Hg remediation technologies in a variety of source waters. Laboratory studies in the AEL will continue in FY 2022 and will advance the scale of testing beyond field studies and bench-scale testing.

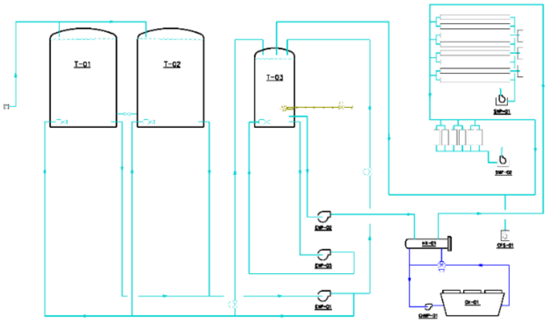

Figure 64. Schematics of the upgraded AEL design. The system includes two 8,000 gal holding tanks; one 650 gal equalization (mixing) tank; a chiller and heat exchanger to modulate water temperature; a series of pumps and valves to control flow from distribution lines to point of use locations in the labs; and integrated monitors and alarms. A touchscreen human machine interface with a programmable logic controller allows monitoring and control of the system inside the lab.

REFERENCES

Acha, D., C. A. Pabon, and H. Hintelmann. 2012. "Mercury methylation and hydrogen sulfide production among unexpected strains isolated from periphyton of two macrophytes of the Amazon." *FEMS Microbiol Ecol* 80(3): 637–645. doi:10.1111/j.1574-6941.2012.01333.x.

Borah, D. K., and M. Bera. 2004. "Watershed-scale hydrologic and nonpoint-source pollution models: review of applications." *Trans. ASAE* 47(3): 789–803.

Brooks, S. C., C. L. Miller, A. L. Riscassi, K. A. Lowe, J. O. Dickson, and G. E. Schwartz. 2021. "Increasing temperature and flow management alter mercury dynamics in East Fork Poplar Creek." *Hydrological Processes* 35(8): e14344.

Brooks, S., E. Virginia, J. Dickson, J. Earles, K. Lowe, T. Mehlhorn, T. Olsen, C. DeRolph, D. Watson, and M. Peterson. 2017. *Mercury Content of Sediments in East Fork Poplar Creek: Current Assessment and Past Trends*. ORNL/TM-2016/578, Oak Ridge National Laboratory, Oak Ridge, Tennessee. doi:10.2172/1338545.

Buma, W. G. and S. I. Lee. 2020. "Evaluation of Sentinel-2 and Landsat 8 Images for Estimating Chlorophyll-a Concentrations in Lake Chad, Africa." *Remote Sensing*. doi:10.3390/rs12152437.

Carrell, A. A., et al. 2021. "Nutrient exposure alters microbial composition, structure, and mercury methylating activity in periphyton in a contaminated watershed." *Frontiers in Microbiology* 12(543):647861. doi:10.3389/fmicb.2021.647861.

Catherine, A., N. Escoffier, A. Belhocine, A. B. Nasri, S. Hamlaoui, C. Yepremian, C. Bernard, and M. Troussellier. 2012. "On the use of the FluoroProbe®, a phytoplankton quantification method based on fluorescence excitation spectra for large-scale surveys of lakes and reservoirs." *Water Research* 46(6): 1771–1784. doi:10.1016/j.watres.2011.12.056.

Chasar, L. C., B. C. Scudder, A. R. Stewart, A. H. Bell, and G. A. Aiken. 2009. "Mercury cycling in stream ecosystems. 3. Trophic dynamics and methylmercury bioaccumulation." *Environmental Science & Technology* 43, 2733–2739.

Dickson, J. O., M. A. Mayes, S. C. Brooks, T. L. Mehlhorn, K. A. Lowe, J. K. Earles, L. Goñez-Rodriguez, D. B. Watson, and M. J. Peterson. 2018. "Source relationships between streambank soils and streambed sediments in a mercury-contaminated stream." *J. Soils Sediments* 19(4): 2007–2019.

DOE (US Department of Energy). 2017a. *Strategic Plan for Mercury Remediation at the Y-12 National Security Complex, Oak Ridge, Tennessee.* DOE/OR/01-2605&DR/R1. Oak Ridge Office of Environmental Management.

DOE (US Department of Energy). 2017b. *Mercury Technology Development Plan for Remediation of the Y-12 National Security Complex and East Fork Poplar Creek, Oak Ridge, Tennessee.* DOE/ORO-2489/Rev. 1. Oak Ridge Office of Environmental Management.

Duncan, A., B. Vacaliuc, M. Larson, C. Davis, D. Hughes, and K. Corcoran. 2019. "Integration and operation of a sUAS-based multi-modal imaging payload equipped with a novel communication system enabling autonomous platform control." *Proc. SPIE 11021, Unmanned Systems Technology XXI* 1102103. doi:10.1117/12.2517022.

Echenique-Subiabre, I., C. Dalle, C. Duval, M. W. Heath, A. Coute, S. A. Wood, J. F. Humbert, and C. Quiblier. 2016. "Application of a spectrofluorimetric tool (bbe BenthoTorch) for monitoring potentially toxic benthic cyanobacteria in rivers." *Water Research* 101: 341–350. doi:10.1016/j.watres.2016.05.081.

Gilmour, C. C., G. S. Riedel, G. Riedel, S. Kwon, R. Landis, S. S. Brown, C. A. Menzie, and U. Ghosh. 2013. “Activated Carbon Mitigates Mercury and Methylmercury Bioavailability in Contaminated Sediments.” *Environmental Science & Technology* 47(22): 13001–13010.

Harris, T. D. and J. L. Graham. 2015. “Preliminary evaluation of an in vivo fluorometer to quantify algal periphyton biomass and community composition.” *Lake and Reservoir Management* 31(2): 127–133. doi:10.1080/10402381.2015.1025153.

Hills, A., S. Pouil, D. Hua, and T. J. Mathews. 2020. “Clearance rates of freshwater bivalves Corbicula fluminea and Utterbackia imbecillis in the presence and absence of light.” *Aquatic Ecology* 54(4): 1059–1066.

Homer, C. G., et al. 2015. “Completion of the 2011 National Land Cover Database for the conterminous United States – Representing a decade of land cover change information.” *Photogrammetric Engineering & Remote Sensing* 81(5): 345–354.

Jha, M. K. 2011. “Evaluating hydrologic response of an agricultural watershed for watershed analysis.” *Water* 3(2): 604–617.

Johs, A., V. A. Eller, T. L. Mehlhorn, S. C. Brooks, D. P. Harper, M. A. Mayes, E. M. Pierce, and M. J. Peterson. 2019. “Dissolved organic matter reduces the effectiveness of sorbents for mercury removal.” *Sci Total Environ* 690: 410–416.

Joslin, J. D. 1994. “Regional differences in mercury levels in aquatic ecosystems- A discussion of possible causal factors with implications for the Tennessee River System and the Northern Hemisphere.” *Environmental Management* 18: 559–567.

Kahlert, M. and B. G. McKie. 2014. “Comparing new and conventional methods to estimate benthic algal biomass and composition in freshwaters.” *Environmental Science-Processes & Impacts* 16(11): 2627–2634. doi:10.1039/c4em00326h.

Kannan, N., S. M. White, F. Worrall, and M. J. Whelan. 2007. “Hydrological modelling of a small catchment using SWAT-2000 - ensuring correct flow partitioning for contaminant modelling.” *J. Hydrol*. 334(1–2): 64–72.

Kaylor, M. J., A. Argerich, S. M. White, B. J. VerWey, and I. Arismendi. 2018. “A cautionary tale for in situ fluorometric measurement of stream chlorophyll a: Influences of light and periphyton biomass.” *Freshwater Science* 37(2): 287–295. doi:10.1086/697239.

Kelly, C. A., J. W. M. Rudd, V. L. Louis, and A. Heyes. 1995. “Is total mercury concentration a good predictor of methylmercury concentrations in aquatic systems.” *Water Air and Soil Pollution* 80(1–4): 715–724.

Luoma, S. N. and P. S. Rainbow. 2005. “Why is metal bioaccumulation so variable? Biodynamics as a unifying concept.” *Environ Sci Technol*. 39(7): 1921–1931. doi:10.1021/es048947e.

Martínez Collado, J. L. 2021. *Terrestrial laser scanning technology for measuring streambank retreat along East Fork Poplar Creek and calculating the effect on mercury release*. The University of Tennessee.

Mathews, T. J., B. B. Looney, A. L. Bryan, J. G. Smith, C. L. Miller, G. R. Southworth, and M. J. Peterson. 2015. “The effects of a stannous chloride-based water treatment system in a mercury contaminated stream.” *Chemosphere* 138: 190–196.

Mathews, T. J., et al. 2019. *Mercury Remediation Technology Development for Lower East Fork Poplar Creek—FY 2019 Update*. ORNL/SPR-2019/1243, Oak Ridge National Laboratory, Oak Ridge, Tennessee.

Mathews, T., G. Southworth, M. Peterson, W. K. Roy, R. Ketelle, C. Valentine, and S. Gregory. 2013. "Decreasing aqueous mercury concentrations to achieve safe levels in fish: examining the water-fish relationship in two point-source contaminated streams." *Sci. Total Environ*. 443: 836–843.

Muller, K. A. and S. C. Brooks. 2018. "Effectiveness of sorbents to reduce mercury methylation." *Environ. Eng. Sci*. 36(3): 361–371. doi:10.1089/ees.2018.0375.

Muller, K. A., C. C. Brandt, T. J. Mathews, and S. C. Brooks. 2019. "Methylmercury sorption onto engineered materials." *J. Environ. Management* 245: 481–488. doi:10.1016/j.jenvman.2019.05.100 (data doi:10.17632/jcfwd5sg4w.1).

Myers, D. T., Rediske, R. R., McNair, J. N. 2019. "Measuring Streambank Erosion: A Comparison of Erosion Pins, Total Station, and Terrestrial Laser Scanner." *Water* 11: 1846. doi:10.3390/w11091846.

Olsen, T. A., C. C. Brandt, and S. C. Brooks. 2016. "Periphyton biofilms influence net methylmercury production in an industrially contaminated system." *Environ. Sci. Technol*. 50(20): 10843–10850. doi:10.1021/acs.est.6b01538.

Paulson, K. M. A. 2014. *Methylmercury Production in Riverbank Sediments of the South River, Virginia (USA) and Assessment of Biochar as a Mercury Treatment Option*. University of Waterloo, Waterloo, Ontario.

Paulson, K. M. A., C. J. Ptacek, D. W. Blowes, W. D. Gould, J. Ma, R. C. Landis, and J. A. Dyer. 2018. "Role of Organic Carbon Sources and Sulfate in Controlling Net Methylmercury Production in Riverbank Sediments of the South River, VA (USA)." *Geomicrobiol J* 35(1): 1–14.

Peterson, M. J., et al. 2018. *Mercury Remediation Technology Development for Lower East Fork Poplar Creek—2017 Progress Report.* ORNL/TM-2017/480, Oak Ridge National Laboratory, Oak Ridge, Tennessee.

Peterson, M. J., S. C. Brooks, T. J. Mathews, M. A. Mayes, A. Johs, D. B. Watson, M. D. Poteat, and E. Pierce. 2015. *Mercury Remediation Technology Development for Lower East Fork Poplar Creek.* ORNL/SPR-2014/645, Oak Ridge National Laboratory, Oak Ridge, Tennessee.

Pineiro, G., S. Perelman, J. P. Guerschman, and T. M. Paruelo. 2008. How to evaluate models: observed vs. predicted or predicted vs. observed? *Ecol. Model*. 216(3–4): 316–322.

Pouil, S., A. Hills, and T. J. Mathews. 2021 "The effects of food quantity, light, and temperature on clearance rates in freshwater bivalves (Cyrenidae and Unionidae)." *Hydrobiologia* 848(3): 675–689.

Rosero-Lopez, D., M. T. Walter, A. S. Flecker, D. F. Ontaneda, and O. Dangles. 2021. "Standardization of instantaneous fluoroprobe measurements of benthic algal biomass and composition in streams." *Ecological Indicators* 121(10): 107185. doi:10.1016/j.ecolind.2020.107185.

Sankey, T. T., J. McVay, T. L. Swetnam, M. P. McClaran, P. Heilman, and M. Nichols. 2017. "UAV hyperspectral and lidar data and their fusion for arid and semi-arid land vegetation monitoring." *Remote Sensing in Ecology and Conservation* 4(1): 20–33. doi:10.1002/rse2.44.

Schwartz, G. E., T. A. Olsen, K. A. Muller, and S. C. Brooks. 2019. "Ecosystem controls on methylmercury production by periphyton in a contaminated freshwater stream: Implications for predictive modeling." *Environ. Toxicol. Chem*. 38(11): 2426–2435. doi:10.1002/etc.4551.

Southworth, G., M. Peterson, and M. Bogle. 2004. "Bioaccumulation factors for mercury in stream fish." *Environ. Pract*. 6: 135–143. doi:10.1017/S1466046604000249.

Tom, K. R., M. C. Newman, and J. Schmerfeld. 2010. "Modeling mercury biomagnification (South River, Virginia, USA) to inform river management decision making." *Environmental Toxicology and Chemistry* 29(4): 1013–1020. doi:10.1002/etc.117.

Tsui, M. T. K., J. C. Findlay, S. J. Balogh, and Y. H. Nollet. 2010. “In situ production of methylmercury within a stream channel in northern California.” *Environ Sci Technol* 44: 6998–7004.

Turner, R. R. and G. R. Southworth. 1999. *Mercury Contaminated Sites*. R. Ebinghaus, R. R. Turner, L. De Lacerda, O. Vasiliev, and W. Salomons, Eds. Berlin: Springer-Verlag.

USDA-NRCS (US Department of Agriculture–Natural Resources Conservation Service). 2006. *US General Soil Map (STATSGO2)*. doi:10.15482/USDA.ADC/1242480.

Ward, D. M., K. H. Nislow, C. Y. Chen, and C. L. Folt. 2010. “Rapid, Efficient Growth Reduces Mercury Concentrations in Stream-Dwelling Atlantic Salmon.” *Transactions of the American Fisheries Society* 139: 1–10.

Watson, D., M. et al. 2017. *Evaluation of lower East Fork Poplar Creek mercury sources–Model update*. ORNL/SR-2016/503, Oak Ridge National Laboratory, Oak Ridge, Tennessee.

Watson, D., S. Brooks, T. Mathews, M. Bevelheimer, C. DeRolph, C. Brandt, M. Peterson, and D. Ketelle. 2016. *Evaluation of lower East Fork Poplar Creek mercury sources.* ORNL/TM-2016/134, Oak Ridge National Laboratory, Oak Ridge, Tennessee.